Solar Radio Observations At Low Frequencies With High Spectral And Temporal Resolution

A Thesis
Submitted for the degree of
Doctor of Philosophy (Technology)

Submitted by
K Hariharan

Department of Applied Optics & Photonics
University College of Technology
University of Calcutta
April-2017

I would like to dedicate this thesis to my colleagues at the Gauribidanur Radio Observatory as a sign of gratitude. I also dedicate this thesis to my family and friends for their motivation and moral support.

Acknowledgements

I would like to thank my thesis supervisor for providing me the opportunity to carry out my doctoral thesis work at the Gauribidanur Radio Observatory one of the field stations of the Indian Institute of Astrophysics. I sincerely thank all my other colleagues, friends and family members for their continued support and encouragement during the course of my PhD. Though an exhaustive list, I refrain from mentioning specific names in order to not miss out anyone.

Foreword

Ground-based radio observations of the solar corona at low frequencies ($<$ 100 MHz) provide useful information in the height range $\approx 1-2$ $R_\odot$ above the photosphere which is presently difficult to observe at other regions in the electromagnetic spectrum. Observations in the above height range are crucial since it is widely believed that some of the transient Sun-induced disturbances in the near-Earth space have their origin there. The other advantage is that the radio emission associated with transient solar activities are primarily non-thermal in nature, and hence more intense at low frequencies. Radio spectral observations in the corresponding frequency range are more worthwhile in this regard since they provide information over the entire range of heliocentric distance. Note that the radio emission at different frequencies originate at different distances from the Sun due to the inherent decrease in the electron density with increasing distance and the characteristics of radio wave propagation in an ionized medium like the solar atmosphere. So radio emission associated with any propagating disturbance in the solar atmosphere can be observed as a distinct featue in a time-frequency waterfall plot of the dynamic spectrum.

This thesis describes the attempts made in this regard to carry out spectral observations at low frequencies down to the local ionospheric cut-off with high spectral and temporal resolutions at the Gauribidanur Radio Observatory under the auspices of the Indian Institute of Astrophysics. A low-frequency single antenna spectrograph system for observing solar transient radio emissions was configured to operate over the frequency range 15$-$85 MHz with the commercially available analog spectrum analyzer as back-end. A detailed description on the design of low-frequency antennas and filters is presented. The details of various experimental tests and inferences of the analog front-end components is also described.

Using the new low-frequency antenna set-up and the existing instruments at the GRO we reported the radio imaging, spectral, and polarimeter

observations of a type II radio burst associated with the solar coronal mass ejection (CMEs). Simultaneous ground-based, low-frequency (< 100 MHz) radio imaging, spectral, and polarization observations of type II bursts are quite rare. From the radio spectral and imaging observations in tandem with the coronagraph observations we reinforce the close spatio-temporal association of CMEs and type II radio bursts which has been one of the long standing debates in solar radiophysics. We also had the opportunity to estimate coronal magnetic field strength ahead of and behind a CME, particularly from the dcp of the associated harmonic type II radio burst, with proper justifications. Though observations of circularly polarized harmonic type II bursts have been reported earlier, estimates of the coronal magnetic field from the observed circular polarization are not available. In this respect this was a unique set of observation with a combination of ground-based radio (< 100 MHz) and space-based coronagraph observations.

Another rare variant of the type II solar radio emission is the multiple type II radio burst phenomenon in which two or more type II bursts occur in quick succession. The occurrence of two successive Type-II bursts (referred to as Type-II doublets) in particular have been attributed to either two successive flares or two successive CMEs or a flare and a CME. We have reported radio spectral and polarimeter observations of two successive split-band Type-II bursts within a time interval of one minute at low frequencies (< 100 MHz). Interestingly, both bursts exhibit Fundamental-Harmonic as well as split-band structure. Type-II doublets with the above combined characteristics have rarely been reported. Our analysis of the data indicates that the first and the second Type-II bursts in the present case were likely due to MHD shocks generated by the near-simultaneous interaction of two different regions of the aforementioned CME with a preceding CME and a pre-existing coronal streamer.

In the case of a conventional analog spectrum analyzer, at any give time data is obtained only at a single frequency since it is a swee-tuned instrument. The temporal resolution of such an instrument is determined by the sweep-time and the frequncy range of operation. The number of frequency channels over the operating frequency range is often fixed and hence results in poor frequency resoluion for larger bandwidths. Note that

an improvement in the temporal resolution could help us to understand the quasi-periodicity in the solar radio bursts and the related estimates of the coronal magnetic field strength. Higher spectral resolution can be used to identify and remove the RFI in frequency space while an improvement in the amplitude resolution leads to an enhancement of dynamic range in the measurements. In view of the above, we commissioned a new digital spectro-corrlator instrument using commercially available digitizer, for regular solar obsevations over the frequency range $15 - 30$ MHz. The details of the instrument and the observational results obtained with it are presented in detail.

From the encouraging results obtained wih the above narrow-band spectrograph system, we configured a wide-band full digital back-end for the new spectrograph array that was recently commissioned at the GRO. An high-speed ADC-FPGA based data recorder was tested and characterised to be used as digital back-end receiver for the spectrograph array. Preliminary observations were carried out with both the digital and analog back-end for the spectrograph array to compare and contrast the results. The characterization of the ADC and the details of the FPGA board are presented in detail. The details on the data acquisition and pre-processing of the spectral data is also described.

Quasi-continuum radio emissions of duration $10 - 60$ min that occur in close association with CMEs in the solar atmosphere are termed as moving type IV bursts. The latter is found to accompany only about 5% of the CMEs. This provides a unique oppurtunity to study and infer the characteristics of CMEs viz. electron density, magnetic field strength etc. by simultaneously observing both the phenomena. We have reported the near-Sun ($r \lesssim 2R_{\odot}$) radio heliograph, radio spectrograph, and radio polarimeter observations of a type IVm burst that was co-spatial with the leading edge (LE) of a white light CME. To our knowledge, concurrent observations of the above type have rarely been reported. A complete analysis was performed to infer the electron density of the CME and the associated coronal magnetic field strength.

List of Publications

1. *Simultaneous Near-Sun Observations of a Moving Type IV Radio Burst and the Associated White-Light Coronal Mass Ejection*
   K. Hariharan, R. Ramesh, C. Kathiravan and T. J. Wang, Solar Physics Journal, 2016, Volume 291, 1405.
2. *High Dynamic Range Observations of Solar Coronal Transients at Low Radio Frequencies With a Spectro-Correlator*
   K. Hariharan, R. Ramesh, C. Kathiravan, H. N. Abhilash and M.Rajalingam Astrophysical Journal of Supplimentary Series, 2016, Volume 222, 21.
3. *Observations of Near-Simultaneous Split-Band Solar Type-II Radio Bursts at Low Frequencies*
   K. Hariharan, R. Ramesh and C. Kathiravan Solar Physics Journal, 2015, Volume 290, pp2479.
4. *An Estimate of The Coronal Magnetic Field Near a Solar Coronal Mass Ejection From Low -Frequency Radio Observations*
   K. Hariharan, R. Ramesh, P. Kishore, C. Kathiravan and N. Gopalswamy Astrophysical Journal, 2014, Volume 795, pp14
5. *An Estimate of The Magnetic Field Strength Associated With A Solar Coronal Mass Ejection From Low Frequency Radio Observations*
   K. Sasikumar Raja, R. Ramesh, **K. Hariharan**, C. Kathiravan and T. J. Wang Astrophysical Journal, 2014, Volume 796, pp56.
6. *Constraining the Solar Coronal Magnetic Field Strength Using Split-Band Type II Radio Burst Observations*
   P. Kishore, R. Ramesh, **K. Hariharan**, C. Kathiravan and N. Gopalswamy Astrophysical Journal, 2016, Volume 832, pp59.
7. *Wideband Digital Spectrometer for Low Frequency Solar Observations*
   K. Hariharan, V. Mugundhan and R. Ramesh Experimental Astronomy Journal (in preparation).

8. *Estimation of Density Modulation Index in Middle Corona Using Type-IIIb Solar Radio Bursts*
   V. Mugundhan, **K. Hariharan** and R. Ramesh Solar Physics Journal (in preparation)

Contents

List of Figures

Chapter 1

Introduction

Being the nearest stellar object to Earth our Sun has intrigued and interested astronomers for many centuries. Innumerable attempts have been made towards understanding the physics of our Sun. By studying the electromagnetic radiation, originating from the Sun, at visible wavelengths astronomers have classified it to be a G2V type star among other spectral categories of the stellar population (Figure 1.1). Through careful in-depth studies of the elemental composition from the Solar spectrum and from carbon dating of rocks and fossils of trees, the age of our Sun has been estimated to be about 4.5 billion years. The radius of the visible disk ($R_\odot$) of our Sun has been estimated to be around 6.96×10^5 Km with a mass ($M_\odot$) $\approx 1.9889 \pm 0.0003 \times 10^{30}$ Kg and a luminosity ($L_\odot$) $\approx 3.84 \pm 0.04 \times 10^{26}$ W (Foukal, 2004). Due to our inaccessibility to the interior structure of the Sun, it's structure and evolution are determined using the "standard solar model" (SSM; Bahcall *et al.*, 1982) which gives a description of the stellar structure derived from basic physical properties of the Sun mentioned above.

The energy released by the Sun is mostly generated at the interior-most layer (referred as the "core") of the Sun. The core is at a very high temperature $\approx 1.5 \times 10^7$ K due to the thermonuclear reactions that take place there. At this temperature, the proton-proton (pp) chain is the dominant process on which four protons are fused to form a Helium nucleus. Though there are several ways for this process to occur, the main mechanism is described by the ppI chain as shown below :

$$ {}^1_1\mathrm{H} + {}^1_1\mathrm{H} \longrightarrow {}^2_1\mathrm{H} + \mathrm{e}^1 + \nu_\mathrm{e} \tag{1.1} $$

$$ {}^2_1\mathrm{H} + {}^1_1\mathrm{H} \longrightarrow {}^3_2\mathrm{He} + \gamma \tag{1.2} $$

$$^{3}_{2}\mathrm{He} + {}^{3}_{2}\mathrm{He} \longrightarrow {}^{4}_{2}\mathrm{He} + {}^{1}_{1}\mathrm{H} \tag{1.3}$$

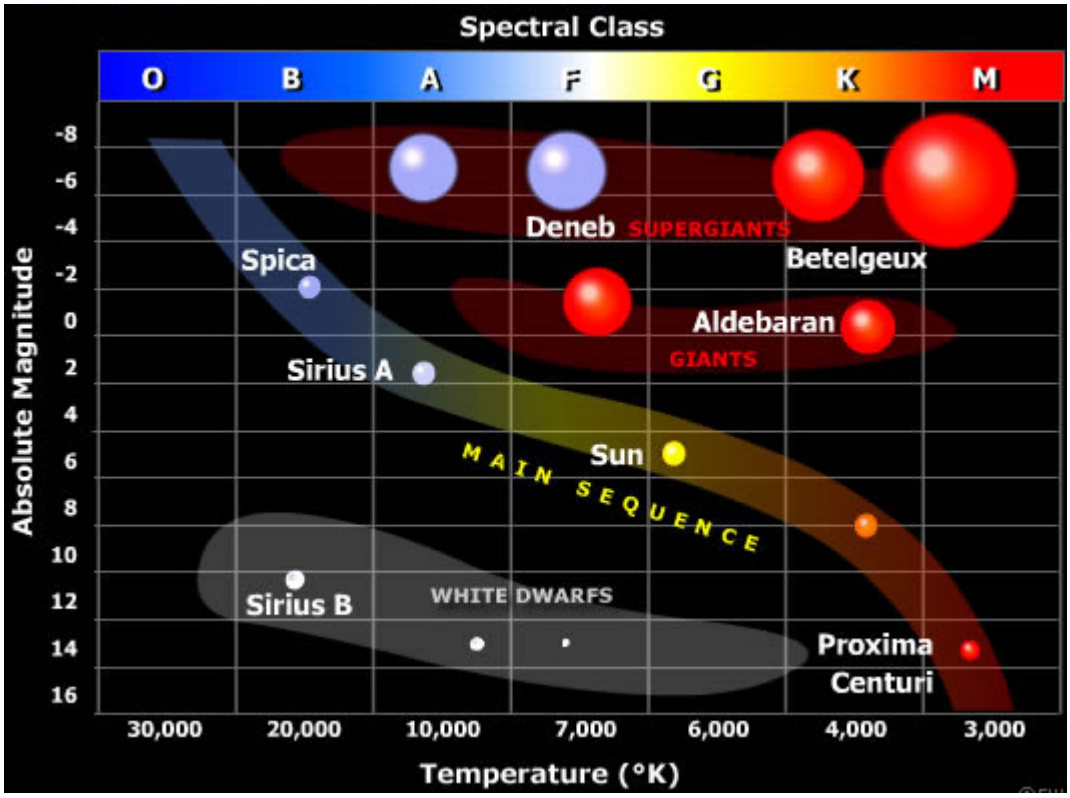

Figure 1.1: The Hertzsprung-Russel (HR) Diagram of classification of stars based on absolute magnitude and temperature

As one moves out of the core close to it's outer boundary the temperature drops to about 8 million Kelvin and the fusion reaction ceases. This region extends from $\approx 0.25 - 0.75$ $R_{\odot}$ and it is called the "radiative" zone, consisting only of free electrons and protons. Photons generated at the core are continuously scattered-off by the free particles and take about 10^5 years to traverse this region through a random-walk process. Due to the thermal equilibrium of the photons with matter, the thermal radiance can be well described by the Planck equation (blackbody distribution) given by:

$$B_{\nu} = \frac{8\pi h\nu^3}{c^3\left(e^{(h\nu/kT)} - 1\right)} \tag{1.4}$$

The temperature further drops down to 2 million Kelvin close to the boundary of the radiative zone which allows the formation of highly ionized atoms and the

plasma becomes optically thick. This region is called the "convective" zone as the sudden increase in opacity causes the plasma to become unstable. The heat is then transported in convective cells from this region to the solar surface which is at a temperature of $\approx$ 5800 K. The radiation and convection regions are separated by a relatively thin interface (referred as the "tachocline"), where the solid body rotation of the radiative region encounters the differentially rotating outer convection region. Due to this, the tachocline has a very large shear profile which could account for the formation of large scale magnetic fields which is the basic idea of the "solar dynamo". The differential rotation of the convection region gives rise to large scale winding of magnetic field within the region. This effect, called the Ω-effect gives rise to a 22-year periodicity for the magnetic field with the reversal of the magnetic poles occurring every 11 years commonly known as the "solar cycle". The latter gives rise to the increased and decreased periods of solar activity which manifest in many different forms and is observed in the atmosphere of the Sun.

1.1 Solar Atmosphere

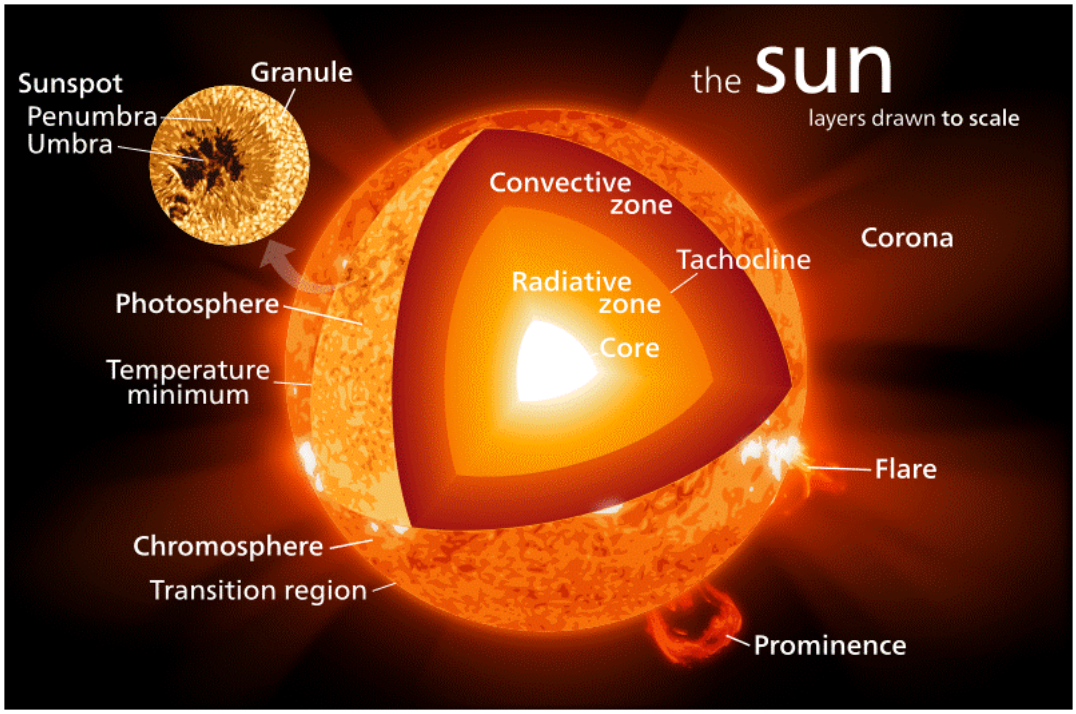

Figure 1.2: An artistic illustration of the Sun from the interior layer to the Solar atmosphere

Astrophysical studies on the Sun have been possible by studying the electromagnetic radiation coming from the atmosphere of the Sun. Based on the distribution of the number density of electrons and the temperature profile, the solar atmosphere (Figure 1.2) can be divided into four distinct regions :

Photosphere This region starts where the solar atmosphere becomes optically thin for the visible band of the electromagnetic spectrum. This is described as the point where the optical depth equals 2/3 for wavelengths of 5000Å($\tau_{5000} \backsim 2/3$ for $I/I_0 = e^{-\tau}$). Photospheric radiation is emitted at this optical depth and the effective temperature ($T_{eff} \approx 5776$ K) is equal to the blackbody temperature of the photosphere. A variety of features have been observed to appear on the photosphere due to the dynamics happening in the interior convective region, described as follows :
i)*granules* – These are formed by the convective motion of plasma in the photospheric region
ii) *super-granules* – large-scale granular network that spreads all over the sun
iii) *sunspots* – these are non-convecting regions on the photosphere which appear as dark features on the visible disk due to their relatively lower temperature compared to the ambient medium. These are regions of intense magnetic field resulting from electric current generated by the flow of charged particles and ionized gases in the medium. the non-uniform rotational motion of the photosphere gives rise to dense plasma regions ($'$active regions$'$) which harbour powerful magnetic fields
iv) *faculae* – these are relatively less dense magnetic regions which appear as bright features on the white-light images.

Chromosphere The photosphere is followed by a thin layer of atmosphere called chromosphere. This layer is spread over a few hundred kilometers above the photosphere with a slightly higher temperature of $\approx$ 20000 K. At this temperature the chromosphere emits Hα emission at 6562.8 Å.

Transition Region The temperature abruptly rises from 20000 K in the chromosphere to about 10^6 K in the outer atmosphere. Due to this abrupt change, there is heat flow from the outer layer to the chromosphere creating a thin irregular layer in the atmosphere called the transition region. Due to the very high temperature, hydrogen is ionized and it becomes difficult to observe. But the various ionized states of heavier elements like Silicon (Si), Carbon (C), Oxygen (O) and Iron (Fe) are observed

as very narrow spectral line emissions in the Ultra-violet band of the electromagnetic spectrum.

Corona The solar corona is the outermost layer of the Earth's atmosphere. It is a tenuous cold plasma medium at a temperature of over 10^6K. The reason for the abnormally high temperature of the corona has been an intense subject of interest. Many theoretical and observational studies are dedicated to the understanding of the driver for the heating in the corona, this is one of the long-standing problems in astrophysics, referred as the "coronal heating problem". The corona is very faint by several orders of magnitude as compared to the solar photosphere and it is visible to the naked eye only during a total/partial solar eclipse when the photospheric disk is completely or partially obscured by our moon. The coronal region at visible wavelengths observed by the scattered photospheric light is categorized as : i)*K-corona*– scattering by the high energy electrons ii) F-corona – scattering by dust particles in the ecliptic plane iii) Thermal-corona – due to emission from thermally energized electrons. The solar corona can also be divied into three distinct regions based on the heliocentric distance (r) as: i)Low-corona – $r \lesssim 1.2\ R_\odot$; ii) middle-corona – $1.2\ R_\odot \lesssim r \lesssim 2\ R_\odot$; iii) outer corona – $r \gtrsim 2\ R_\odot$. The corona extends further out as a shell structure referred as the 'heliosphere' and merges with the interstellar medium.

1.1.1 Dynamics in the Solar Atmosphere

Most of the dynamical processes that define solar activity have been observed to occur at various regions in the solar atmosphere. As mentioned in previous sections the solar activity is mostly governed by the magnetic field activity in the solar atmosphere. The dynamic events that occur in the solar atmosphere which involve the release of massive amounts of energy and plasma material are called 'solar eruptive phenomena'.

1.1.1.1 Solar Wind

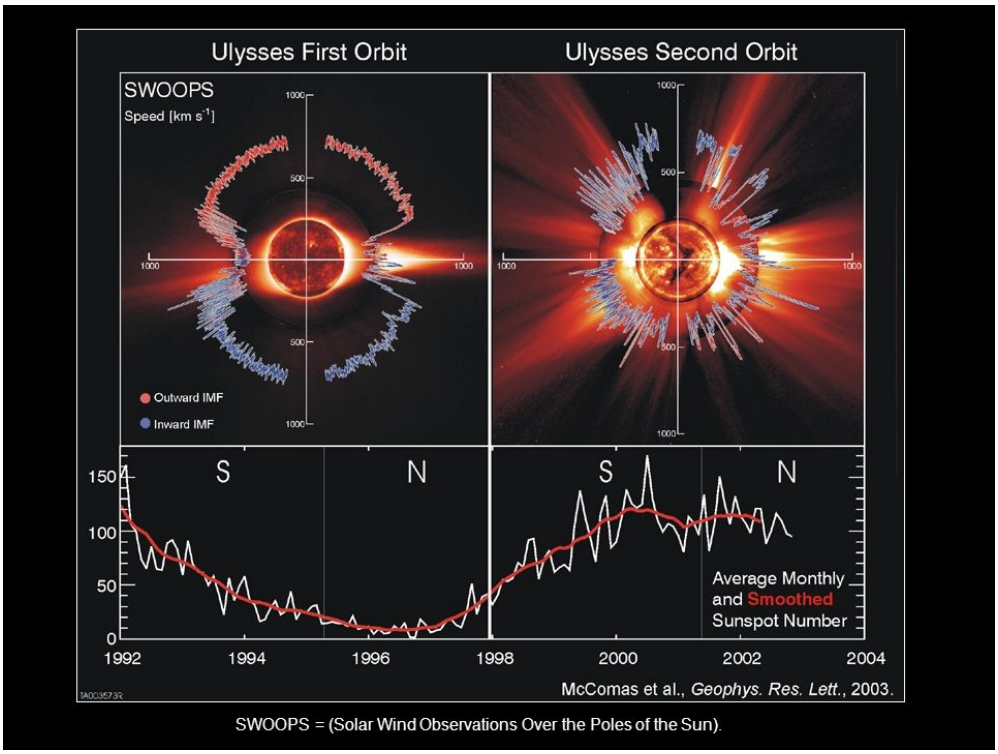

Figure 1.3: The distribution of solar wind and speed as observed by Ulysses spacecraft during solar minimum and maximum periods

Due to the persistent expansion of the solar corona there is a constant outflow of charged particles of plasma from the Sun′s atmosphere. These particles consist mostly of electrons and protons with energies of ≈1 keV and constitutes the ′Solar Wind′ (Figure 1.3). Based on the speed of the particles solar wind can be divided into two categories: 1) The slow solar wind with speeds of ≈ 400 Kms^{-1} and 2) The fast solar wind particle speeds up to ≈ 800 Kms^{-1}. The idea of continuous outflow from the Sun was first suggested by Biermann (1957) in-order to account for the observations of cometary tails pointing away from the Sun. Later, the idea was taken by Parker (1958) and he combined it with the description of heat of the static corona (Chapman & Zirin, 1957) to derive the existence of the solar wind in a model. The magnetic field is advected outwards with the solar wind as the plasma $\beta-$parameter of the latter is larger than one. The radial advection and the solar rotation generates what is known as the Parker spiral in the interplanetary magnetic field

1.1.1.2 Solar Flares

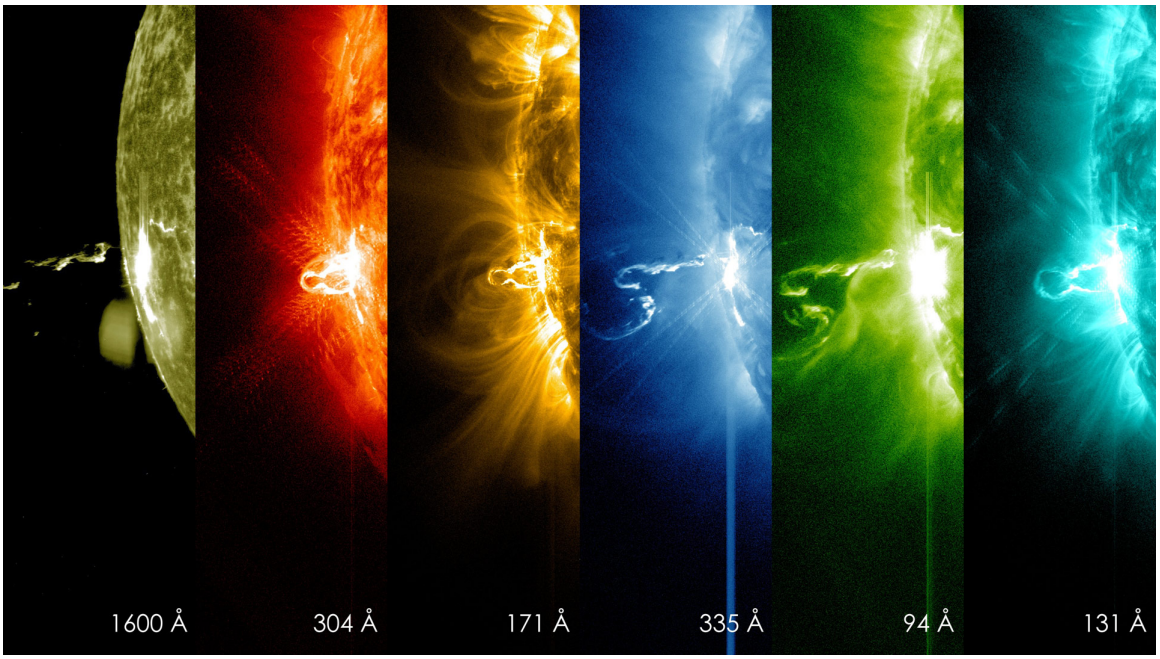

Figure 1.4: Multi-wavelength near-simultaneous snapshots a solar flare obtained from space-based solar observatory

Solar flares are sudden large explosions that occur in the Solar atmosphere with the release of huge amounts of energy ($\approx 6\ \ 10^{25}$ J ; Kopp *et. al.* 2005). On 1, September, 1859 the first recorded observation of a flare phenomenon was made independently by R.C. Carrington and R. Hodgson. They noticed an intense brightening of regions in a complex sunspot group lasting only few minutes during a routine survey of sunspots on the solar disk. They are often observed as enhanced emission in contrast to the background radiation. In the visible wavelengths they are often seen as enhancements in the spectral lines such as Hα, while large amounts of energy are irradiated in EUV and soft X-ray wavelengths as illustrated in Figure 1.4. The Hα flares are categorized on the basis of area (in units of hemispheric square degrees[1] at the time of peak brightness as described in (Table 1.1). A brightness qualifier F, N or B is generally appended to the importance character to indicate faint, normal, or brilliant.

The effects of the solar flares are felt through all the layers of the solar atmosphere, (viz. photosphere, choromsphere and the corona). The solar plasma is heated to tens of millions of Kelvin with the acceleration of particles, viz. electrons, protons, and

[1]One square degree is equal to $\approx 1.214 \times 10^4$ Km^2

Table 1.1: Classification of H-α flares

Area	Optical Class / Importance
≤ 2.0	0
2.1-5.1	1
5.2-12.4	2
12.5-24.7	3
≥ 24.8	4

heavier ions, to relativistic speeds. Flares are observed over the entire electromagnetic spectrum at all wavelengths, from radio waves to gamma rays and mostly occur in active regions around sunspots which harbour intense magnetic fields. It is believed that solar flares are powered by the release of the energy stored within the strong magnetic fields into the solar atmosphere. The X-rays and UV radiation emitted by solar flares can affect Earths ionosphere and disrupt long-range radio communications. The occurrence rate of the flares varies between several per day ($'$active sun$'$) to less than a week ($'$quiet sun$'$) depending on the solar activity cycle. Solar flares are classified as A, B, C, M or X according to the peak flux (in watts per square meter, W/m 2) of 1.0 to 8.0 Å X-rays near Earth, as measured on the GOES (Geostationary Operational Environmental Satellites) spacecrafts. The peak flux of each class is an order of magnitude higher than the preceding one, with X class flares being the most powerful one having a peak flux of order 10^{-4} W/m^2.

1.1.1.3 Coronal Mass Ejection

The magnetic field in the corona shapes the plasma medium there, resulting in the formation of a multitude of large-scale structures exceeding the solar radius, viz. coronal streamers, polar coronal holes and coronal mass ejections (CMEs). CMEs are the most spectacular manifestation of build-up and release of magnetic energy from the Sun (Figure 1.5). These are large scale eruptions of material plasma and magnetic field that propagate the solar corona out into the Heliosphere. A typical CME has a magnetic field strength of $\approx 10^{-6}$ T, mass in the range of $10^{10} - 10^{13}$ kg (Vourlidas *et al.*, 2002) and velocity between $\approx 100 - 2000$ kms^{-1} with some CMEs reaching 3500 kms^{-1} (Yashiro *et al.*, 2004) which are extremely rare. The energies associated with CMEs are in the order of $10^24 - 10^25$ J making them the most energetic events on the Sun$'$s heliosphere (Vourlidas *et al.*, 2002).

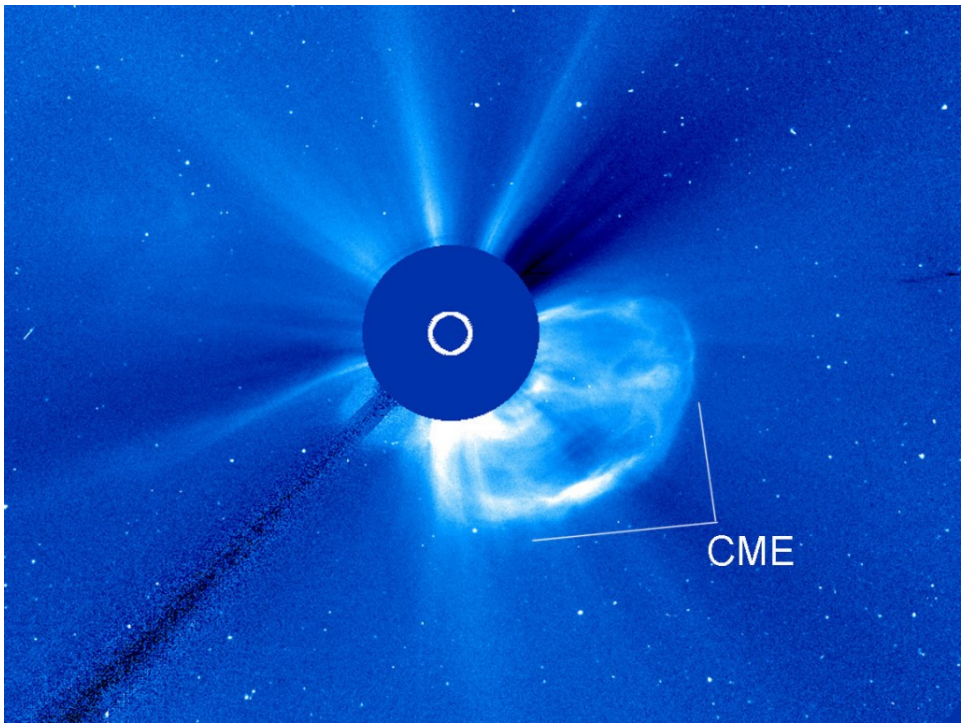

Figure 1.5: A Solar Coronal Mass Ejection as observed from a space-based coronagraph instrument

Although CMEs can have complex morphological structures (Pick *et. al.*, 2006), most CMEs have been observed to show the classic "three-part" structure consisting of bright leading edge, dark cavity, and bright compact core (Illing and Hundhausen, 1960) as illustrated in (Figure 1.5). The CMEs are identified by their position angle (P.A) and projected size ('width') in the plane-of-sky. The position angle of a CME is the angular distance between a reference axis and the mid-point between the frontal structure of the CME. The width of a CME is the angular width of the foot-points. A "plane-of-sky" or limb CME, propagating at right angles to the observer, allows the best measure of their properties such as the width, speed, and morphology without suffering of projection effects. Typical angular width of limb CMEs is approximately 55°, any CME with an angular width greater than $\approx 120°$ is considered as "partial-halo" CME (Burkepile *et al.* (2004); Yashiro *et al.*, 2004). Halo or partial halo CMEs have wider angular extent as they propagate towards the observer and those observed from Earth are of prime importance from the context of 'space-weather'.

1.1.2 Observations of the Solar Atmosphere

Various observational techniques have been proposed and a multitude of instruments

have been developed to observe and study the solar atmosphere. Each of these instruments have been designed to work at various bands over the electromagnetic spectrum to observe different regions of the solar atmosphere. Major solar mission, called the Solar Heliospheric Observatory (SoHO; Domingo, Fleck, and Poland 1995), jointly built by European Space Agency (ESA) and National Aeronautical Space Administration (NASA) was launched in the nineties. The spacecraft had instruments to study helio seismology, solar atmosphere and to monitor the solar wind. Some of the instruments are Solar Ultraviolet Measurements of Emitted Radiation (SUMER) telescope, Coronal Diagnostic Spectrometer (CDS), Extreme Ultra-Violet Coronagraph Spectrometer (UVCS) and Large Angle Spectroscopic COronagraph (LASCO; Brueckner *et al.* 1995). LASCO has the coronagraphs known as C1, C2 and C3 which operate in the range 1.1 - 3$R_\odot$, 2 - 6 $R_\odot$ and 3.7 - 32 $R_\odot$ respectively. Out of the above listed three coronagraphs, C1 is presently not operational. Transition Region And Coronal Explorer (TRACE) is another telescope which operates in the EUV, UV, White light, H I Lyman-α and CIV and provides high spatial resolution images. (Reuven) Ramaty High Energy Solar Spectroscopic Imager (RHESSI) was launched to study the physics of particle acceleration. Review on these instruments with references are given in Aschwanden (2004) and Lin *et al.* (2004). Solar TErrestrial RElations Observatory (STEREO; Kaiser 2005) is another important mission aimed at understanding Earth-directed CMEs. STEREO employs two nearly identical space-based observatories: one ahead of Earth in its orbit (STEREO/A) and the other behind (STEREO/B). STEREO has different instruments: (1) Sun-Earth Connection Cornal and Heliospheric Investigation (SECCHI) whose primary science target is to observe the 3-D evolution of CMEs from close to solar surface through the corona and interplanetary medium including the impacts of CMEs on Earth. (2) SWAVES is aimed to study the interplanetary radio bursts. (3) In-situ Measurements of Particles And CME Transients (IMPACT) and (4) PLasma And Super Thermal Ion Composition (PLASTIC) (STEREO; Kaiser, 2005; Kaiser et al., 2008). The Solar Dynamics Observatory (Pesnell, 2012) is yet another important solar mission that has opened new vistas to understanding our Sun and it was the first satellite to be launched under the Living With a Star (LWS) programme. SDO contains a suite of instruments that provide observations that will lead to a more complete understanding of the solar dynamics that drive variability in the Earth's environment which include the Helioseismic and Magnetic Imager (HMI) to study oscillations and the magnetic field at the solar surface, or photosphere, the Atmospheric Imaging Assembly (AIA) to image the solar atmosphere at multiple wavelengths and the Extreme Ultraviolet Variability

Experiment (EVE) to measure the solar extreme-ultraviolet (EUV) irradiance with unprecedented spectral resolution, temporal cadence, and precision.

Ground based observations of the solar atmosphere are mostly limited to the optical and radio regimes of the electromagnetic spectrum. Using small-scale ground-based optical telescopes the Sun is often observed in particular wavebands like H-α, Calsium-K whose wavelengths correspond to specific spectral lines in the optical solar spectra. H-α observations are primarily useful in identifying active regions, flares and solar prominences. Observations of the low K-corona are also carried out using the white-light ground-based coronagraph instruments. Throughout the world a network of telescopes at various observatories are operated for regular observations of the Sun which include the high altitude sites of the Mauna Loa Solar Observatory (MLSO) in Hawaii, National Solar Observatory (NSO) in Kitt Peak, Solar Observatory Tower in Meudon, Udaipur Solar Observatory (USO), Kodaikanal Solar Observatory in India to name a few.

1.2 Radio Emission from the Sun

The Sun is one of the first astrophysical objects to be studied by our early radio astronomers. Our Sun is the brightest source of radio waves in the sky mainly because of it's proximity to the Earth. It has been observed that radio waves penetrate through the outer layers of the solar atmosphere, viz. the chromosphere and corona, and the depth of penetration depends on the wavelength. Radio radiation is emitted by the solar atmosphere at all wavelengths at all times and it′s total flux density varies with the magnetic activity. Thus observing and studying the sun in the radio wavelength regime offers a unique opportunity to understand the dynamics of the solar atmosphere.

1.2.1 Continuum Emission

The radio emission from the Sun has been identified to consist of two components of radio radiation. One component is the radio emission from the spherically symmetric static solar atmosphere that is observed to vary only slightly over the solar sunspot cycle. This is often referred as the "quiet" Sun (in which active regions are embedded) emission in the absence of solar activity like flares or CMEs. This component of radio radiation is primarily due to the free-free emission from the electrons distributed in the solar atmosphere and follows Rayleigh−Jeans Law,

$$B_\nu \approx \frac{2kT}{\lambda^2} \tag{1.5}$$

The peak brightness temperature[2] from the thermal continuum is $\approx 10^6$K. Another component of radio emission in addition to the non-variable thermal background is the contribution from density condensations over active sunspot regions. The presence of active regions gives rise to a "Slowly Variable Component" (SVC) which is also of thermal origin and has a brightness temperature $\approx 2 \times 10^6$ K. The intensity of the SVC component of the radio emission varies gradually on a daily basis with a period of about 27 days.

1.2.2 Transient Emission

At times the radio emission from the Sun can be impulsive in nature and are often referred as "radio bursts". These are transient phenomena observed to occur over a broad range of frequencies from a few kHz up-to few GHz with very high brightness temperatures in the range 10^{12}-10^{14}K. The radio bursts are primarily non-thermal (Melrose, 1980) and highly coherent in nature, those occurring in the meter-wavelength region have a distinct classification mainly based on their time-frequency characteristics, as described below:

Type−I : This type of impulsive radio emission is referred as solar noise storm emission. It has been observed to consist of two components : i) very short-lived narrow-band (δf / f ≈ 0.025) spikes referred as type-I bursts and ii) A broad-band long-duration enhanced continuum emission that can last for hours or days together. Solar noise storms are one of the most frequently observed type of radio transient in the solar corona at meter wavelengths and found to be associated with active region locations on the Sun.

Type−II : These are observed as slow-drifting (δf/δt ≈ 0.5 MHzs^{-1}) lanes of enhanced radio emission from high-to-low frequency, in dynamic spectral records, with a duration in the range 10−20 minutes. This type of radio transient has been observed to be associated with CMEs and shock waves generated in the coronal and interplanetary medium.

[2]the temperature of a blackbody that would produce the observed radiance at a specific frequency

Type−III : These are generated through plasma oscillations induced by relativistic electron streams travelling along "open" magnetic field-lines. They appear as relativiley fast drifting ($\delta f/\delta t \approx 100$ MHzs^{-1}) enhanced features in the dynamic spectrum with a duration of few 10s of seconds. It has been observed that the Type III bursts can either occur as isolated or in groups and have been found to show a multitude of spectral and temporal features.

Type−IV : These are smoothly varying enhanced radio continuum emissions, often with a broad-frequency coverage. The origin and mechanism of this type of radio burst is still unknown. Based on the time-frequency characteristics they are classified as : i) stationary type-IV burst and ii) moving type-IV burst. The latter has often been associated with material ejecta coincident with CMEs.

Type−V : These are short-duration ($\approx$ 5 minutes) diffuse continuum radio emissions that are observed in the aftermath of type III radio bursts. The longer duration as compared to the type-III radio bursts has been attributed to the distributed velocity profile of the associated relativistic electron streams. Due to the paucity of observations of the this kind of radio burst, studies on Type-V bursts are relatively limited.

1.2.3 Solar Radio Observations

Radio astronomy had its beginning in the early 1930s with the historical observations by Karl Jansky at 20.5 MHz. Subsequent observations by Grote Reber at higher frequencies established radio astronomy as a potential tool to explore and understand many astrophysical problems. However, the use of radio astronomy as a useful diagnostic in solar science began much later, with the announcement of the serendipitous discovery of solar noise storms by Hey in 1942. In the post-world war II period numerous efforts were taken by independent research groups in Australia and Great Britain to make use of the war-time military radar systems as peace-time radio telescopes for solar observations. Pioneering work was carried out especially at low-frequencies in the range 30−300 MHz with the then available instruments. But the need for higher angular resolution and difficulties faced with building large low-frequency radio telescopes prompted radio astronomers to move to higher frequencies.

Radio observations at the shortest wavelengths (sub-millimeter) have historically been performed with single-dish antennas and have therefore been limited in spatial resolution to tens of arc-Sec, except for those that have been recorded during a solar

eclipse, which provides sub-diffraction-limited resolution in one dimension. To date there are a multitude of instruments, sent on-board space-platforms and at ground-based observatories, dedicated for solar observations in the frequency range spanning from a few kHz to a few GHz. These are described briefly in the following sections:

1.2.3.1 Space-based Instruments

Radio observations of the Sun from space-platforms are presently limited to the spectral mode. The Radio and Plasma Wave Investigation (WAVES) instrument on board the WIND spacecraft is the result of a collaboration between the Paris-Meudon Observatory, the University of Minnesota, and the Goddard Space Flight Center (NASA) (Bougeret, 1995). WIND/WAVES consists of electric field detectors and magnetic search coils. The electric field detectors are composed of three orthogonal electric field dipole antennas, two in the spin plane (roughly the plane of the ecliptic) of the spacecraft and one along the spin axis. The complete WAVES suite of instruments includes five total receivers including: Low Frequency FFT receiver called FFT (0.3 Hz to 11 kHz), Thermal Noise Receiver called TNR (4-256 kHz), Radio receiver band 1 called RAD1 (20-1040 kHz), Radio Receiver Band 2 called RAD2 (1.075-13.825 MHz) and the Time Domain Sampler called TDS (designed and built by the University of Minnesota). All of the above instruments are mainly used for dynamic spectral observations of radio transient emission.

1.2.3.2 Ground-based Observing Facilities

Radio imaging observations of the Sun have been successfully carried out using various radio telescopes around the world. The Giant Meterwave Radio Telescope (GMRT) in Khodad near Pune in India is a Y−shaped radio-interferometric array that has been used for solar radio observations, particularly at 327 MHz (Mercier *et al.*, 2015; Prasad *et al.*, 2003). With the recent upgrade activities, the upgraded-GMRT (uGMRT) can observe over a broad range of frequencies from $150 - 1500$ MHz with an instantaneous bandwidth of 200 MHz. The general-purpose Very Large Array (VLA) in the United States of America (USA) with its 27 antennas in a Y−shaped array (similar to GMRT) has been successfully used to observe the Sun with its most compact configurations (Allissandrakis, Kundu and Shevgaonkar 1991; Felli, Lang and Willson 1980; Kundu, Schmahl and Rao 1981; Marsh and Hurford 1980; Shevgaonkar and Kundu 1985). The VLA has been upgraded to the Expanded-VLA (EVLA) with the addition of far-away antennas and improved spectroscopic capabilities, allowing observations anywhere between 1 and 50 GHz. The Russian RATAN-600 telescope (Parijskij, 1993) has

a circular arrangement of 895 antenna-segments that operate between 0.61 and 30 GHz. The large frequency range makes it attractive for solar observations in general, but the one-dimensional scans provide only limited information about the structure of the quiet Sun (Bogod, 1998). The international Atacama Large Millimeter Array (ALMA) which has been recently commissioned in the Chilean Andes with its 64 antennas can observe over ten different bands covering a very broad frequency range of $84 - 950$ GHz. Its spatial resolution of down to $0.0100''$ as well as its spectroscopic capabilities should make it particularly interesting for solar observations (Bastain, 2002, Wedemeyer, 2016). Recently many new radio telescopes have been built and commissioned for science observations, particularly at low-frequencies like the Low Freqency Array (LOFAR: Van Harleem *et al.*, 2013) in the Netherlands, the Murchison Wide-field Array (Tingay *et al.*, 2013) in Australia and the Long Wavelength Array (Ellingson *et al.*, 2013) in the USA. Note that the aforementioned radio telescopes are not solar-dedicated instruments and hence these are not available for regular monitoring of solar activities.

The Japanese Nobeyama Radioheliograph (NoRH) is one of the powerful solar-dedicated imaging radio telescopes (Nakajima *et al.*, 1994; 1995). It provides full disk radio maps of the Sun simultaneously at frequencies of 17 and 34 GHz, with an angular resolution of $10''$ and $5''$, respectively with a time resolution of $\lesssim 0.1$ seconds. The solar-dedicated Expanded Owens Valley Solar Array (EOVSA; Gary *et al.*, 2014) in the USA consists of two 27−m and thirteen 2−m antennae spreading over an area about 1.2 km wide. The receivers can tune to any harmonic of 200 MHz in the range of 1 to 18 GHz, and acquire phase lock in less than 10 ms. Through its rapidly tuning receiver system, provides near-simultaneous observations of an area of the Sun at many frequencies, allowing observations that require spectroscopic capabilities. The planned Frequency Agile Solar Radiotelescope (FASR) is a Fourier synthesis telescope designed to perform imaging spectroscopy over an extremely broad frequency range ($0.1 - 30$ GHz). The frequency, temporal and angular resolution of the instrument will be optimized to study a multitude of radio phenomena originating from the Sun. The French Nançay Radioheliograph (NRH) is another solar-dedicated instrument with a cross-shaped 43-antenna array that images the Sun at six frequencies between 164 MHz and 432 MHz at a rate of 5 Hz (Avignon *et al.*, 1989)

Radio spectral observations of the solar coronal transients are being carried out on a daily basis with dedicated facilities at different locations around the globe. The Radio Solar Telescope Network (RSTN) is a network of solar observatories maintained and operated by the 557th Weather Wing, ACC. The RSTN consists

of ground-based observatories in Australia, Italy, Massachusetts, New Mexico and Hawaii. But there are very limited facilities that operate at frequencies $\lesssim$ 30 MHz (Boischot, 1980; Erickson, 1997; Prestage, 1995; Zucca *et al.*, 2012)[3]. The CALLISTO (**C**ompound **A**stronomical **L**ow cost **L**ow frequency **I**nstrument for **S**pectroscopy and **T**ransportable **O**bservatory) network is a distribution of radio spectrometers based on a dual-channel frequency-agile receiver based on commercially available consumer electronics, at many places around the globe. The total bandwidth is 825 MHz, and the width of individual channels is 300 kHz. A total of 1000 measurements can be made per second. The spectrometer is primarily used for solar low-frequency radio observations pertinent for space weather research. The above mentioned instruments are one of the very few that are dedicated for solar radio observations on a regular day-to-day basis.

1.3 Observational Facilities at Gauribidanur Observatory

The Indian Institute of Astrophysics operates different instruments to carry out solar radio observations in various modes at the Gauribidanur Radio Observatory (GRO) [longtitude : 77°27′07″ E ; latitude : 13°36′12″ N] located ≈ 80 Km North of the city of Bengaluru. All of the instruments operate in the frequency range of 150 − 40 MHz[4] which corresponds to a heliocentric distance range of 1.2 − 1.8 $R_\odot$ in the solar atmosphere (insert figure). Most of the impulsive phenomenon discussed in the previous sections are believed to have their origin in the above-mentioned distance range in the solar atmosphere. The lack of dedicated observing facilities and the limitations posed by the existing instruments has made the above the height range presently inaccessible for observations in other bands of the electromagnetic spectrum. The details of the existing instruments used for solar observations at the GRO are briefly discussed in the subsequent sections

1.3.1 Gauribidanur RAdio heliograPH

The Gauribidanur Radio Heliograph (GRH ; Ramesh *et al.* 1998) is a two-dimensional T-shaped radio interferometric array with two orthogonal arms of well-defined dis-

[3]The Bruny Island Radio Spectrometer (Erickson, 1997) is not in operation since January 2015 (http://www.astro.umd.edu/∼white/gb/)

[4]Note that this is, at present, the only solar-dedicated facility in the world that operating below 100 MHz

tribution of antenna elements extending along the east-west (EW) and south (S) direction. The array is divided into groups of antennas with each group in the EW and S direction consisting of eight and four antenna element with an inter-element spacing of ≈ 10 m and 7 m, respectively. The EW arm of the GRH extends to a length of ≈ 1280 m and the S arm extends to a length of ≈ 440 m. The array underwent augmentation work very recently with additional antenna elements being installed and grouped in the same manner as mentioned above, with extension of the arms along EW and the north (N) directions in order to improve the sensitivity and angular resolution. The array in its present configuration extends to a length of 2480 m in the EW and 880 m in the NS directions. Table 1 shows the details of the GRH and the GRAPH with a comparison of the sensitivity and angular resolution at a typical frequency like 80 MHz. The GRAPH is in regular operation and used for making two-dimensional snap-shot images of the radio emission from the solar corona (Figure 1.6). The radio maps are useful in obtaining the positional information of radio emission from extended and compact structures which are used in conjunction with space-borne coronagraph and EUV imaging instruments (refer Section **1.1.2**) for complimentary studies.

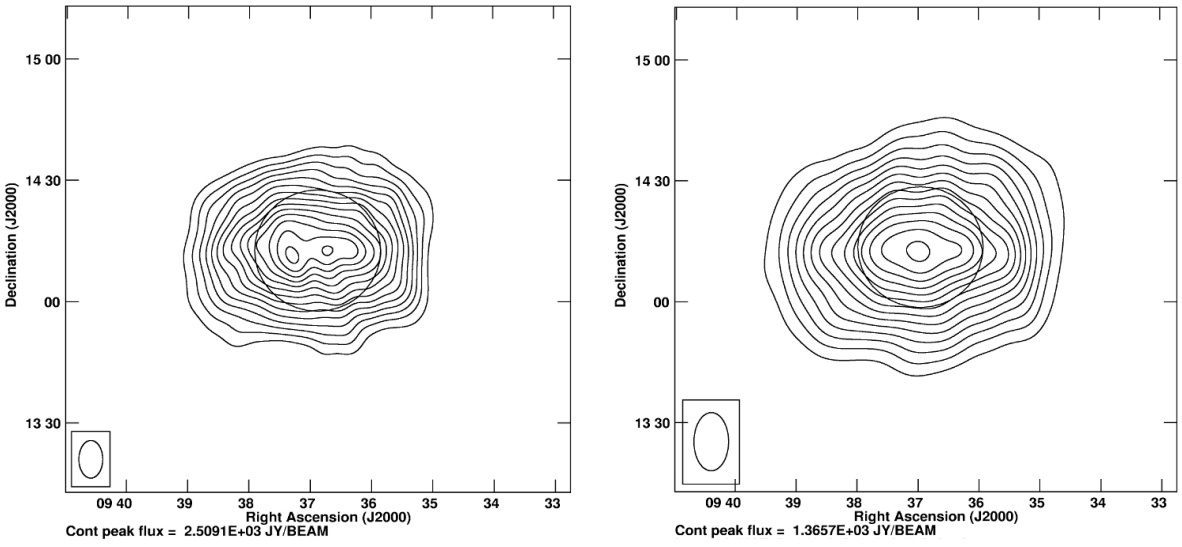

(a) (b)

Figure 1.6: Snapshot Radio Contour map of the Solar Corona obtained on 14, August, 2016 at two spot frequencies: a) 80 MHz; b) 53.3 MHz

1.3.2 Gauribidanur Radio Interferometric Polarimeter

The tenuous coronal plasma is essentially birefringent due to the complex magnetic

field structures there, this splits the electromagnetic wave propagating the medium into ordinary (o) and extraordinary components (e). The differential attenuation of the two components as they propagate the coronal plasma introduces some degree of circular polarization to the radio emission. It has been observed and verified that some of the solar radio bursts can be low ($\lesssim 20\%$) to highly $\approx 90\%$ circularly polarized. The Gauribidanur Radio Interferometric Polarimeter (GRIP; Ramesh *et al.* (2008)) is a one-dimensional radio interferometric array of groups of antenna elements along EW direction which has been set-up and used for measuring the polarized emission signatures of the solar coronal transients. It consists of three groups of antennas, with two groups each of 16 and 8 antenna elements having their dipole arms oriented along the NS direction and a third group of 16 antenna elements with the dipole arms oriented along the EW direction (orthogonal to the other two groups). The three groups of antennas form two pairs of interferometers and the half-power width of the response pattern (″beam″) is approximately $2^\circ \times 90^\circ$ (R.A. $\times$ Dec.) which is very broad compared to the size of the Sun making it a compact source for the array. Therefore a plot of the temporal profile of data from GRIP observations in the transit mode is essentially the ″eastwest beam″ of the array with amplitude proportional to the strength of the emission from the ″whole″ Sun, weighted by the antenna gain in that direction. By measuring the mutual coherence between the pairs of 90° and 0° antenna groups one can record the Stokes parameters I and V which indicate the total and the circular polarized intensity from the radio source which is used in estimating the degree of circular polarization (dcp). The dcp can in turn be used in the estimation of the magnetic field strength at a particular radial distance in the solar corona corresponding to the frequency of observation.

1.4 Motivation

As mentioned in earlier sections the solar transient activity can expel highly energetic particles into the interplanetary medium and if these were directed towards Earth can pose a serious threat to the very existence of life. So it is important to study and understand the solar transient phenomena in the context of Space Weather which is defined according to the U.S. National Space Weather Plan as *the conditions on the Sun and in the solar wind, magnetosphere, ionosphere and thermosphere that can influence performance and reliability of space borne and ground based technological systems and that can affect human life and health* (Schwenn, 2006). Also, one can see that solar-dedicated observing facilities at low-frequencies below 30 MHz are presently

limited and this poses limitations on the near-continuous spectro-temporal coverage of solar radio observations. Some of the reasons for the non-availability of such low frequency observational facilities are the cut-off frequency for radio wave propagation in the Earth's ionosphere, and the technical difficulties related to handling the terrestrial Radio Frequency Interferences (RFI). It would be useful if the observations are available till $\lesssim 15$ MHz as it will minimize the existing gap with observations from the space platforms which as mentioned in previous sections can extend well below frequencies < 15 MHz up-to few kHz. Such observations are useful in addressing some of the important scientific problems on the origin and nature of coronal and interplanetary shocks, the initiators of such shocks and the relationship between the two and their implications on space weather which have not yet been fully investigated (see for eg. Cane *et al.*, 2002; Cane and Erickson, 2005; Carley *et al.*, 2015; Eastwood *et al.*, 2010; Gopalswamy *et al.*, 1998; Gopalswamy and Mäkelä, 2010; Gopalswamy *et al.*, 2005; Leblanc *et al.*, 2001; Melnik *et al.*, 2014; Morioka *et al.*, 2007; Ramesh *et al.*, 2010; Ramesh, 2011; Ramesh *et al.*, 2012; Ratcliffe *et al.*, 2014; Reid and Kontar, 2015).

Observational studies of the radio emission features in the solar corona particularly at low radio frequencies will compliment the observations made at other wave-bands of the electromagnetic spectrum which can be very useful in investigating innumerable scientific problems. Such comprehensive observations can help track the solar activity from the surface level up-to the corona and out into the interplanetary medium which is important from the space-weather perspective. Therefore, the primary objective of this thesis is to develop i) low-frequency radio observing instruments for solar observations close to the local ionospheric cut-off frequency limit at the Gauribidanur Observatory and to implement digital back-end system that can offer high spectro-temporal resolution and dynamic range required for observations in the presence of RFIs in the operating frequency range. and ii) using the data obtained with the instrument to bring out interesting scientific results by combining the data from the existing radio observing facilities and instruments operating at other wavelengths.

Chapter 2

Low-frequency Solar Spectrograph

2.1 Introduction

Radio spectrograph systems are very useful in solar observations to understand the transient activity such as flares and CMEs (Section 1.1.1) in the solar atmosphere through their associated radio bursts. The Sun is a highly variable source both in time and frequency, radio spectrographs offer the best possible way to probe the science of such phenomena. As explained in the previous chapter, solar transients can occur over a wide range of frequencies, $\approx$10 kHz $-$ 10 GHz and most of them are observed with good contrast at frequencies $<$ 500 MHz (Benz, 1993) from ground-based observations. Radio emission at different frequencies have their origin at different heliocentric distance (r) in the solar atmosphere due to the inherent electron density gradient. The morphology of bursts also changes from one frequency to the other in accordance with the above. To obtain data on the radio emission related to flares and CMEs, near-simultaneous observations over a wide range of frequencies is necessary. Various types of radio telescopes (section 1.2.3.2) are constructed for this purpose using antennas (which are based on transmission lines) as the basic receiving element.

2.2 Low-frequency Antenna

Transmission lines are a medium for the transport of electromagnetic energy from source to sink. Co-axial cable, wires, waveguides and optical fibers are examples of transmission lines. The electrical properties of a transmission line changes drastically with length and frequency of operation (refer distributive networks in Jordan and Balmain (1968)]. The characteristic impedance (Z_o) of the transmission line is the ratio of an infinite line voltage to the line current. The power from a source to load

is maximally transferred if the latter is terminated with the characteristic impedance of the transmission line, in accordance with the maximum power transfer theorem. An antenna can be considered to be an open-ended transmission line based structure (Kraus and Marhefka, 2001) of transducive nature that converts a guided electromagnetic wave into free space electromagnetic wave and vice versa. Generally, any piece of conducting wire/structure acts as an antenna, but the radiation characteristics greatly vary according to the dimensions of the structure involved. They are the basic receiving elements of a radio telescope and can come in various shapes and dimensions. According to the reciprocity theorem, the characteristics of a transmitting antenna are exactly the same when it is used as a receiving antenna. The characteristic impedance of any antenna has to match with the source impedance (—Z_s—) as well as the free space impedance to efficiently transceive the electromagnetic radiation radiation.

2.2.0.1 Hertzian Dipole

Antenna principles are considered to be the same irrespective of the size of the antenna with respect to the operating wavelength and can be explained with antennas of small size. As a rule of thumb, when the largest dimension of an antenna is no more than one-tenth of the wavelength ($\lambda/10$) of operation then it can be considered to be "electrically small". The most common structures used in electrically small antennas are the short dipole (or equivalent monopole and ground place), the small loop, and the dielectrically-loaded patch.

Dipole Antenna Dipole antenna is the simplest of all antenna variants and consists of two conductive elements such as metal wires or rods which are called the 'arms' of the dipole. When an alternating voltage signal is fed to the antenna, current flows along the arms of the dipole generating an electric field which is radiated by the antenna. At the end of the terminals the current gets reflected back to feed point thereby superposing with the incident current. This superposition of the incident and reflected current gives rise to standing wave pattern and the ratio of V_{min} to V_{max} of the standing wave is called the Voltage Standing Wave Ratio (VSWR), which is an an indirect measure of impedance. This is because the VSWR and the impedance are related to each other, i.e., the VSWR $= \frac{1+\Gamma}{1-\Gamma}$, where Γ is the reflection co-efficient of the transmission line. The latter is related to the line (Z_L) and source (Z_S) impedances as $\Gamma = |\frac{Z_L - Z_S}{Z_L + Z_S}|$. The level of reflected current is high in case of larger mismatch. In many conventional antennas such as monopoles, dipoles, Yagi-Uda, etc. the impedance

match is found to be over a narrow range of frequencies; therefore they are called as narrow-band antennas. Most of the electrical properties of the antenna viz. the operating frequency, bandwidth, characteristic impedance etc. are determined by the dimensions of it's structure.

Half-wave Dipole Antenna: The half−wave dipole is a dipole antenna formed using metal a metal wire or tube whose end-to-end arm length is half the wavelength of operation. The feed point of such a dipole is the centre with the feeder connected to two quarter-wave elements in line with each other. The voltage distribution of the $\lambda/2$-dipole is positive maximum at one end of the arm reducing to zero at the centre and goes to negative maximum at the other end while the electric-field distribution follows the opposite trend being maximum at the centre and minimum at the ends. And this keeps alternating at the frequency of the sinusoid being fed to the dipole antenna. The typical bandwidth of a $\lambda/2$ dipole is $\approx$ 10 % of the centre frequency ad hence broad-band performance cannot be achieved with a single dipole. Also the electrical properties of such a dipole antenna is often frequency (or wavelength) dependant.

2.2.0.2 Frequency-Independent Antenna

Theoretically, an antenna is considered to be "Frequency-independent" when it′s near-field and far-field characteristics are independent of frequency which happens if the resultant current (incident+reflected) at the feed terminals is constant and lower in magnitude to that of incident, irrespective of the frequency. The far-field contamination is eliminated or reduced in such antennas by ensuring that the residual currents decay to zero after passing through the active region and before entering the the next-higher order radiating region. In-order to eliminate the low-frequency limit such antennas must have an infinitely large aperture and to eliminate the high-frequency limit they must have a very fine and infinitely small feed region. Such antennas are exclusively described by angles in-order to avoid the length dependant scaling and must have a frequency independent feed. Such type of structures have almost identical input impedance, radiation characteristics, etc. throughout the band. According to Babinets principle (Balanis, 2005) on EM waves, the impedance of any radiating antenna combined with its self-complementary structure becomes frequency independent.

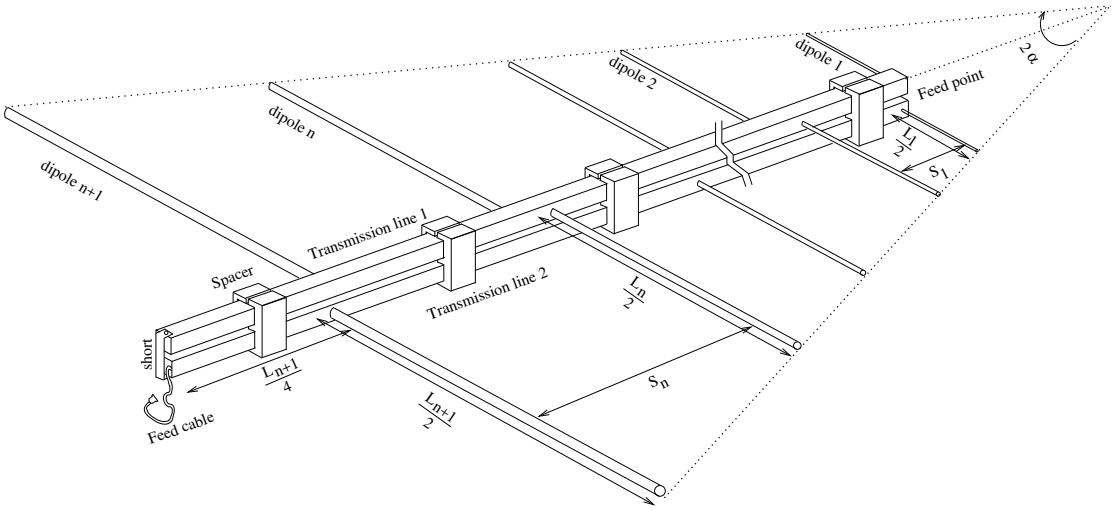

Figure 2.1: Schematic of a Log-Periodic Dipole Antenna

Though designing such antennas of infinite structure is practically impossible, it has been found through various experiments that the the geometry of a structure specified entirely by angles will be ideal for broad-band antenna (Rumsey, 1957). The combined principle of angle-only-specified-geometry and self-complimentary structures lead to the development of Log Periodic Structures (LPS). The log-periodic dipole antenna (LPDA; Figure 2.1) is one such structure that can be used for obtaining broad-band operation and for the spectrograph it was decided to design and fabricate an LPDA to be the basic receiving antenna element.

2.2.1 Design and Fabrication

An LPDA is a series of dipoles stacked together to a transmission line systematically as shown in 2.1 and 2.3. The design of an LPDA is based upon the choice of two primary parameters, the design (or geometric) constant (τ) and the relative spacing constant (σ), as given by Carrel, 1961. Depending upon required directive gain, one can choose a number of combinations of τ and σ (Figure 2.4). If the highest and the lowest operating frequencies are f_n and f_1 respectively with a bandwidth ratio $\beta = \frac{f_n}{f_1}$, then the relationship between the operating frequencies and τ can be derived as follows:

$$f_2 = \frac{f_1}{\tau} \tag{2.1}$$

$$f_{n+1} = \frac{\tau^n}{f_1} \tag{2.2}$$

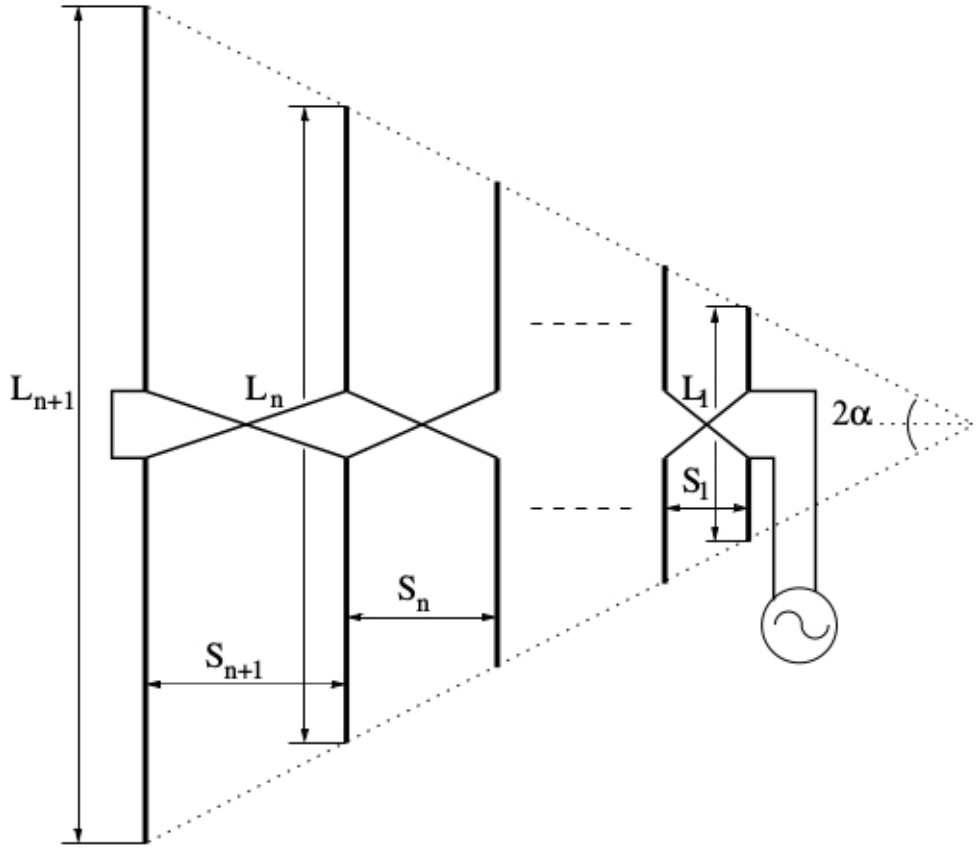

Figure 2.2: Schematic of the Log Periodic Dipole Antenna (LPDA) with an apex angle 2α. The adjacent half-wave dipoles are combined in 'Criss-Cross' manner in order to ensure a phase difference of 180° between the voltage and the current in the adjacent dipoles making the structure self-complementary. As a result, the overall antenna response will be free from cross-talks and interference between adjacent elements and the characteristic impedance remains relatively same over a broad-frequency range in accordance with the Babinet's principle.

$$f_n = \frac{\tau^{n-1}}{f_1} \tag{2.3}$$

$$\log(f_{n+1}) = \log(f_n) + \log\frac{1}{\tau} \tag{2.4}$$

Considering the illustration of an LPDA in Figure 2.2 with an apex angle (2α) with adjacent dipole elements of length L_n and L_{n+1} and inter-element spacing S_n and S_{n+1}, then they are related to the geometric constant (τ) as follows:

$$Ł_n = \tau L_{n+1} \tag{2.5}$$

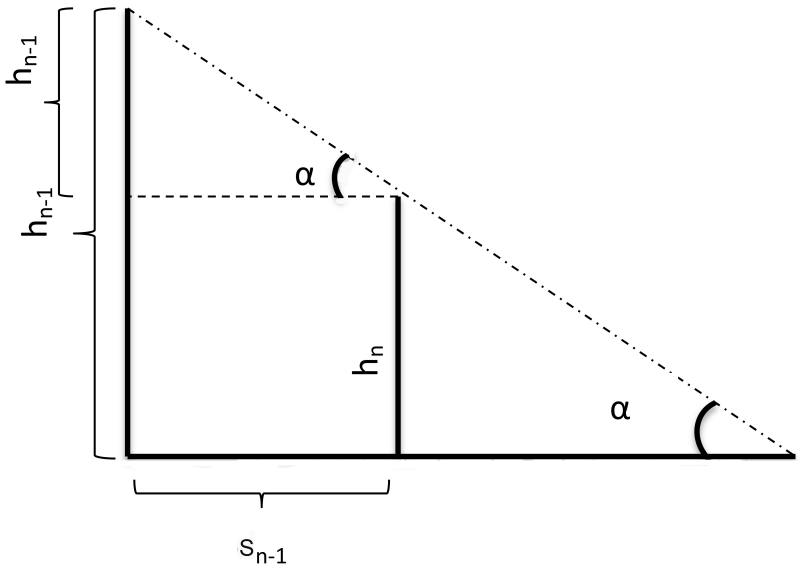

Figure 2.3: Structure Dimension Analysis of the LPDA

$$S_n = \tau S_{n+1} \tag{2.6}$$

$$h_n = \tau h_{n+1} \tag{2.7}$$

$$\tau = \frac{L_n}{L_{n+1}} = \frac{S_n}{S_{n+1}} = \frac{h_n}{h_{n+1}} \tag{2.8}$$

$$\sigma = \frac{S_{n+1}}{\lambda_{n+1}} = \frac{S_{n+1}}{2L_{n+1}} = \frac{S_{n+1}}{4h_{n+1}} \tag{2.9}$$

The relative spacing constant (σ) is given by equation 2.9.

$$S_{n+1} = 4\sigma h_{n+1} \tag{2.10}$$

$$\tan\alpha = \frac{h_{n+1} - h_n}{S_{n+1}} = \frac{h_{n+1}(1-\tau)}{S_{n+1}} = \frac{(1-\tau)}{4\sigma} \tag{2.11}$$

2.2.2 Characteristics of LPDA

Figure 2.5 shows that the VSWR response of the LPDA over the frequency range $15 - 75$ MHz is $\lesssim 2.5$. The half-power beam width of the response pattern of the

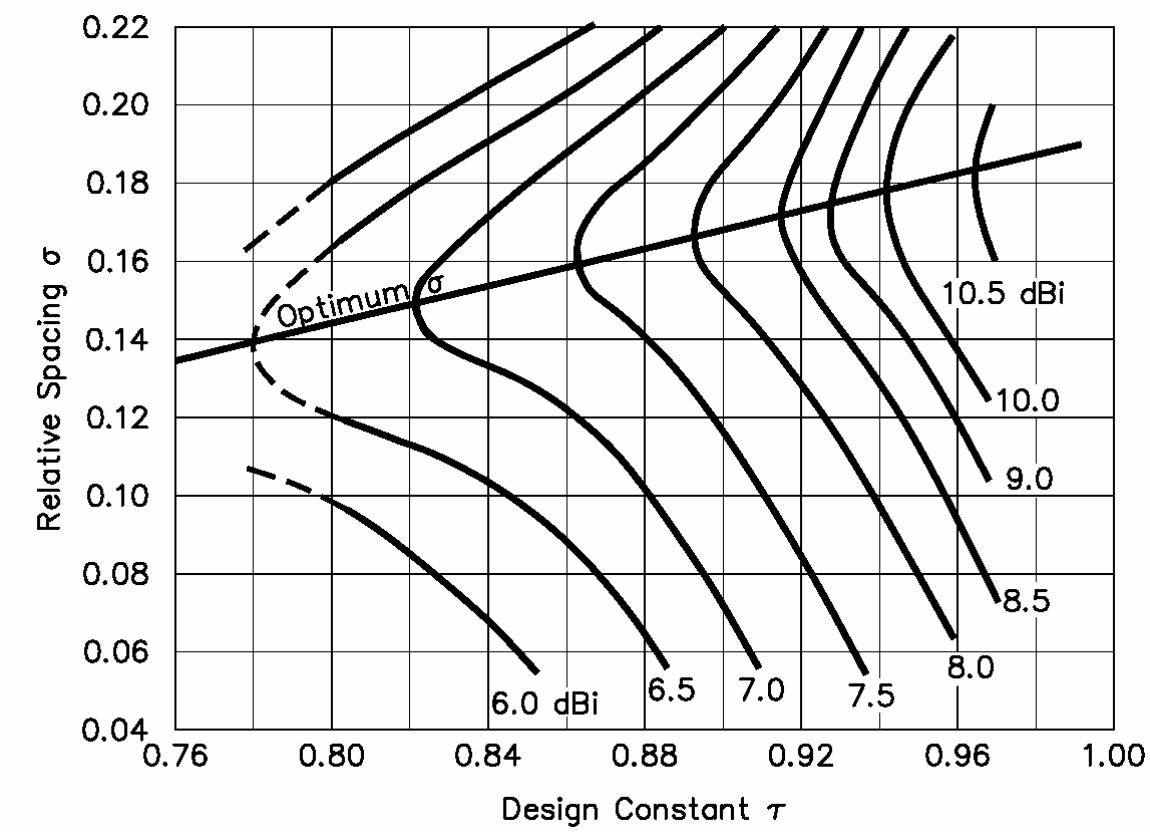

Figure 2.4: Constant Directivity contours (Carrel, 1961) in decibels vs τ and σ

Table 2.1: Specifications of the Log-Periodic Dipole Antenna (LPDA) with $\sigma = 0.056$ and $\tau = 0.78$ over the structural frequency range of $16 - 81$ MHz

Arm Length for the Dipole (cm)	Spacing (cm)	Frequency (MHz)
468.8	105	16
397.5	89	18.9
337.1	75.5	22.2
285.8	64	26.2
242.4	54.3	30.9
205.6	46	36.5
174.3	39	43
147.8	33.1	50.7
125.3	28.1	59.8
106.3	23.8	70.6
90.1	20.2	83.2

LPDAs is estimated to be $\approx 100°$ in both the E-plane and the H-plane. This enables us to carry out observations for longer time duration ($\gtrsim$ 6 h) and over a wide range

of declination. The effective collecting area of each LPDA is $\approx 0.3\lambda^2$, gain is ≈ 5.5 dBi (Carrel, 1961), and the characteristic impedance is $\approx 50\Omega$ over the bandwidth of operation. The above parameters are comparable to that of similar low frequency antennas used elsewhere[1,2].

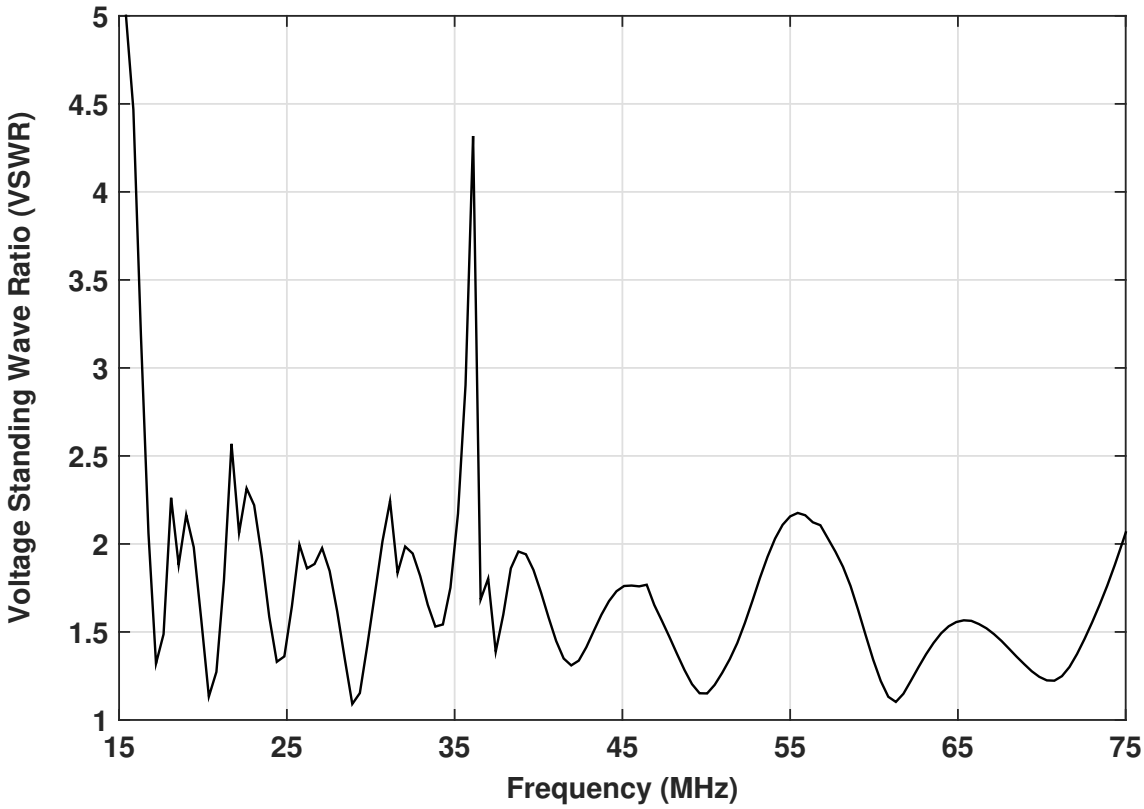

Figure 2.5: VSWR Response of the Low-frequency Log-Periodic Dipole Antenna (LPDA)

2.3 Analog Front-End

The RF signal from the antenna is conditioned in the analog signal chain which consists of the two major sections: i) Low-Noise amplifier and ii) High-pass filter followed by

[1]http://www.lofar.org
[2]http://www.phys.unm.edu/ lwa/index.html

2.3.1 Low-Noise Amplifier

Low-Noise Amplifiers (LNA) form a critical part of the interface between antennas and the subsequent electronic circuitry in wireless signal transmitting and receiving systems. LNA being a principal component in the "front-end" of the receiver channel, it must capture and amplify a very-low-power, low-voltage signal in addition to the random noise fluctuations which is presented to it by the antenna, within the bandwidth of interest.

2.3.1.1 Characteristics of Amplifier

Gain and noise-figure are two important parameters used for characterizing the performance of amplifiers. The gain characteristics of MAN amplifier that is used as an LNA in the present case was derived using the Vector Network Analyzer (VNA). VNA is a sweep-frequency instrument used for the measurement of the network S-parameters viz. S_{21}, S_{11}, S_{12} and S_{22}. The S_{21} represents the "Insertion Loss" (IL) introduced in the signal path and the S_{11} is the "Return Loss" (RL) due to impedance mismatch at the ports of the two-port network circuits.

Amplifier Gain and Return Loss In the case of an amplifier the S_{21} parameter represents the gain of the amplifier. Figure 2.6 shows the broadband response of the MAN amplifier used in the spectrograph set-up. It can be seen that the amplifier offers a gain (G) of ≈ 32 dB over the entire operating band and the RL being $\lesssim -10$ dB shows that the characteristic impedance of the amplifier ports is well matched with that of the RF cable (which is $\approx 50\ \Omega$).

Noise figure Another important parameter that is useful in characterization of amplifiers and receivers is the Noise Figure (NF), introduced by Harald T. Friis, which is a measure of the degradation in the signal−to−noise ratio (SNR) due to additional noise from the amplifier. It is the logarithmic scale of the ratio of SNR at the input of the amplifier to the SNR at it's output. The noise figure of the amplifier used in the present case was measured to be ≈ 3 dB over the frequency range $10 - 100$ MHz.

$$NF = 10 * \log_{10} SNR_{in-linear}/SNR_{out-linear} \tag{2.12}$$

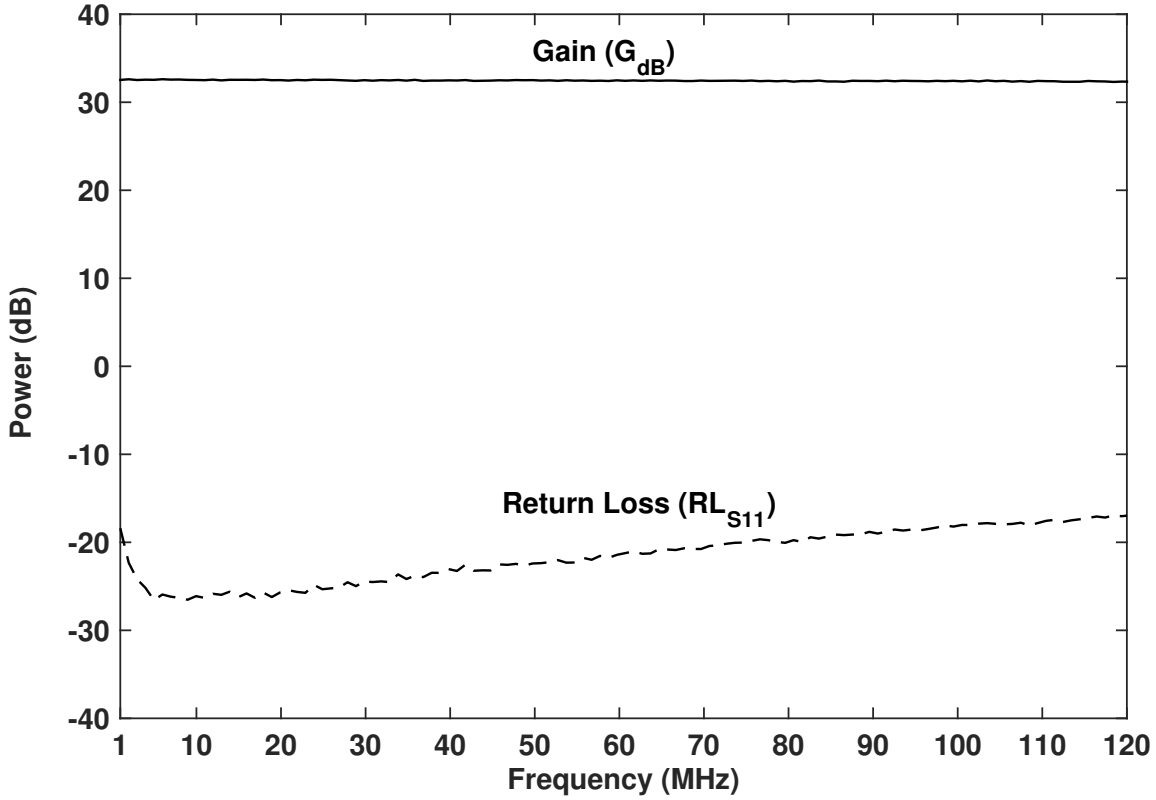

Figure 2.6: Gain and Return Loss Response of MAN amplifier

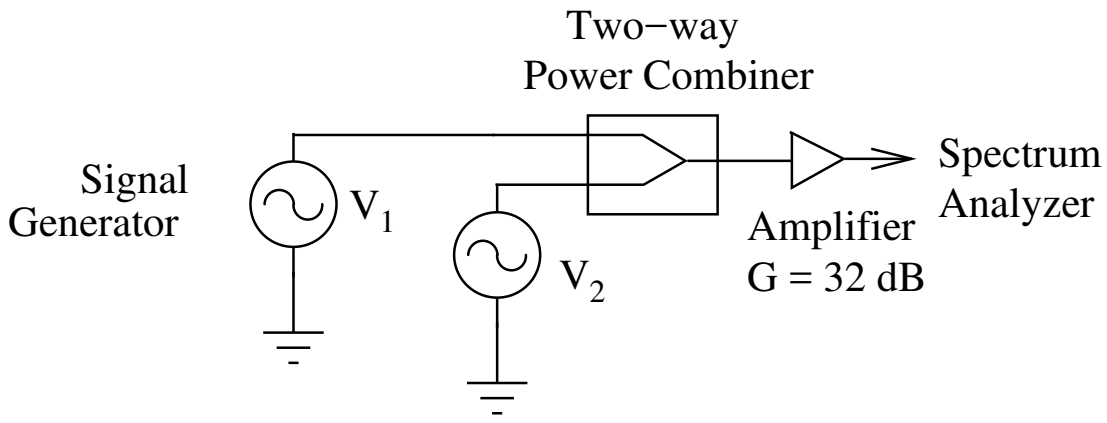

Figure 2.7: Block-Diagram for the experimental set-up for testing inter-modulation distortion effects in the amplifier

2.3.1.2 Inter-modulation Distortion Test

When two or more signals are passed through a two-port network device with a non-

linear transfer function, the spectrum at the output of the device is comprised of the original signals and additional spurious components. The latter can cause interference within the original system or in other systems. When the spurious signals are of sufficient amplitude, they can overpower the signal of interest, resulting in interference and loss of information. The IMD effects are undesirable and more commonly observed in electronic components such as amplifiers and other semiconductor electronics which can be mitigated, by improving the linearity of system components.

We performed a simple test for the MAN amplifier circuit in-order to demonstrate the effects of inter-modulation distortion and to determine the maximum input signal level for the amplifier so that it can still operate within it′s linear range. The block diagram shown in figure 2.7 describes the IMD experimental set-up. Two sinusoidal signals generated from two signal generators are given to a two-way power combiner. The combined signal is then given to the input of the MAN amplifier circuit. The output of the amplifier is recorded in a spectrum analyzer. Figure 2.8 shows the spectrum at the output of the amplifier circuit recorded with a spectrum analyzer with the experimental set-up described in Figure 2.7. Top panel shows the spectrum recorded at the output of the amplifier which comprises the two power-combined CW signals f_1 and f_2 at 30 MHz and 35 MHz, both at a power level of -50 dBm, fed to the input of the amplifier. When the power level of both the signals is increased to -30 dBm one can notice that the spectrum at the output of the amplifier shows spurious harmonic and inter-modulation components in addition to the original signals. This simple experiment clearly demonstrates that when the input signal level is close to the maximum input signal level sustainable by the amplifier for it to operate within its linear range. This is important for low-frequency observations considering the high levels of RFI in the frequency band of interest in the present case.

2.3.2 High-Pass Filter

It has been observed that the spectrum below 30 MHz is populated by AM communication channels and the band below 15 MHz is almost not usable for radio astronomical observations. So to minimize and overcome the undesirable radio interferences and IMD effects in amplifiers, a high pass-filter was designed and fabricated in-house.

2.3.2.1 Design and Fabrication

The cut-off frequency of the high-pass filter was chosen to be 15 MHz in view of the RFI environment and the local ionospheric cut-off frequency at the GRO. It was

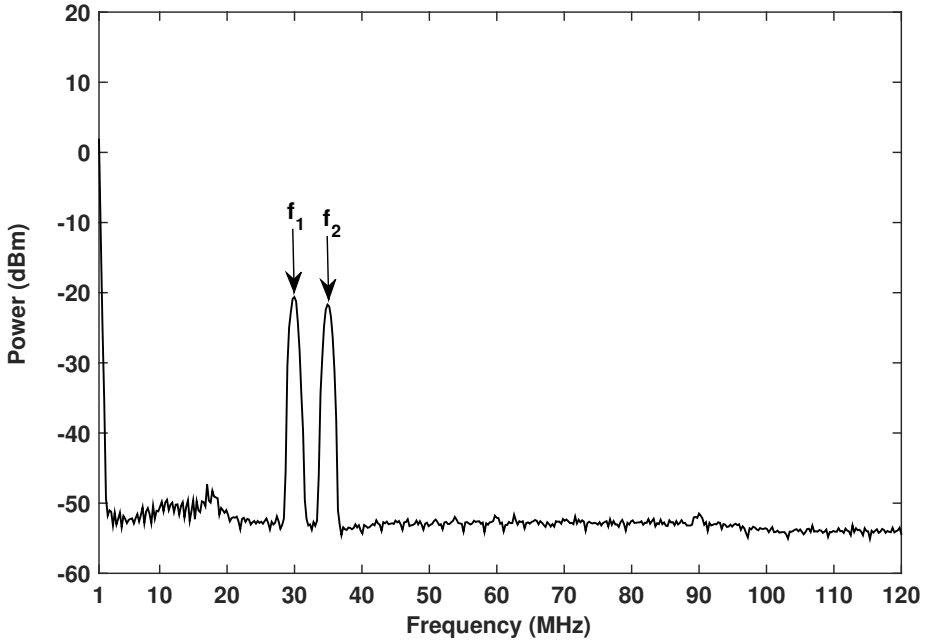

(a)

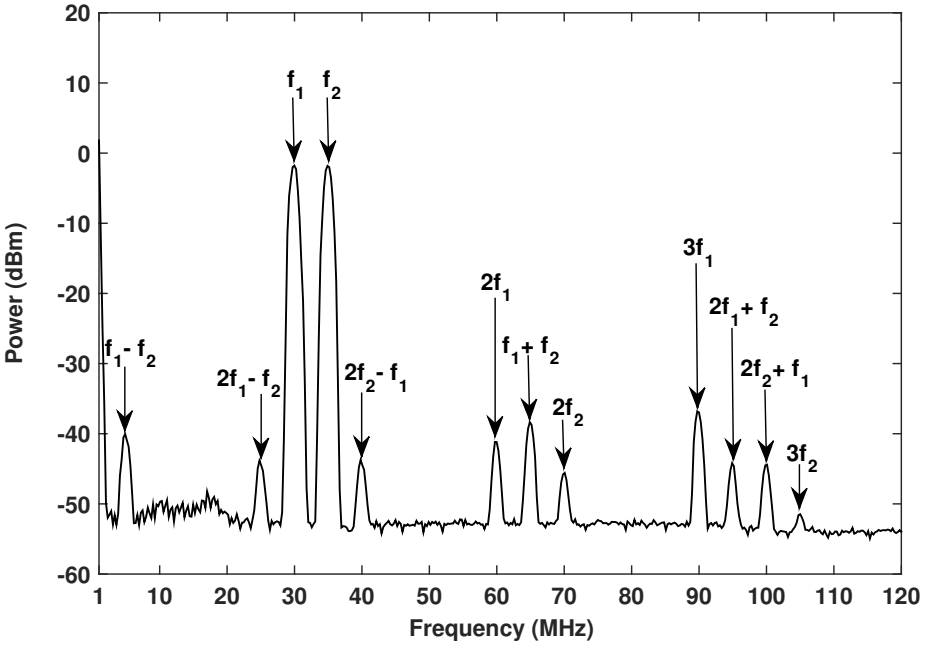

(b)

Figure 2.8: Experimental illustration of Inter-modulation Distortion Test by injecting two CW signals at $f_1 = 30$ MHz and $f_2 = 35$ MHz, a) at a power level of -50 dBm (top panel); b) at a power level of -30 dBm (bottom panel). The latter displays the spectrum of the two CW signals along with the higher-order harmonics and inter-modulation products that generated due to saturation of the amplifier.

decided to design a lumped element filter circuit based T-network and the constant k-filter morphology (figure 2.10) in-order to achieve good impedance matching. The basic and the simplest of the T-network is a L-section filter (figure 2.9) from which the impedance relation is derived as shown below. The values of the lumped elements L and C required to fabricate the circuit are calculated using equations 2.13, 2.14 and 2.18. For a cut-off frequency of 15 MHz the L and C values are calculated to be $\approx$ 265 nH and $\approx$ 212 pF, using these lumped elements the final 5-stage constant-k filter was fabricated and tested.

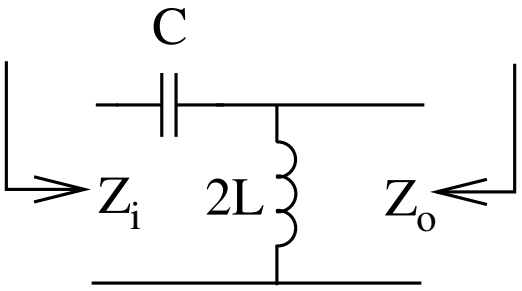

Figure 2.9: Simple L-section of the T-network

$$Z = \frac{1}{\omega C} \tag{2.13}$$

$$Y = \frac{1}{\omega 2L} \tag{2.14}$$

$$Z_i = Z + \frac{1}{2Y + \frac{1}{Z+Z_i}} \tag{2.15}$$

$$Z_i^2 = Z^2 + \frac{Z}{Y} \tag{2.16}$$

$$Y_o^2 = Y^2 + \frac{Y}{Z} \tag{2.17}$$

$$\frac{Z_i}{Y_o} = \frac{Z}{Y} = k^2 = 50^2 \tag{2.18}$$

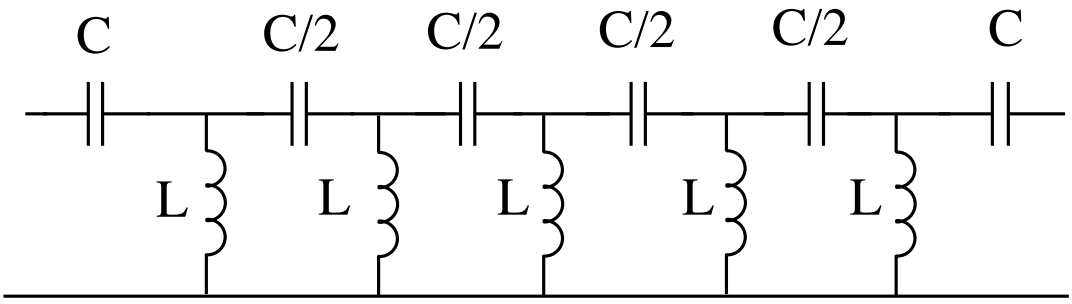

Figure 2.10: High-pass filter Circuit with 5-stages of the T-network to achieve sharp roll-off in the stop-band

2.3.3 Characteristics of High-pass Filter

Figure 2.11 shows the insertion loss and the return loss characteristics of the 5-stage filter designed for the spectrograph application. The insertion loss is found to be ≈ 0.3 dB over the observing band of interest (i.e. 15 - 85 MHz). The roll-off rate in the stop-band is found to be ≈ 68 dB/decade. The return loss over the afore-mentioned band is found to be below −10 dBm which gives a very good impedance match for a characteristic impedance of 50 Ω. Note that the 3dB cut-off point is at f_{3dB} = 16.45 MHz, this deviation in cut-off may be due to the mismatch in values of the lumped element components used in the circuit.

2.4 Single Antenna Spectrograph

A spectrograph was configured using the afore-mentioned analog front-end set-up for regular RFI monitoring and observations of the Sun. The RF signal from the LPDA is passed through the high-pass filter (Section 2.3.2). The filtered signal is then amplified and transmitted to the receiver room via RF coaxial cable buried ≈ 1 meter beneath the ground. In the receiver room, the RF signal is connected to the input of the analog spectrum analyzer (described in following section) which is used as the back-end for the spectrograph system. The specifications of the spectrograph system is given in Table 2.2.

2.4.1 Analog Spectrum Analyzer Back-end

Frequency domain analysis of signals with a spectrum analyzer greatly reduces the amount of noise present in the measurement due to the analyzers ability to narrow the measurement bandwidth. With a frequency-domain view of the spectrum, it

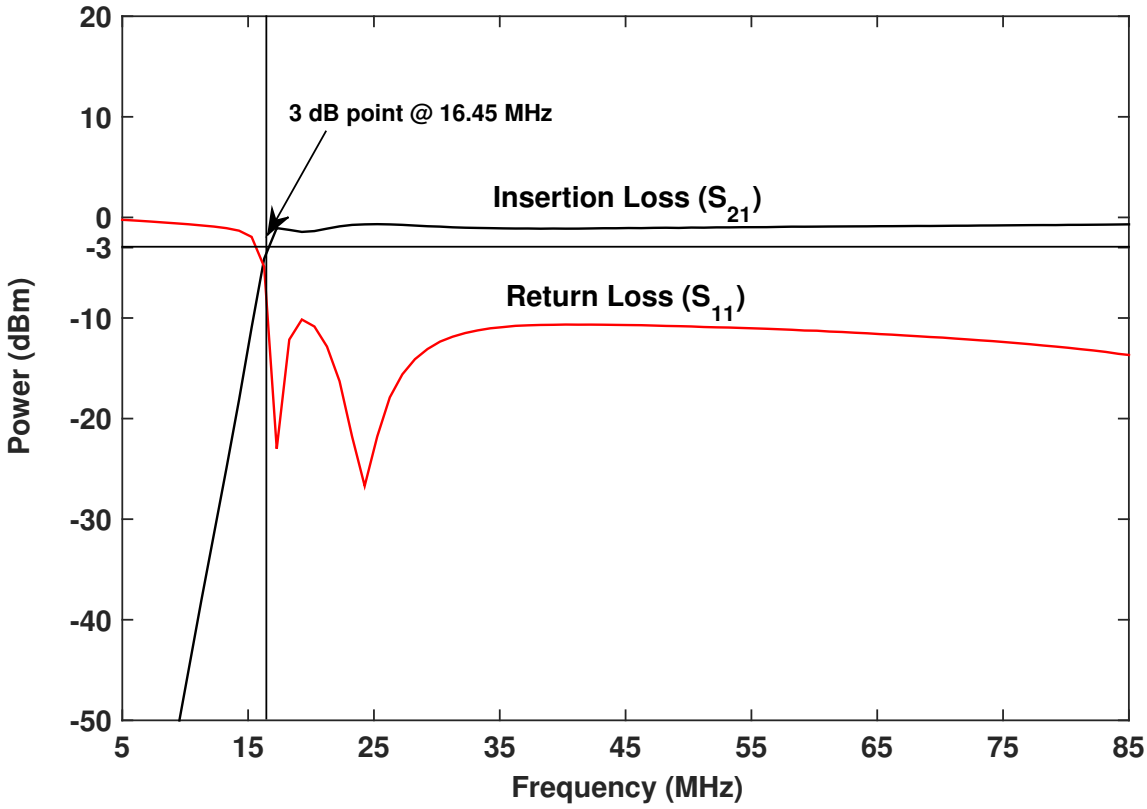

Figure 2.11: Insertion Loss (IL) and Return Loss (RL) Response of the high-pass. Note that the 3 dB cut-off frequency is at $f_{3dB} = 16.45$ MHz

is easy to measure a signals frequency, power, harmonic content, modulation, spurs, and noise. With these quantities measured, total harmonic distortion, occupied bandwidth, signal stability, output power, inter-modulation distortion, power bandwidth, carrier-to-noise ratio, and a host of other measurements then can be determined using just a spectrum analyzer.

For the spectrograph set-up we made use of a commercially available Agilent E4401B (9 kHz-1.5 GHz) analog spectrum analyzer as the back-end receiver. Analog spectrum analyzers are based on the super-heterodyne principle and it is often referred as a 'sweep-tuned analyzer' which "sweeps" across the frequency range of interest, displaying all the frequency components present in the input analog signal. This enables measurements to be made over a large dynamic range and wide frequency range. Figure 2.12 shows the block diagram of the internal circuitry of a sweep-tuned analyzer. The analog input signal passes through an RF-attenuator section followed by a pre-selectable low-pass filter section. The filtered signal is then converted from

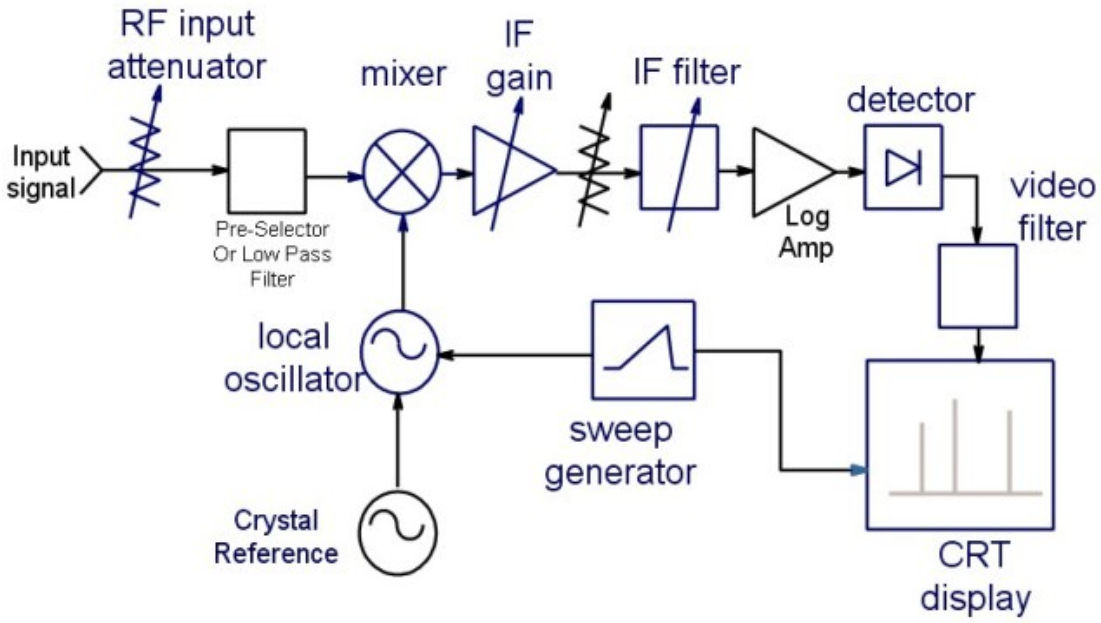

Figure 2.12: Block Diagram of sweep-frequency based analog spectrum analyzer

one frequency to another in a mixer, which is a three-port device with the input signal applied to one port and a local oscillator's (LO) output signal applied to another. Due to the non-linearity of the mixer frequencies that were't present at the input will be present at the output which are the sum and difference frequencies of the two signals in addition to the input signals to the mixer. The difference frequency is called the 'Intermediate frequency' (IF) signal. The IF filter of the analyzer is a bandpass filter section used as a "window" for detecting signals whose bandwidth is user-selectable and it is the analyzer's resolution bandwidth (RBW). A broad range of variable RBW settings allows the analyzer to be optimized for different sweep and signal conditions and enables the user to trade off frequency selectivity, signal-to-noise ratio (SNR), and measurement speed. The IF signal is then converted to a baseband (or video signal) by an envelope detector which is then digitized by the ADC and represented as the signal's amplitude on the Y-axis of the analyzer display. The digitized IF signal is recorded to a computer that is interfaced with the spectrum analyzer through GPIB peripheral interface connections. The parameters for setting-up of the observation and the data acquisition are performed through Agilent Vee-Pro software module.

Table 2.2: Specifications of the Single Antenna Spectrograph System

Frequency Range	15−85 MHz
Number of frequency channels	401
Frequency Resolution	175 kHz
Sweep Time	100 ms
Dwell time	30.9
Data transfer	250 μs
ADC resolution	8-bit

2.4.2 Dynamic Spectrum at Low-frequency

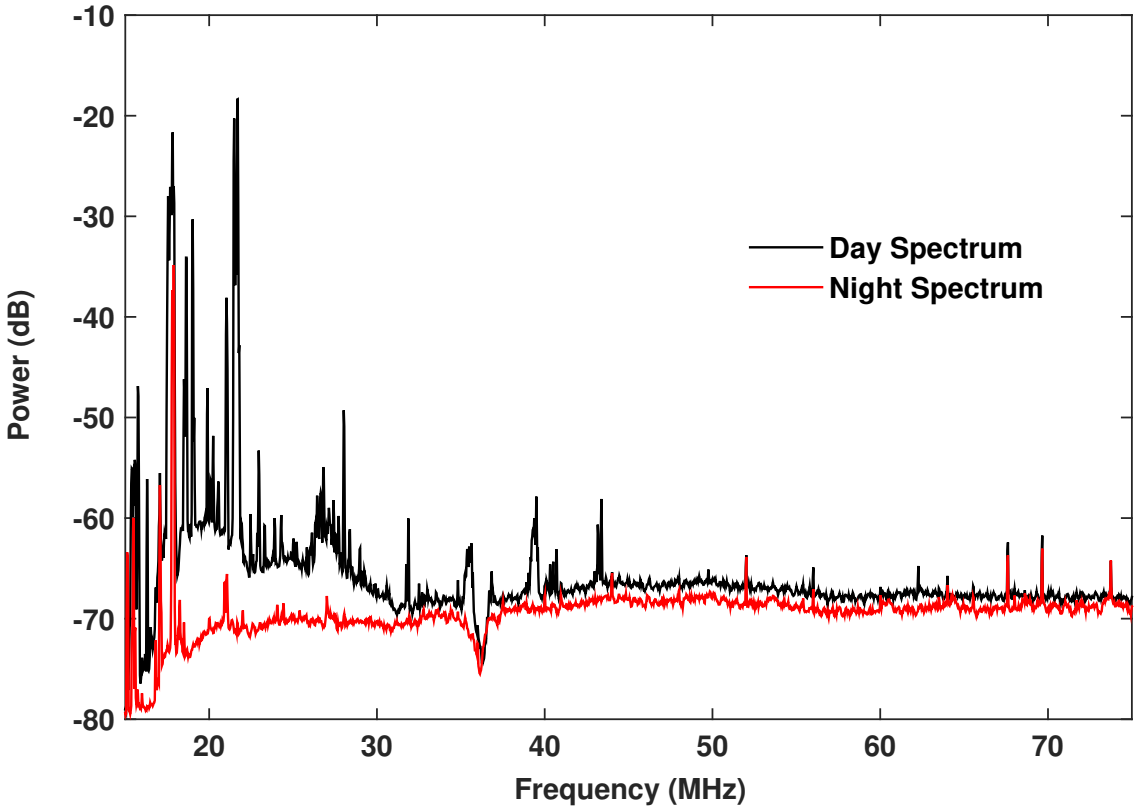

Figure 2.13: Radio spectrum at the GRO over the frequency band 15 − 75 MHz during day and night

Preliminary observations were carried out over 24 hours during the commissioning phase of the spectrograph system described in section 2.4. The dynamic spectrum was recorded over the frequency band of 15−75 MHz during day and night to monitor

the RFI environment at the GRO. It can be noted from Figure 2.13 that the RFI levels are quite high during day and the spectrum is relatively quiet during night. As can be seen, there are small interference free frequency channels amidst the crowd of RFI at the low-frequency side which can very well be made use of for radio astronomical observations. This is of particular advantage to us since we were interested in the low-frequency observations of solar bursts which as mentioned in earlier chapter, are purely non-thermal and hence quite bright at low-frequencies.

2.5 Summary

A log-periodic dipole antenna operating in the frequency range 15−85 MHz was designed and fabricated in-house at the GRO. Analog front-end electronic circuits viz. filters, amplifiers were designed, characterized through lab-tests. A single antenna spectrograph was configured using these components and commercially available spectrum analyzer as the back-end receiver. Since the instrument was commissioned to observe low frequency solar transients, daily observations over an 8-hour period was carried out to maximize the on-source time which maximizes the detection probability. In chapter 3 we describe the observations of solar type-II radio bursts using the low-frequency spectrograph system and the scientific results inferred from the observations.

Chapter 3

Radio Signatures of Coronal Shocks

3.1 Introduction

Solar Type-II radio bursts are electromagnetic signatures of magneto-hydrodynamic (MHD) shocks propagating outward in the solar atmosphere. These bursts have been of particular interest and studied extensively from the time of their discovery by Payne-Scott, Yabsley and Bolton (1947). The bursts are often observed as two slow-drifting narrow-band stripes of enhanced radio emission from higher (several hundred MHz) to lower ($\lesssim$ 20 MHz) frequencies with a timescale of tens of minutes and a frequency ratio of $\approx$ 1:2, in dynamic spectral records. Claβen and Aurass (2002) proposed that a Type-II radio burst could be due to either blast wave shocks driven by the associated flare or shock waves driven by the leading edge and/or the flanks of the associated CME. However, the most accepted emission scenario for type II radio burst involves acceleration of supra-thermal electrons by an MHD shock which causes excitation of Langmuir (plasma) waves in the coronal plasma, these Langmuir waves convert into escaping electromagnetic radiation at the local electron plasma frequency (F) and its harmonic (H) through various non-linear processes. The observed frequency drift from high to low-frequency (typically 0.1 MHz/s, see Mann, Classen and Aurass, 1995; Gopalswamy *et al.*, 2009) results from the decrease of the coronal electron density (N_e) and hence the electron plasma frequency, with increasing distance (r) in the solar atmosphere. The observed drift rate can be converted into the speed of the associated MHD shock if N_e(r) is known.

The spectral observations indicate that the appearance of the type II radio burst can vary drastically as described below.

Split-band structure : In some cases, either or both of the F and H bands are split into two sub-lanes (upper lane, U and lower lane, L) with a separation in frequency usually smaller than that between the F and H bands. This was first reported by Robinson and Sheridan (1982). The band-splitting feature is attributed to the radio emission originating in the corona ahead of and behind the MHD shockfront (Smerd, Sheridan and Stewart, 1975; Vršnak *et al.*, 2001) close to the leading edge (LE) of the associated CME. The corresponding coronal region is referred to as either the upstream/downstream corona or the pre-shock/post-shock corona with respect to the LE of the CME.

Herring-bone structures : Sometimes a second component from apparently much faster propagating features accompanies the main type II trace ("backbone") in the dynamic spectrum. It appears as rapidly drifting (some 10 MHz/s) stripes of enhanced radio emission from the backbone towards both high and low frequencies. These are called "herringbones" (Roberts, 1959) and are generally interpreted as signatures of electron streams that propagate away from and/or toward the Sun along open magnetic field lines after acceleration in the corona ahead of and/or behind the MHD shock front responsible for the type II burst. Type II bursts with herringbone structures are less frequent ($\lesssim 20\%$) and are observed mostly at low frequencies.

Multi-lane Type-II Burst : Another rare variant of the type II radio burst is the Multi-lane type II radio burst (or "multiple type IIs"), first studied by Robinson and Sheridan (1982). They suggested that multiple Type-II bursts are likely to be produced by a single shock travelling through different coronal structures. These are events with two or more lanes of type II radio bursts which have a short duration (usually within $10 - 20$ min). In these events, the type II lanes are not related to each other in a manner like the fundamental and harmonic branches, or split-band structures described above. The lanes or bands observed in multiple type-IIs usually have different start times and frequencies, drift rates, and morphological features. Both statistical and specific case studies have been conducted to explore the origin of multi-lane type IIs. Based on the observations and simulations, it has been suggested that different lanes in a multiple type II burst may be caused by different drivers such as, 1) *flare and a CME* – the different components are driven by a flare bast wave and a shock driven by a CME; 2) *two successive CMEs* - different lanes are associated with shock driven from multiple solar eruptions; 3) *different regions of the*

same shock-front - different lanes are from different sections of a single shock front that is generated by either a flare or a CME.

The reader can find a more detailed description on the characteristics of solar type II radio bursts in Roberts (1959), Wild, Smerd and Weiss (1963), Nelson and Melrose (1985), Mann, Classen and Aurass (1995), Aurass (1997) and Gopalswamy (2006). I would like to note here that the band-splitting and herringbone structures have also been interpreted to be due to other reasons and the interested reader is encouraged to read the following articles by Stewart and Magun 1980; Holman and Pesses 1983; Zlobec *et. al.* 1993.

In the subsequent sections we present the observations of two Type-II radio bursts that were recorded using the spectrograph set-up described in section 2.4 on two different days. We also present a complete analysis of the radio data in addition to observations from space-based instruments and the interpretation of the results based on the above.

3.2 Split-band Type-II Burst : Event of 2013 May 02

3.2.1 Observations

Figure 3.1 shows the dynamic spectrum of a typical split-band type II burst observed with the low-frequency spectrograph set-up (refer chapter 2) on 2013 May 2 during the interval 05:06−05:18 UT over the frequency range 85−25 MHz. The splitting of the F and H components into lower(L) and upper(U) bands, i.e., F_L , F_U , H_L , and H_U, can be clearly noticed in the spectrum. The onset frequencies of the F_L and F_U bands are approximately 50 MHz and 60 MHz, respectively, at 05:06 UT. They are last noticed at approximately 25 and 30 MHz at 05:12 UT and 05:15 UT, respectively. The H_L and H_U bands are observed from 05:06 UT and 05:08 UT, respectively, at 85 MHz. They are last noticed at 35 and 55 MHz at 05:18 UT. The frequency ratio of the F_L , F_U , H_L and H_U bands estimated from the mid-frequencies (f_l , f_u , h_l and h_u) of the corresponding bands in the spectrum at 05:10 UT are f_l : $h_l \approx$ 1:2 and f_u : $h_u \approx$ 1:1.8 (see Figure 3.3). The ratio of the corresponding instantaneous bandwidths F_L : H_L and F_U : H_U are ≈ 1:1 in both the cases. However, the ratio of the bandwidths of the lower and the upper bands within the F and H components, i.e., FL : FU and HL : HU are in the ratio ≈ 1:2. Zimovets *et. al.* (2012) had recently reported H_L : $H_U \approx$ 1:3 for the high- frequency (≈ 150 − 450 MHz) split-band type II burst

reported by them. In addition to the split-band structure of the type II burst, one can observe rib-like features emerging particularly from the FU band in the present case (Figure 2). These are the herringbone structures mentioned in Section 3.1. The herringbones from the other bands are probably too weak to be noticed. The higher intensity of the FU band in Figure 3.3 indicates this. Similar higher intensity of the upper band as compared to the lower band in a split-band type II burst was recently reported by Zimovets *et. al.* (2012). The presence of herringbones in the F_U band, and its likely harmonic components in the H_U band, could be a reason for their larger bandwidths compared to the F_L and H_L bands. The drift of the herringbones toward higher frequencies in the present case is an indication of energetic electrons escaping along magnetic field lines behind the MHD shock front (Wild, Smerd and Weiss, 1963). An inspection of the e-CALLISTO solar radio spectrometer (Benz *et al.*, 2009) observations at the Gauribidanur observatory in the frequency range $45 - 440$ MHz revealed that the above type II burst was limited to frequencies 150 MHz.

Figure 3.4 shows the GRAPH observations of the type II burst at 05:07 UT superposed on the *SOHO*-LASCO C2 and the SDO-AIA difference images obtained at 05:36 UT and 05:34 UT, respectively. The centroid of the burst is at 2 ± 0.2 $R_\odot$ and its peak T_b is $3.7 \pm 0.3 \times 10^9$ K. Since the dynamic range of the GRAPH is limited to approximately 20 dB (Ramesh *et al.*, 1999), radio emission from the background corona is not noticeable in the GRAPH observations. The half-angular width of the burst is $\approx 9'$. This is consistent with the size of the type II bursts at 80 MHz reported in the literature (Nelson and Melrose, 1985). A comparison with Figure 3.1 indicates that type II burst in Figure 3.4 corresponds to the H_L band. We also generated a radioheliogram using GRAPH data obtained around 05:09 UT, the epoch during which the 80 MHz emission is from the H_U band of the type II burst (see Figure 3.1). Given the coarse angular resolution of the GRAPH, we did not observe any significant shift in the location of the centroid of the burst compared to that in Figure 3.4. Having said so, we would like to note here that even the spatially resolved observations indicate only $1'$ separation between the two sub-bands in a split-band type II burst (Zimovets et al. 2012). The enhanced white-light emission above the occulting disk of the coronagraph in Figure 3.4 corresponds to a CME. It was associated with a 1N class Hα flare and M1.1 class GOES soft X-ray flare from AR 11731 located at N10W25.

Note that any error in the position of the type II burst in Figure 3.4 due to ionospheric effects and/or scattering (irregular refraction due to density inhomogeneities

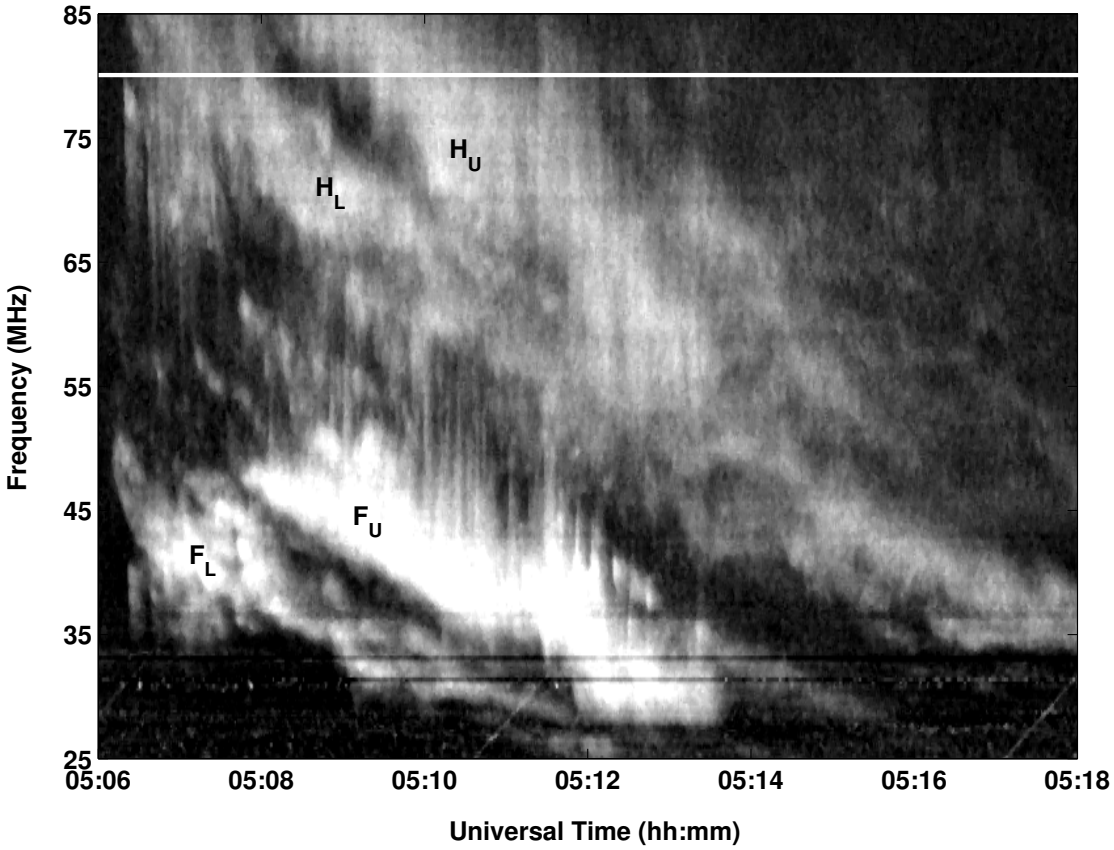

Figure 3.1: Dynamic spectrum (85 − 25 MHz) of the type II radio burst from the solar corona obtained with the GLOSS on 2013 May 2 during the period 05:06 − 05:18 UT. The F and H components of the type II burst with band-splitting and herringbone structures (from the F_U band) are clearly noticeable. The labels F_L, F_U, H_L and H_U on the backbone of the type II burst represent the lower and upper bands in the F and H components of the type II burst. The white horizontal straight line indicates the 80 MHz observations in the spectrum. The other horizontal lines in the spectrum are due to local radio frequency interference.

in the solar corona) is expected to be minimal (0.2 $R_\odot$) and within the angular resolution limits of the GRAPH because (1) positional shifts due to ionospheric effects is expected to be 0.2 $R_\odot$ at 80 MHz in the hour angle range ± 2 hr (Stewart and McLean, 1982). The GRAPH observations are within this hour angle range since the transit of the Sun over the local meridian at Gauribidanur occurs around 06:30 UT; (2) the effects of scattering are considered to be small at 80 MHz compared to lower frequencies (Aubier, Leblanc and Boischot 1971; Bastain 2004;Ramesh *et al.* 2006). High angular resolution observations of the solar corona indicate that discrete radio

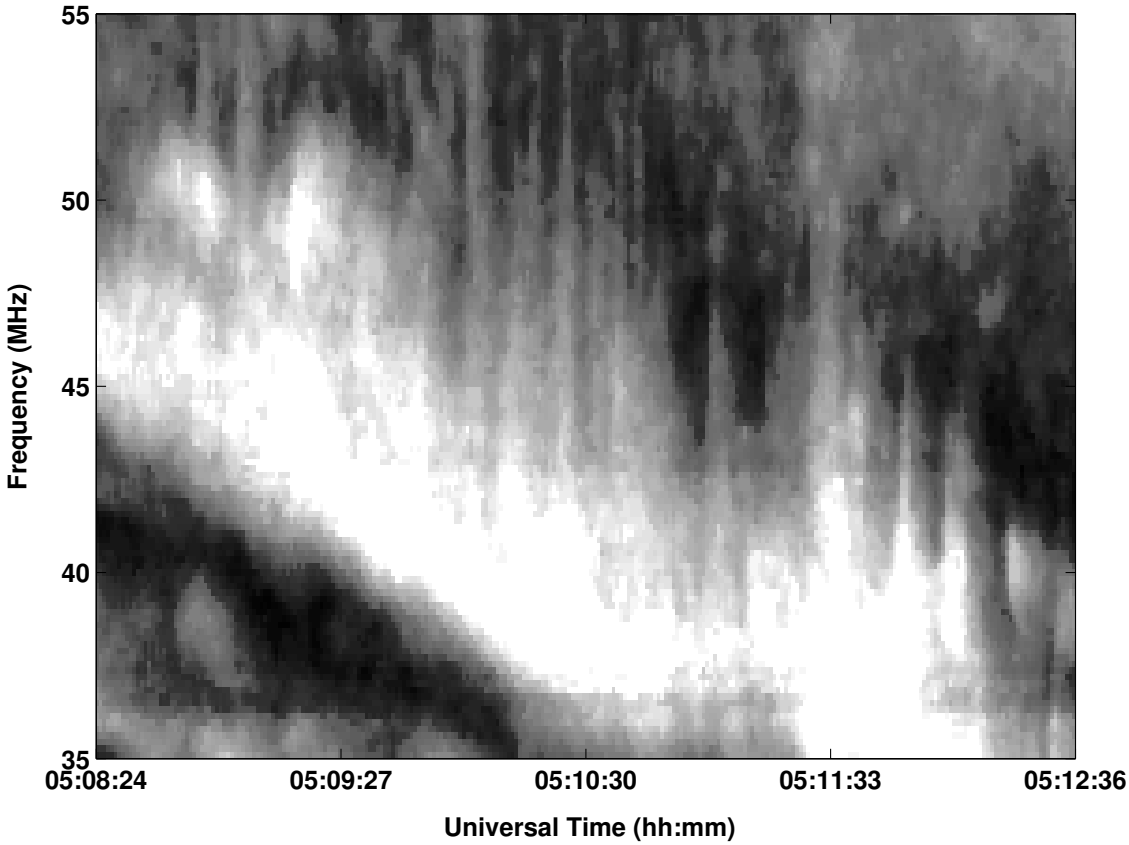

Figure 3.2: Close-up view of the 55−35 MHz range of the F_U band in the dynamic spectrum in Figure 1. The herringbone structures drifting toward higher frequencies from the backbone can be clearly noted.

sources of angular size $\approx 1' - 3'$ are present in the solar atmosphere from where low-frequency radio radiation originates (Kerdraon 1979;Lang and Wilson 1987;Willson *et al.* 1998;Ramesh, Subramanian and Sastry 1999;Ramesh and Sastry 2000;Ramesh and Ebenezer 2001;Ramesh *et al.* 2012;Mercier *et al.* 2006;Kathiravan *et al.* 2011); and (3) the positional shift of discrete solar radio sources due to scattering is expected to be 0.2 $R_\odot$ at 80 MHz (Riddle 1974;Robinson 1983). Ray tracing calculations employing realistic coronal electron density models and density fluctuations show that the turning points of the rays that undergo irregular refraction almost coincide with the location of the plasma ("critical") layer in the non-scattering case even at 73.8 MHz (Thejappa and MacDowall, 2008). Obviously the situation should be better at 80 MHz.

The first appearance of the CME in the coronagraph field of view (FOV) was

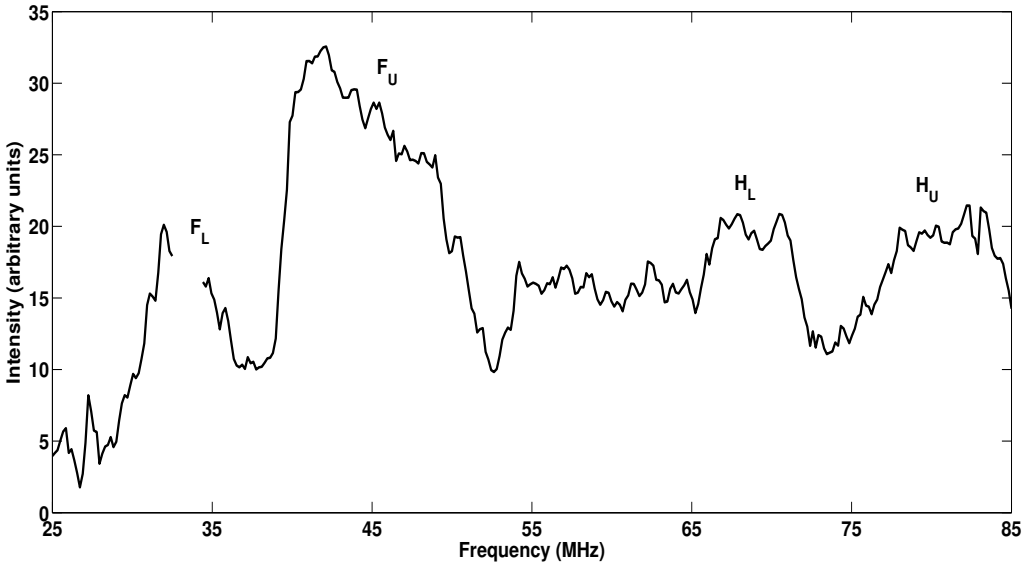

Figure 3.3: Spectral profile of the type II burst in Figure 3.1 at 05:10 UT.

around 05:24 UT. The LE of the CME was measured to be at 2.7 $R_\odot$ at that time. Its central position angle (measured counter clockwise from the solar north) was 344° . The CME exhibited an acceleration of 1.1 ms^2 . The second-order fit to the heighttime measurements of the above CME indicates that its LE was at r = 2 $R_\odot$ around 05:07 UT. We verified this independently with the STEREO observations. Figure 3.5 shows the composite of the STEREO A-COR1 and STEREO A-EUVI 195 $\mathring{A}$ images obtained around 05:10 UT on 2013 May 2. The intense patch of emission seen to the left of the coronagraph occulting disk corresponds to the CME. Its LE is around 2.1 $R_\odot$. Note that *STEREO A* was ahead of Earth at W135 during the above epoch.So the flare location corresponds to E110 from STEREO A view. This is just behind the limb, so the CME measurements in STEREO A-COR1 are less affected by projection effects (Gopalswamy *et al.*, 2013). The height of the CME LE in the STEREO A-COR1 FOV at 05:10 UT agrees with the location of the centroid of the type II burst at 80 MHz around 05:08 UT (Figure 3.4) and the extrapolated CME LE location in the *SOHO*-LASCO C2 FOV around 05:08 UT. The close spatial correspondence indicates that projection effects on the location of the type II burst and the CME LE (as inferred from *SOHO*-LASCO C2 observations) can also be assumed to be minimal. The type II burst seems to be spatially associated with the nose of the frontal structure of the CME.

Figure 3.6 shows the time profile of the Stokes I and V radio emission from the

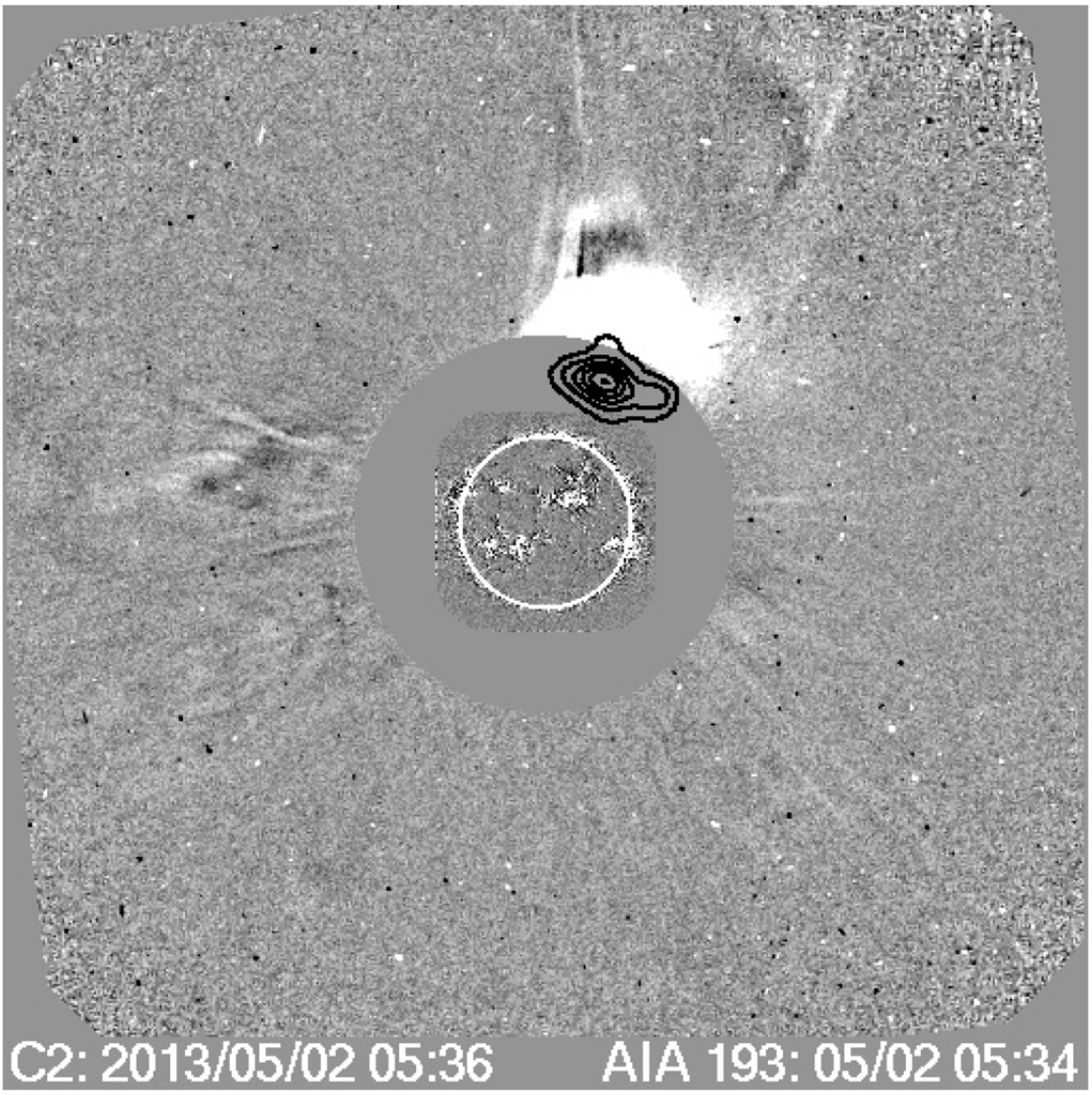

Figure 3.4: Composite of the 80 MHz GRAPH radioheliogram of the type II burst (05:08 UT) in Figure 3.1, SDO-AIA 193 $\mathring{A}$ image (05:34 UT), and SOHO-LASCO C2 image (05:36 UT) obtained on 2013 May 2. The peak T_b of the radioheliogram is 3.7 $\pm$ 0.3 $\times$ 10^9 K and the contours are in interval of 10% of the peak T_b . The white circle (radius = $1R_\odot$) at the center indicates the solar limb. The larger, concentric gray circle (radius $2.2R_\odot$) represents the occulting disk of the SOHO-LASCO C2 coronagraph. Solar north is straight up and solar east is to the left in the image. The enhanced emission above the northwest quadrant of the coronagraph occulting disk corresponds to the white light CME discussed in the text.

solar corona at 80 MHz as observed with the GRIP on 2013 May 2 during the interval 05:06−05:18 UT. A comparison of Figures 1 and 6 indicate that the enhanced Stokes I and V emission at 80 MHz corresponds to the H component of the type II burst

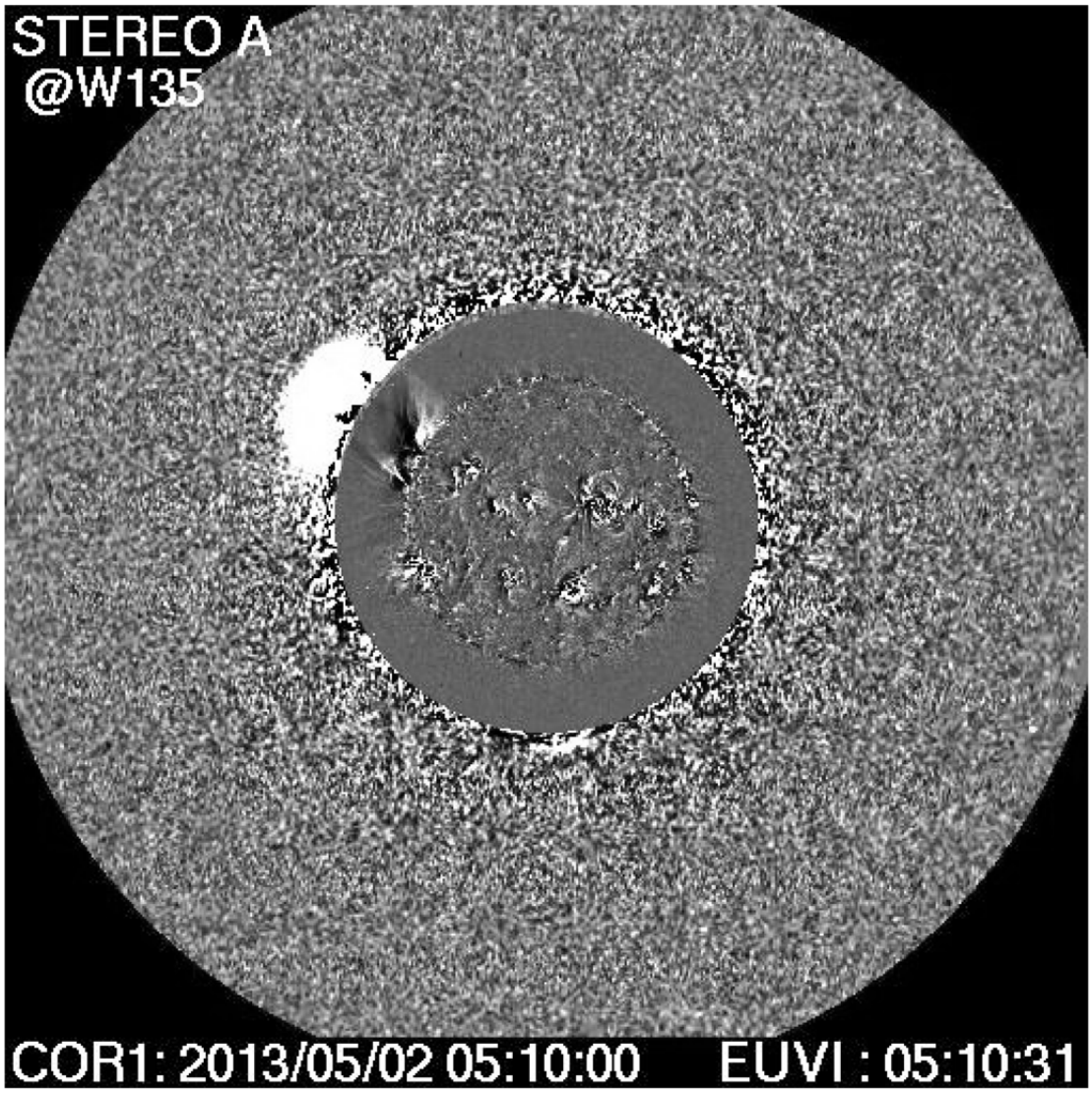

Figure 3.5: Composite of the STEREO A-COR1 and the STEREO A-EUVI 195 $\mathring{A}$ images obtained on 2013 May 2 at 05:10 UT. The gray circle (radius = $1.4R_{\odot}$) represents the occulting disk of the COR1 coronagraph. The enhanced emission to the left of the coronagraph occulting disk corresponds to the white light CME discussed in the text.

similar to the GRAPH observations of the type II burst in Figure 3.4. The GRIP observations during the interval 05:06−05:08 UT and 05:09−05:17 UT relate to the H_L and H_U bands, respectively, in Figure 3.1. The slightly longer duration of the event at 80 MHz in Figure 3.6, particularly the H_L band, as compared to Figure 3.1 is likely due to the better sensitivity of the GRIP over GLOSS. The Stokes V flux density of the H_U band in Figure 3.6 is larger by a factor of approximately 2 compared

to that of the H_L band. This is likely due to the presence of the herringbones in the F_U band (see Figure 3.2). It is possible that there is enhanced polarization at the type II burst location when the emission is from the corresponding harmonic, i.e., the H_U band (Suzuki, Stewart and Magun, 1980).

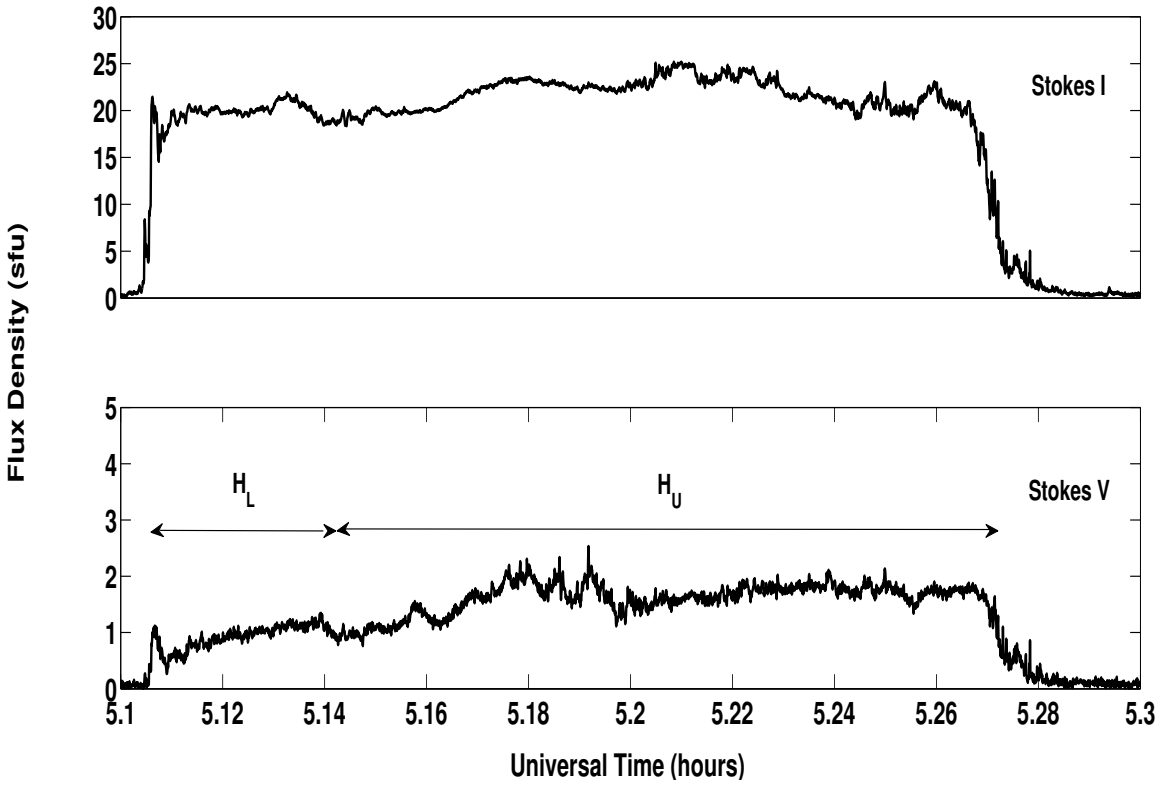

Figure 3.6: GRIP observations at 80 MHz on 2013 May 2 during the period 05:06−05:18 UT. The upper and lower panels correspond to the Stokes I and V, respectively. There is noticeable circularly polarized emission during the corresponding 80 MHz type II burst period in Figure 3.1.

The peak Stokes I and V flux densities in Figure 3.6 are 22 sfu and 1 sfu for the H_L band, and 28 sfu and 3 sfu for the H_U band. The corresponding dcp (= |Vflux|/Iflux, in the present case) for the HL and the HU bands are 0.05±0.02 and 0.1±0.01, respectively. Note that the type II bursts without the herringbone structures (i.e., the bursts with only the backbone present) and the H component of type II bursts with herringbone structures are both weakly polarized with dcp 0.2 (Suzuki, Stewart and Magun 1980; Stewart and Magun 1980;Cairns and Robinson 1987). Therefore, it is possible that the Stokes V emission in Figure 3.6 could be due to either one or both of them.

3.2.2 Analysis

3.2.2.1 Estimation of the speed of the CME and MHD Shock

From an inspection of the STEREO/A−COR 1 and STEREO/A−EUVI 195 $\mathring{A}$ composite movie close to the onset phase of the above CME, we inferred that its LE was at 1.6 $R_\odot$ around 05:05 UT. Note that CMEs in extreme ultraviolet (EUV) images often appear similar to their white light counterparts (Dere *et. al.* 1997;Gopalswamy *et al.* 2012). In the STEREO A-COR1 image obtained around 05:10 UT, the CME LE was at 2.1 $R_\odot$ (Figure 3.5). The above heighttime measurements indicate a linear speed of approximately 1160 kms^1 for the CME. Note that the latter was nearly a limb event for the above two instruments as mentioned in Section 3.2.1. The close agreement between the above mentioned location of the CME LE at 05:10 UT and the type II burst in Figure 3.4 at 05:08 UT reinforces the close spatio-temporal association between the CMEs and the metric type II bursts mentioned in Section 3.1. Also it indicates that any projection effects on the location of the type II burst in the present case is minimal. The onset of the type II event in Figure 3.1 was around 05:06 UT at a frequency of 60 MHz (F emission). Estimation based on the above speed of the CME indicates that its LE at 05:06 UT was likely to be around 1.7 $R_\odot$. This is in agreement with the typical CME height at the onset time of the metric type II bursts (Gopalswamy *et al.*, 2013). Constraining the electron density model of the solar corona based on the above height-time measurements, i.e., the 60 MHz plasma level should be located at a distance of 1.7 $R_\odot$, we find that five the Baumbach−Allen model (Baumbach 1937; Allen 1947) is the appropriate choice for the present case. For the 40 MHz plasma level, the corresponding radial distance is 2.0 $R_\odot$. The location of the centroid of the type II burst at 80 MHz (H emission) in Figure 3.4 is consistent with this. Having identified the appropriate coronal electron density model, we calculated the shock speed from the onset time difference between the occurrence of the type II burst at the same frequency in the F and H bands (see Figure 3.1) and their corresponding radial distances. The value is approximately 1320 kms^1. This is consistent with the CME speed estimated from the STEREO/A-COR1 observations.

3.2.2.2 Estimation of Coronal Magnetic Field

Using Polarization Measurements : Langmuir waves scattered-off of ions or low-frequency turbulence result in radiation at the fundamental of the local plasma frequency. Two Langmuir waves can also coalesce to produce electromagnetic waves

at twice the local plasma frequency, commonly known as second harmonic emission. Melrose, Dulk and Smerd (1978), Melrose, Dulk and Gary (1980),Zlotnik (1981) and Willes and Melrose (1996) had shown that when the Langmuir waves are collimated in the direction of the magnetic field, weakly polarized H radiation results with the sense of the O mode, and the magnetic field strength (B) near the source region of a solar radio burst (H component) is related to the observed DCP as,

$$B = 0.18 \frac{\mathrm{DCP}}{a(\theta)} f, \tag{3.1}$$

where f_p is the plasma frequency (fundamental component) in MHz and B is in G. $a(\theta)$ is a slowly varying function of the angle θ between the magnetic field and the viewing direction. We adopted equation 3.1 in the present case to estimate B since the observed circular polarization at 80 MHz in Figure 3.6 corresponds to the H component of the type II burst in Figure 3.1 and is also weakly polarized (DCP$\lesssim$0.1). The sense of polarization was assumed to be the O-mode because of the following reasons. (1) Both the type II and type III radio bursts are due to plasma emission and their polarization is predominantly in the O-mode for the F and H components (Melrose, 1980); (2) the X-mode emission experiences greater absorption than the O-mode during propagation through the solar corona (Fomichev and Chertok 1968; Thejappa, Zlobec and MacDowall 2003); and (3) the polarization characteristics of the FH type II bursts with herringbone structures are similar to that of the FH type III bursts. In the case of the latter, both the F and H components are polarized in the O-mode (Stewart 1966; Suzuki, Stewart and Magun 1980; Dulk and Suzuki 1980).

Since we are discussing the H component, f_p = 40 MHz in Equation (1). The peak DCP of the type II burst in figure 3.6 for the H_L and H_U bands are 0.05$\pm$0.02 and 0.1$\pm$0.01, respectively (see Section 3.2.1). We assumed $a(\theta) = 1$ since the burst in figure 3.4 is close to the solar limb (Dulk and McLean, 1978). Substituting the different values in equation 3.1, we get B $\approx$ 0.7$\pm$0.2 G and 1.4$\pm$0.1 G for the H_L and H_U bands, respectively. Considering that Langmuir waves can be present up to an angle of 30° to the magnetic field lines for weakly polarized second harmonic plasma emission in the O-mode (Melrose, Dulk and Smerd, 1978), we find that $a(\theta) \approx$ 0.5$-$1 (Melrose, Dulk and Gary, 1980). The above arguments indicate that B $\approx$ (0.7$-$1.4)$\pm$0.2 G and (1.4$-$2.8)$\pm$0.1 G for the HL and HU bands, respectively, and the ratio of the field strengths in the coronal region ahead of and behind the MHD shock front is $\approx$ 1:2.

Using split-band measurement : We also confirmed the above B value for the H_L band (i.e., emission from the coronal region ahead of the MHD shock front) using the often used technique to estimate the magnetic field in the upstream corona ahead of a CME from the split-band structure (Cho *et al.*, 2007; Smerd, Sheridan and Stewart, 1975; Vasanth *et al.*, 2014; Vršnak *et al.*, 2002) of the associated type II bursts as described below .

Plasma frequency (f_p) is related to the number density of electrons (Ne) as :

$$f_p \approx 9000\sqrt{N_e} \tag{3.2}$$

Using equation 3.2, one can obtain the number density of electrons corresponding to the upstream (n_1) and downstream (n_2) reagions of the shock front from the dynamic spectrum of the Type-II radio burst. The relative instantaneous bandwidth (BDW) of the splitting is then expressed as:

$$BDW = \frac{\triangle f}{f} = \frac{(f_2 - f_1)}{f_1} = \sqrt{(n_2/n_1)} - 1 \tag{3.3}$$

$$X = n_2/n_1 = (BDW + 1)^2 \tag{3.4}$$

$$M_A = \sqrt{(X(X+5)/2(4-X))} \tag{3.5}$$

$$V_a = V_s/M_A \tag{3.6}$$

$$B = 5.1 \times 10^{-5} \times f_l V_a \tag{3.7}$$

The density jump (X) across the shock front is then calculated from the upstream and downstream electron densities using equation 3.4 which is then used to derive the Alfv̆en Mach number (M_A) using the simplified Rankine-Hugoniot jump relation (equation 3.5) for perpendicular shocks in plasma environments with $\beta \ll 1$ and $\gamma = 5/3$ (Vršnak *et al.*, 2002). The shock speed (V_s) is then estimated from the electron density corresponding to the mid-frequencies of the F_U and the F_L bands of the band-split type-II burst (see Figure 3.3) and the coronal electron density model. Using the shock speed and the Alfv̆en Mach number one can estimate the Alfv̆en speed (V_a) using equation 3.6. The strength of the ambient magnetic field (B) is then obtained using V_a and the frequency (f_l) of the F_L band using equation 3.7.)

Assuming five × BaumbachAllen coronal electron density model for the type II burst in Figure 3.1 (section 3.2.2.1) and using the method of split-band analysis described above, we find that B ≈ 1.6 G at r = 2 $R_\odot$, the location of the type II burst in Figure 3.4. There is a reasonable agreement between the B values estimated using the two different methods. This strengthens the case of estimation of the coronal magnetic field strength from circular polarization observations of solar radio bursts, particularly when the latter is due to harmonic plasma emission. We also calculated the Alfvén speed (v_A) at r = 2$R_\odot$, i.e., at the location of the type II burst in Figure 3.4 using the relationship $v_A = B/\sqrt{4\pi M N_e}$, and the value is 628 kms^1 for the post-shock corona (behind the MHD shock front) and 314 kms^1 for the pre-shock corona (ahead of the MHD shock front). Here M = 2×10^{24}g is the mass ascribed to each electron in the coronal plasma (includes 10% He). We assumed Ne = 1.98 × 10^7 cm^3 , the electron density corresponding to 40 MHz, since the observed type II burst at 80 MHz is the H component.

Discussion We would like to note here that in the case of interplanetary type II bursts, the emission is mainly found in the upstream region of interplanetary shock waves driven by the CMEs (Reiner *et al.* 1998; Bale *et al.* 2009; Hoang *et al.* 2007). In-situ measurements indicate that the electron plasma waves required for the type II burst emission are also mainly generated in the upstream region of interplanetary shocks (Lengyel *et al.* 1997; Bale *et al.* 2009;Thejappa and MacDowall 2000; Pulupa and Bale 2008). Moreover, energetic electrons accelerated at the shocks should be preferentially reflected to the upstream region according to the theories (Cairns *et al.*, 2003). However, physical conditions in the corona are different from those in the interplanetary medium. Figure 3.2 indicates the propagation of energetic electrons downward (toward the photosphere) from the coronal shock. Such spectral features are rare in the interplanetary type II bursts compared to the coronal type II bursts (Vršnak *et al.*, 2001). Considering the examples of geometries in which a type II burst with different features can result (Holman and Pesses, 1983), it is possible that the present observations (where the type II burst has backbone with band-splitting and herringbone structures) could be due to the propagation of a curved shock front (with minimally gradual curvature) in an environment where the upstream magnetic field is inclined to the coronal density gradient (a geometry intermediate to those shown in Figures 2(b) and 2(c) of Holman and Pesses 1983). This would imply that the energetic electrons though being in the upstream region, similar to the interplanetary type II bursts, could still propagate downward toward the photosphere. However, the

geometry of shock front and magnetic field lines could be more complicated than is usually considered in the models.

3.3 Multi-lane Type-II Burst : Event of 2014 February 20

Both statistical and specific case studies have been conducted extensively to examine the drivers of multi-lane type IIs. In a particular statistical study by Shanmugaraju *et al.* (2005), 38 multiple type II events from 1997 to 2003 were examined. It was reported that more than 90% of the events are associated with both flares and CMEs. In most of these events, the first lane of the type II bursts started within the flare impulsive phase, and a majority (22/38) of the second lane of the type II bursts started after the flare impulsive phase, and no events were associated with multiple flares or multiple CMEs. They concluded that both flares and CMEs (front and flank) could be sources of multiple type IIs. Similar results has been reported in literature (Robinson and Sheridan, 1982; Shanmugaraju *et al.*, 2003; Subramanian and Ebenezer, 2006), with the exact driver of multi-lane type II bursts unresolved as yet. Since CMEs and flares often occur coincidentally (e.g., Zucca *et al.*, 2014), it is in general difficult to resolve the origin of multi-lane type IIs with a statistical study.

In view of the above, careful and extensive case studies on individual multi-lane type II events are necessary. One such well known event was examined by Cho *et al.* 2011 using the twin STEREO (Solar TErrestrial Relations Observatory; Howard *et al.*, 2008) spacecraft data obtained on 31 December 2007. By comparing the shock dynamics of the type II burst and CME kinematics, they concluded that the first lane was from the CME nose, the second from the CME flank that interacted with a nearby streamer. The same event was re-examined by Feng *et al.* 2013 and they concluded that the type II lanes with a spectral bump feature were associated with CME interactions with nearby streamers

In the subsequent sections, we present the observations of two successive Type-II bursts within a time interval of $\lesssim 1$ min. Interestingly both the bursts exhibit F-H as well as split-band structure. Type-II doublets with the above combined characteristics have rarely been reported and an attempt has been to unambiguously identify the driver of the multi-lane type II burst from our analysis.

3.3.1 Observations

Figure 3.7 shows the dynamic spectrum of the Type-II doublet bursts recorded with the GLOSS on 20 February 2014 during the time interval ≈ 03:22 - 03:26 UT. The bursts were associated with an SF-class Hα flare and a C3.3 class soft X-ray flare from AR 11982 located at the heliographic co-ordinates S14E38[www.swpc.noaa.gov]. It can be seen from Figure 3.7 that both Type-II bursts show split-band as well as F–H structure. Also, the onset of the second Type-II burst (2) was before the end of the first Type-II burst (1). The temporal interval between the onset of the two bursts is ≈ one minute. The F components of the bursts are present in the frequency range $\approx 40 - 65$ MHz. The starting frequencies of the F_{L1} and F_{U1} bands are ≈ 52 MHz and ≈ 62 MHz, respectively, at ≈ 03:22 UT. They are last noticed at ≈ 44 MHz and ≈ 52 MHz at ≈ 03:24 UT. The starting frequencies of the F_{L2} and F_{U2} bands are ≈ 52 MHz and ≈ 61 MHz, respectively, at ≈ 03:23 UT. They are last apparent at ≈ 40 MHz and ≈ 46 MHz around ≈ 03:26 UT. The harmonic components (H_{L1} and H_{L2}) of the lower band (L) for both Type-II bursts can be noticed in the frequency range ≈ 80 - 85 MHz during the interval ≈ 03:23 - 03:26 UT. An inspection of the e-CALLISTO solar radio spectrometer Benz *et al.* (2009) observations at the GRO in the frequency range $\approx 45 - 440$ MHz on 20 February 2014 revealed that the above Type-II bursts were limited to frequencies $\lesssim$ 125 MHz.

Figure 3.8 shows the STEREO/B-COR1 difference image obtained at ≈ 03:36 UT on 20 February 2014. The intense patch of emission seen to the right of the coronagraph occulting disk corresponds to a CME (referred to as CME2 in the rest of this work). The leading edge (LE) of the latter is at $r \approx 2.1$ $R_\odot$. The height–time (h–t) measurements of the above CME2 are shown in Figure 3.9. Note that STEREO-B was behind the Earth at ≈ E160° during the above epoch. This indicates that AR 11982 (the location of the associated flare) corresponds to ≈ W122° from STEREO-B view[stereo-ssc.nascom.nasa.gov/cgi-bin/make_where_gif]. An inspection of the height–time (h–t) measurements of the CME2 in the STEREO/B-COR1 field of view (FOV) indicates that its LE was at $r \approx 1.7$ $R_\odot$ around ≈ 03:26 UT. The projected linear speed is ≈ 464 kms^{-1}. Note that the associated active region, AR 11982 at S14E38, was ≈ 32° behind the limb for STEREO-B. So the de-projected speed is ≈ 547 kms^{-1}. We would like to add here that the CME2 was also observed with the *SOHO*/LASCO-C2 coronagraph, but the first appearance in the FOV of the latter was around ≈ 04:00 UT. The LE was at a radial distance of $r \approx 2.5$ $R_\odot$ at that time (see Figure 3.9)[cdaw.gsfc.nasa.gov].

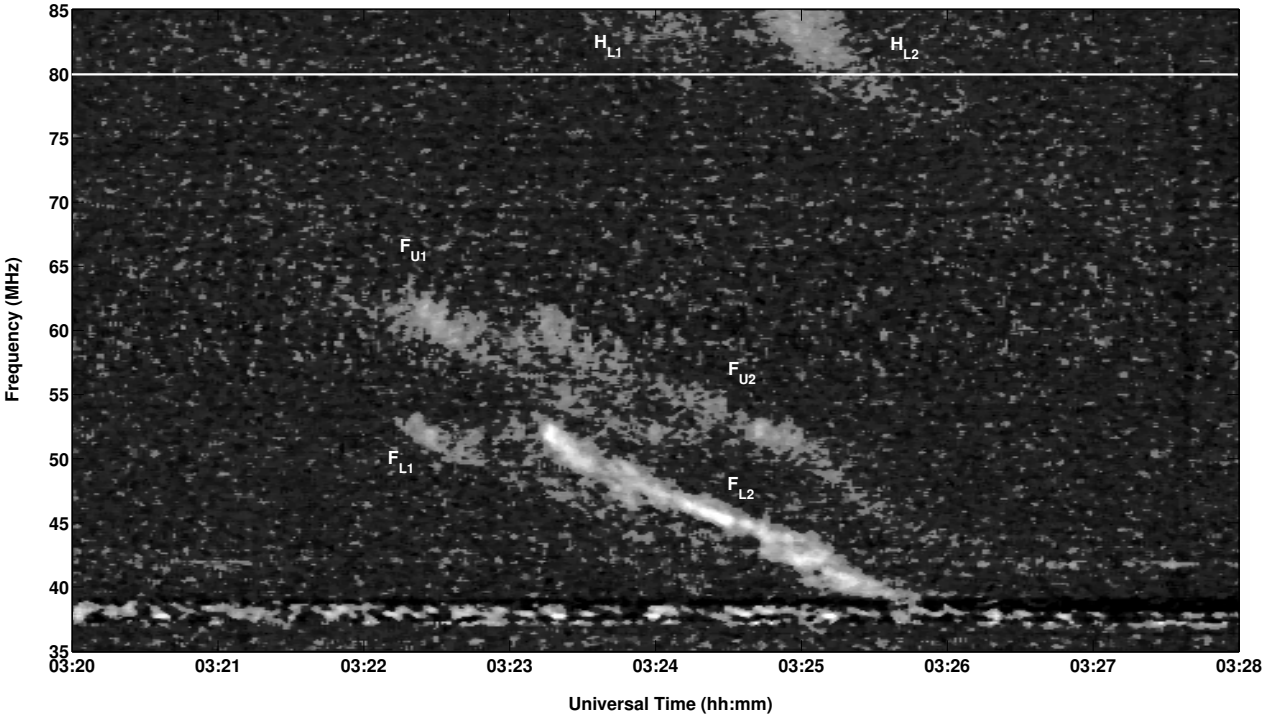

Figure 3.7: Dynamic spectrum of the Type-II burst doublet observed on 20 February 2014 during the interval ≈ 03:22 - 03:26 UT with the GLOSS. The horizontal white line indicates the 80 MHz observations in the spectrum. Numbers 1 and 2 in the suffixes of the labels F and H represent the first and the second Type-II burst, respectively.

Figure 3.10 shows the *SOHO*/LASCO-C2 observations on 20 February 2014 around ≈ 03:36 UT.The bright emission in the position angle (PA, measured counterclockwise from the Solar north) range PA ≈ 45° – 260° above the occulting disk corresponds to a 'halo' CME. This event will be referred to as CME1 in the rest of this work. S1 and S2 are pre-existing streamers. The lines A and B represent the Sunward extrapolation of the central PA of the white-light structures (S2 and part of CME1, respectively,) that are Co-spatial with them. The arc CME2 is the outline of the CME2 LE as observed in the STEREO/B-COR1 FOV in Figure 3.8. The first appearance of CME1 in the *SOHO*/LASCO-C2 FOV was around ≈ 03:12 UT. Note the above CME1 was observed in the STEREO-A COR1 FOV also. The first appearance was around ≈ 02:45 UT when the LE was at $r \approx 1.5$ $R_\odot$ (see Figure 3.9).

Figure 3.11 shows the temporal profiles of the Stokes-I and Stokes-V radio emission from the solar corona at 80 MHz as observed with GRIP on 20 February 2014 during

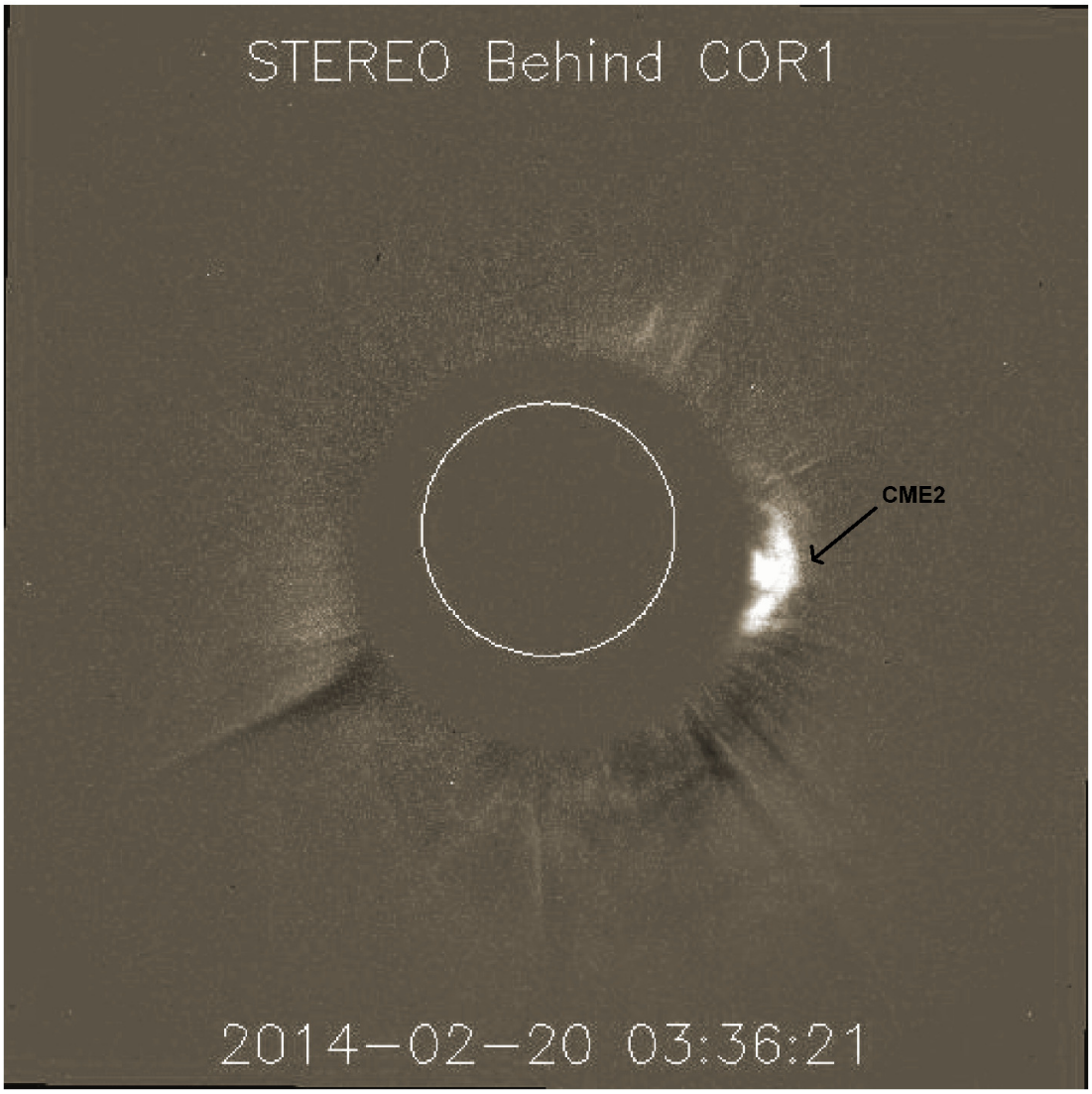

Figure 3.8: STEREO/B-COR1 difference image obtained on 20 February 2014 at ≈ 03:36 UT. The inner white circle (radius = 1 $R_\odot$) and the outer grey circle (radius ≈ 1.4 $R_\odot$) represent the solar limb and the occulting disk of the COR1 coronagraph, respectively. See Section 3.3.1 for the description of the label CME2.

the interval ≈ 03:23 - 03:27 UT. A comparison of Figures 3.7 and 3.11 indicate that the enhanced Stokes-I and Stokes-V emission at 80 MHz during the interval ≈ 03:24 - 03:25 UT and ≈ 03:25 - 03:26 UT correspond to the H_{L1} and H_{L2} bands, respectively, in Figure 3.7. The enhanced contrast of the bursts in the GRIP observations over the GLOSS observations is due to the comparatively better sensitivity of the latter. The peak Stokes-I and V flux densities in Figure 3.11 are ≈ 1.2±0.02 sfu and ≈ 0.12±0.02 sfu for the H_{L1} band and ≈ 2.33 ± 0.02 sfu and ≈ 0.15 ± 0.02 sfu for the H_{L2} band.

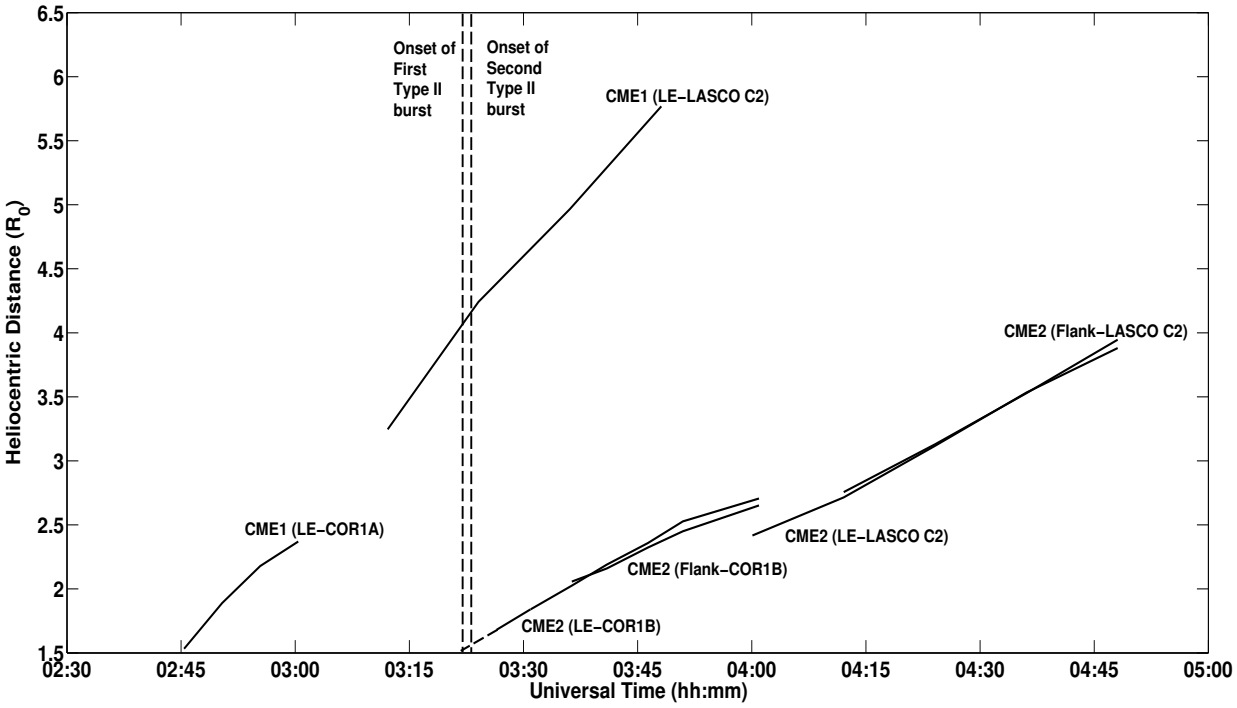

Figure 3.9: Height–time plots of the CMEs mentioned in the text. Labels COR1A and COR1B refer to STEREO-A COR1 and STEREO/B-COR1 coronagraphs, respectively.

The corresponding degree of circular polarization (dcp) are $\approx 0.1 \pm 0.02$ (H_{L1}) and $\approx 0.06 \pm 0.01$ (H_{L2}).

3.3.2 Analysis and Results

3.3.2.1 Estimation of the speeds of CME and Shock

The onset of the F_{L1} band in Figure 3.7 is $\approx$ 03:22 UT at a frequency of $\approx$ 52 MHz. Estimation based on the h–t measurements of the CME2 in the STEREO/B-COR1 FOV indicates that its LE should have been around $r \approx 1.5$ $R_\odot$ at $\approx$ 03:22 UT (see Figure 3.9). This is consistent with the mean radial distance of the CMEs at the onset of the metric Type-II bursts (Robinson, Stewart and Cane, 1984; Gopalswamy *et al.*, 2005; 2013). Since, i) close spatio-temporal association between the CMEs and the metric Type-II bursts has been widely reported (Stewart *et al.*, 1974a; 1974b; Gopalswamy and Kundu, 1992; Mancuso and Raymond, 2004; Cliver *et al.*, 2004; Lin, Mancuso and Vourlidas, 2006; Cho *et al.*, 2008; 2013; Liu *et al.*, 2009; Gopalswamy *et al.*, 2009; Ramesh *et al.*, 2010; 2012), ii) the lower and upper bands in a split-band

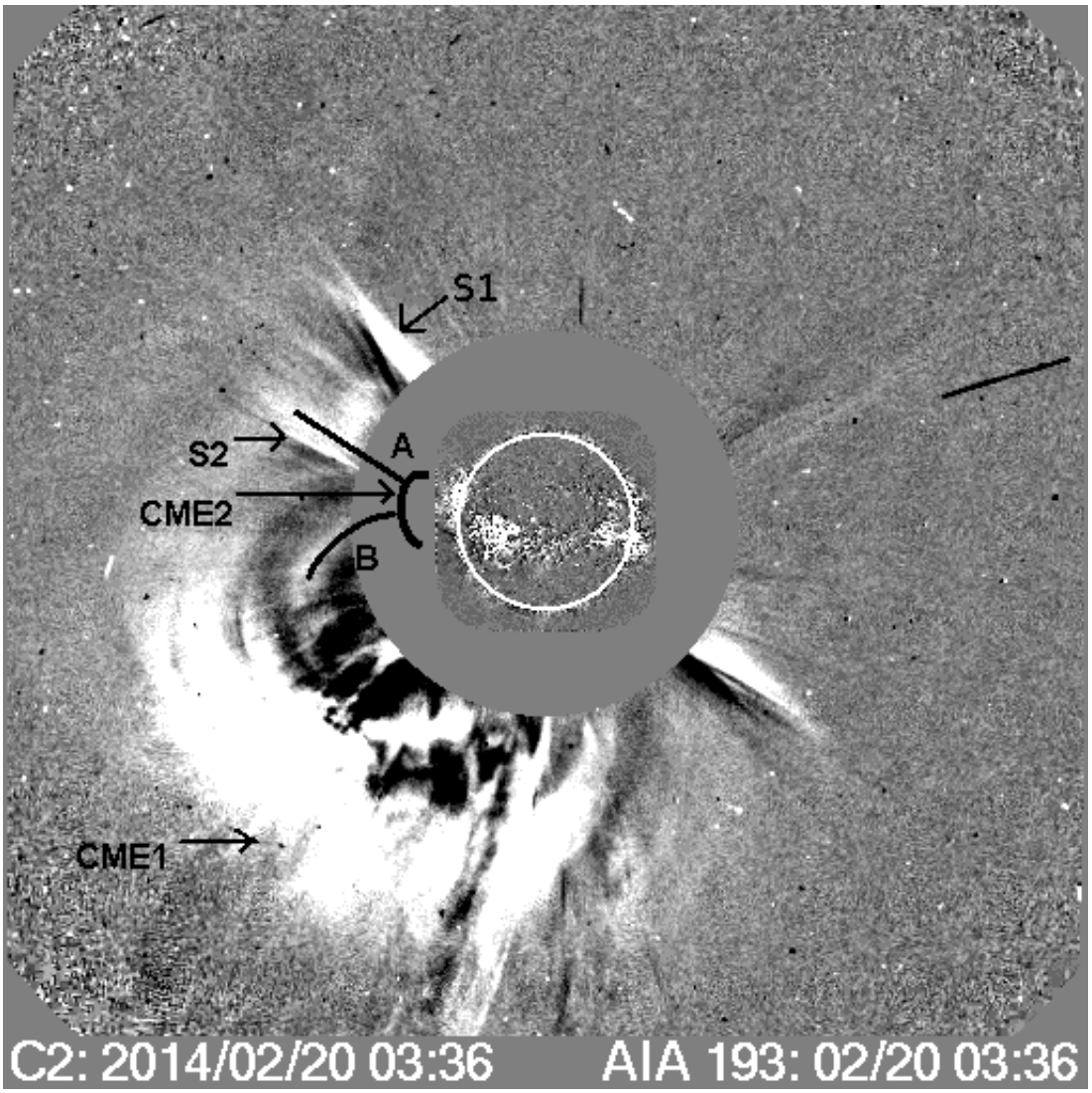

Figure 3.10: *SOHO*/LASCO-C2 white light + SDO AIA 193 Å difference image obtained on 20 February 2014 at ≈ 03:36 UT, same time as the STEREO/B-COR1 image in Figure 3.8. The inner white circle (radius = 1 $R_\odot$) and the outermost grey circle (radius ≈ 2.2 $R_\odot$) indicate the solar limb and the occulting disk of the LASCO C2 coronagraph, respectively. Solar North is straight up and East is to the left. See Section 3.3.1 for the description of the labels A, B, CME1, CME2, S1, and S2.

Type-II burst are considered to be due to emission generated in the corona ahead of and behind the MHD shock front associated with a CME (Vršnak *et al.*, 2001; 2001; Cho *et al.*, 2007; Hariharan *et al.*, 2014), iii) statistical studies indicate metric Type-II bursts with starting frequencies < 100 MHz are primarily due to MHD shocks driven by the CMEs Vasanth *et al.* (2011), we constrained the electron density model of the solar corona based on the h–t measurements of the CME2 in the STEREO/B-COR1

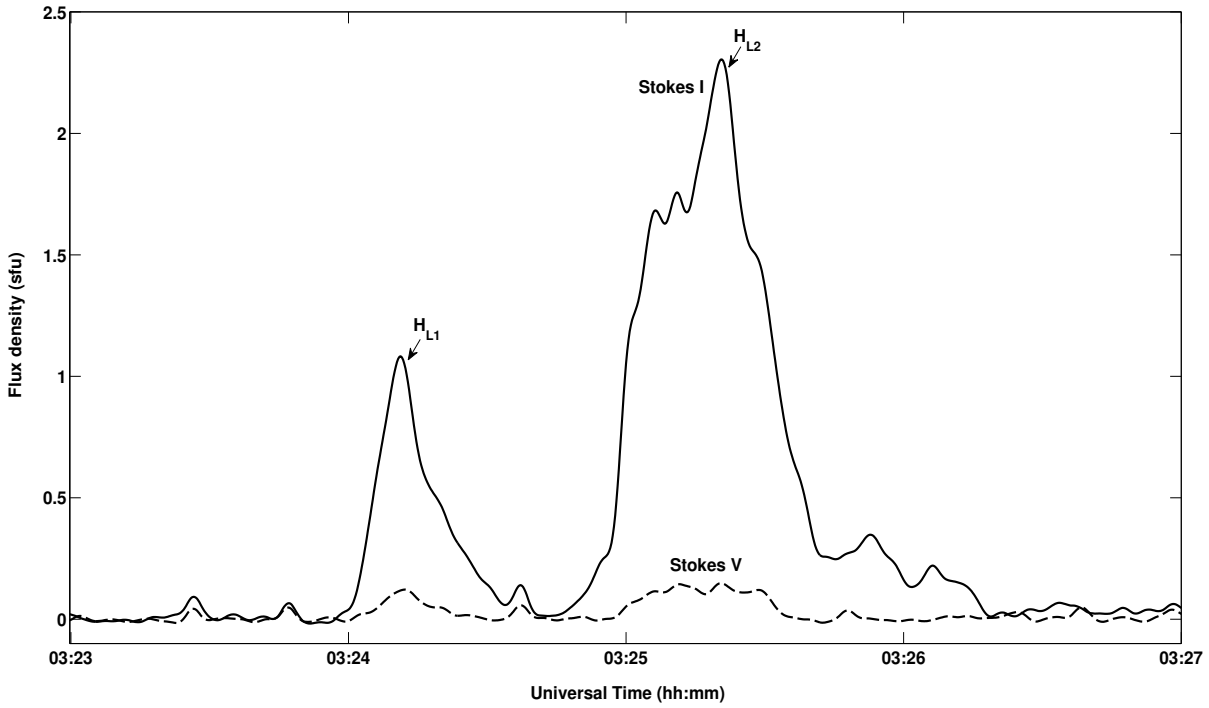

Figure 3.11: Time profiles of the Stokes-I (solid curve) and Stokes-V (dotted curve) emission observed with the GRIP on 20 February 2014 at 80 MHz around the same time as the Type-II burst in Figure 3.7.

FOV (see Figure 3.9), i.e. the 52 MHz plasma level should be located at a distance of $r \approx 1.5$ $R_\odot$, and found that 2 × Baumbach–Allen model Allen (1947); Baumbach (1937) is the appropriate choice. Having identified the coronal electron density model, we calculated the shock speed for the F component of first Type-II burst in Figure 3.7 and the value is ≈ 648 kms^{-1}. The onset of the second Type-II burst was at $\approx$ 03:23 UT at a frequency of ≈ 52 MHz, same as the first Type-II burst. The estimated shock speed for the F component in this case is ≈ 610 kms^{-1}.

3.3.2.2 Estimating the Magnetic Field Strength

The methodology of magnetic field estimation from the dynamic spectrum of split-band type-II burst, described in section 3.2.2.2, was applied to the present observations and it was found that $B \approx 1.3 - 1.1$ G over the frequency range $\approx 52 - 44$ MHz ($r \approx 1.49 - 1.58$ $R_\odot$) for the F_{L1} band, and $\approx 1.3 - 1.0$ G over the frequency range $\approx 52 - 40$ MHz ($r \approx 1.49 - 1.64$ $R_\odot$) for the F_{L2} band. The above values are reasonably consistent with the coronal magnetic-field strengths in the similar distance range

reported from observations of different types of solar radio bursts at low frequencies (Dulk and McLean, 1978; Gopalswamy *et al.*, 1986; Vršnak *et al.*, 2002; Mancuso *et al.*, 2003; Ramesh, Kathiravan and Sastry, 2003; Cho *et al.*, 2007; Ramesh *et al.*, 2011; Gopalswamy *et al.*, 2012; Ramesh *et al.*, 2013; 2013; SasikumarRaja *et al.*, 2014; Hariharan *et al.*, 2014). Interestingly, the B values obtained particularly using the Type-II bursts are extremely close (see Figure 3.12). Note that all the above estimates correspond to the "middle" corona ($1.2\ R_{\odot} \lesssim r \lesssim 3\ R_{\odot}$) where direct measurements of the field strength are presently difficult.

The low values of the peak *dcp* of the 80 MHz emission in Figure 3.11 and the close correspondence with the H_{L1} and H_{L2} components in Figure 3.7 indicate that Equation (3.1) can be used to estimate the coronal magnetic-field strength near the source region of the Type-II burst in the present case. The sense of polarization was assumed to be the "O" mode due to the same arguments presented in section 3.2.2.2. Substituting the peak dcp values estimated from the GRIP observations (see section 3.3.1) and $B \approx 1.0$ G (value corresponding to 40 MHz as estimated from the split-band observations in Figure 3.7) in Equation (3.1), we found that $a(\theta) \approx 1.4$ and ≈ 0.8 for the first and the second Type-II bursts, respectively. Considering that the Langmuir waves are confined within a cone of limiting angle $\approx 30^{\circ}$ for the second harmonic emission with "O" mode polarization, we find that the corresponding viewing angles (θ) are $\approx 72^{\circ}$ and $\approx 82^{\circ}$ Melrose, Dulk and Smerd (1978); Suzuki and Dulk (1985) for the first and the second Type-II burst, respectively.

3.3.3 Discussions

From the observations reported in the previous section we are able to draw conclusions to the driver of the type-II doublet as follows:
i) *two successive flares* - this possibility can be ruled out in the present case since two successive flares were not reported[1] during the Type-II burst period in Figure 3.7;
ii) *flare and a CME* - this scenario is less likely in the present case due to the following reasons: a) it has been established statistically that the speed of the first Type-II is greater than that of the second Type-II burst by a factor of ≈ 2 in the flare-CME scenario Shanmugaraju *et al.* (2005); Subramanian and Ebenezer (2006). The speeds of both Type-II bursts in Figure 3.7 are nearly the same; b) the time interval between the onset of the first and the second Type-II bursts is in the range $\approx 5 - 15$ minutes in the case of the flare–CME scenario Shanmugaraju *et al.* (2005); Subramanian and

[1]http://www.lmsal.com/solarsoft/latest_events

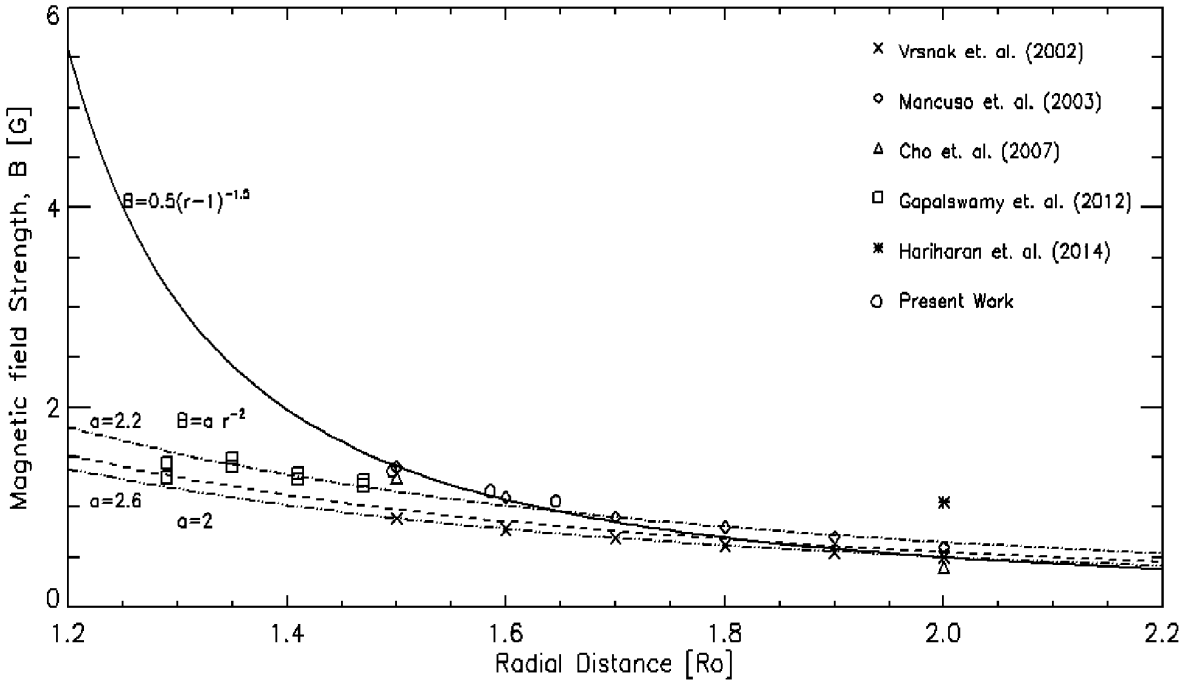

Figure 3.12: Estimates of the coronal magnetic-field strengths using Type-II radio bursts. The solid line profile represents the values obtained using the empirical relationship of Dulk and McLean (1978).

Ebenezer (2006). Compared to this the time interval is ≈ 1 min in Figure 3.7; c) it has been suggested that the Type-II bursts occur following the peak of the associated flare in the flare–CME scenario Claβen and Aurass (2002); Shanmugaraju *et al.* (2003). The onset as well as the end of the Type-II doublet bursts in the present case was before the peak of associated flare, i.e. during the onset-peak phase;

iii) *two successive CMEs* - here we are looking at the possibility that the first and the second Type-II bursts in the present case might have been due to MHD shocks driven successively by the LE of CME1 and CME2. An inspection of the h–t plot of the CME1 in Figure 3.9 indicates that the LE of CME1 was at $\gtrsim$ 4 $R_\odot$ at the onset time of the two Type-II bursts. However statistical studies indicate that the distribution of the CME heights at the onset time of the metric Type-II bursts is in the range $r \approx 1.2 - 1.9$ $R_\odot$ (Robinson, Stewart and Cane, 1984; Gopalswamy *et al.*, 2005; 2013). Therefore neither of the two Type-II bursts in the present case can be associated with the LE of CME1;

iv) *different regions of the same CME* - the angular width of the CME2 in Figure

3.8 is $\approx 80^{\circ}$. We calculated the speed of its flank, i.e. by tracking a feature located at angle of $\approx 40^{\circ}$ from the LE/nose. The projected and the de-projected speeds of the flank of CME2 are ≈ 433 kms^{-1} and ≈ 519 kms^{-1}, respectively. These are slightly smaller than the corresponding speeds of the CME2 LE, i.e. ≈ 464 kms^{-1} and ≈ 547 kms^{-1} (see Section 3.3.1). This is expected since the speed of the CME flank is generally less than that of the CME LE Cho *et al.* (2008); Gopalswamy *et al.* (2005). The estimated shock speeds of the first and the second Type-II bursts in Figure 3.7 are ≈ 648 kms^{-1} and ≈ 610 kms^{-1}, respectively (see Section 3.3.2.1). This close agreement between the two shock speeds suggests a common driver for the two Type-II bursts. Further, the difference between the shock speed of the first/second Type-II burst ($\approx 648/610$ kms^{-1}) and the de-projected speed of the LE/flank of the CME2 in Figure 3.8 ($\approx 547/519$ kms^{-1}) being $\lesssim 100$ kms^{-1} seems to indicate that the first and the second Type-II bursts in Figure 3.7 could probably be due to MHD shocks driven near-simultaneously by the LE and the flank of the CME2, respectively (Holman and Pesses, 1983; Sheeley, Hakala and Wang, 2000; Vourlidas *et al.*, 2003; Gopalswamy *et al.*, 2005; Cho *et al.*, 2007; 2008; 2011).

However the estimated viewing angles between the line of sight and the magnetic-field direction in the source region of the first and the second Type-II bursts are close to each other (angular separation $\approx 10^{\circ}$) as compared to the angular separation ($\approx 40^{\circ}$) between the LE and the flank of the CME2. This implies that the bursts are possibly due to MHD shocks driven by comparatively two close by regions on the CME2 structure. The similarity in the magnetic-field strengths of the first and the second Type-II bursts strengthens the above argument. An inspection of Figure 3.10 indicates that there is a strong possibility that CME2 propagated through the region of the corona where structures A and B were located at $\approx$ 03:22/03:23 UT, the onset time of the first/second Type-II burst (see Section 3.3.2.1). The PA separation between the locations where A and B intersect CME2 in Figure 3.10 at $\approx$ 03:36 UT is $\approx 15^{\circ}$. The structures A and B appear to diverge with increasing radial distance. So the PA separation between them should have been $< 20^{\circ}$ at $\approx$ 03:22/03:23 UT when they were relatively close to the Sun. This is consistent with the angular separation between the viewing angles of the first and second Type-II burst mentioned above. Therefore the doublet Type-II burst in the present are most likely due to MHD shocks generated via the near-simultaneous interaction of two different regions of the CME2 with the preceding CME1 and the pre-existing streamer S2.

3.4 Summary

We have presented the observation and analysis of two variants of low-frequency solar type-II radio bursts that occurred on two different days using the new low-frequency spectrograph antenna system described in section 2.4. It can be clearly seen that the impulsive radio emission from the sun at low-frequencies tend to display complex morphologies both in time and frequency. Also it can be noticed that due to the limitations on the dynamic range and frequency resolution posed by the analog spectrum analyzer it was not possible to accommodate the RFI filled low-frequency band and extend the low-frequency coverage below 25 MHz. In order to effectively extend the low-frequency coverage for spectral observations and to better study the fine spectral/temporal structures with high dynamic range, we decided to upgrade the back-end receiver using commercially available digital hardware and configure a digital spectrograph.

Chapter 4

High-Dynamic Range Solar Spectrograph

4.1 Introduction

A conventional swept-frequency analog spectrum analyzer was used as the back-end receiver for the single antenna low-frequency spectrograph described in (refer chapter 2). In the case of a conventional analog spectrum analyzer, data is obtained only at a single frequency at any given time. The dwell period at each frequency depends on the ′sweep′ time between the start and end frequencies of the observing band, and the number of frequency channels in the instrument which is usually a preset parameter. The above ′sweep′ time also determines the time gap between the adjacent data samples at any given frequency which increases with larger bandwidth of observations and this poses serious limitations on the frequency resolution obtainable with these instruments. Due to the aforementioned reasons on limited spectral resolution and poor dynamic range offered by the spectrum analyzer, the low frequency coverage of the sectrogaph system had to be limited to 25 MHz (refer conclusion section of previous chapter).

Making use of the developments in the field of digital signal processing, several authors have shown that it is possible to obtain better dynamic spectra of the solar radio transients than those obtained with the conventional analog spectrum analyzer (Ebenezer *et al.*, 2001; Iwai *et al.*, 2012; Lecacheux *et al.*, 2004; Morosan *et al.*, 2014; Ryabov *et al.*, 2010; Taylor *et al.*, 2012). Availability of high speed digitizers that can sample analog signals over a large operating bandwidth ensures simultaneous spectral coverage over the observing band during each integration time. Also the very high sampling rates offered by the digitizers improves the temporal resolution in spectral data records. Improvement in temporal resolution could help us to study and

understand the fine structures in solar radio bursts.Higher spectral resolution can be used to localize the RFI in the frequency space which helps to mark the corresponding frequency channels and the observational data in such channels are flagged off without consideration for further processing (Baan *et al.*, 2004). On the other hand, such RFI dominated frequency channels could be identified and RFI excision algorithms could be implemented to such channels and retrieve the useful data for scientific analysis (Offringa, 2012) An increase in the number of digital bits that represent the input analog signal (i.e. the amplitude resolution) could lead to an enhancement in the dynamic range of the observations. This is very useful to detect weak energy release in the solar atmosphere (Mercier and Trottet, 1997; Oberoi *et al.*, 2011; Ramesh and Ebenezer, 2001; Ramesh *et al.*, 2010, 2013) which are thought to contribute to the coronal heating.

Having said so, the advantages with the digital signal processing have not been fully exploited particularly at low radio frequencies which offer unique diagnostics of the solar corona and the magnetic field there(see for eg. Bastain (2004); Reiner *et al.* (2007); Zaqarashvili *et al.* (2013)).

4.2 Instrument Description

A digital spectro-correlator was recently commissioned at the GRO for observations of transient solar radio emission in the frequency range ≈ 30 - 15 MHz using digital back-end receiver configured from commercially available high speed analog-to-digital converter (ADC) and Field Programmable Gate Array (FPGA) hardware.

4.2.1 Digital Back-end Receiver

A digitizer card procured from National Instruments (Model No. PCI-5105) is used as the digital back-end receiver. The card consists of :

4.2.1.1 Analog-to-Digital Converter (ADC)

A high-speed ADC that can sample a band-limited time series signal at a maximum sampling rate of 60 million Samples per second (MSPS). It is a 16-bit ADC built on flash converter architecture explained in Appendix B. At any instant the ADC can take eight analog signals as input channels with each channel having an instantaneous bandwidth not exceeding 30 MHz. The ADC is also supplied with a switchable anti-aliasing low-pass filter with a cut-off frequency at 65 MHz which limits the maximum frequency of the input analog signal. In principle, an analog signal bandwidth of

Table 4.1: Specifications of the digitizer card

Total number of analog i/p channels	8
Bit resolution	16
Sampling rate (maximum)	60 MHz
Bandwidth	30 MHz
Input voltage range (V_{pp})	0.05 - 30 V

up-to 30 MHz in the frequency range 0 - 60 MHz (which includes the second Nyquist zone) can be sampled by the ADC. The characteristics of the ADC card are provided in Table 4.1.

4.2.1.2 Field Programmable Gate Array (FPGA)

The Virtex-2 Pro FPGA chip is provided on the digitizer card for data handling purpose.An on-board data buffer is implemented as a FIFO (First-In-First-Out) on the FPGA chip. The FIFO has a maximum memory capacity of $\approx$ 128 MB (MegaBytes) which is shared equally by the analog input channels that are used. The card is interfaced to a computer through a standard Peripheral Component Interconnect (PCI) bus which supports a maximum data transfer rate of $\approx$ 132 MB/sec. The specifications of the above digitizer card (see Table 4.1) are nearly identical to that described in Ryabov *et al.* (2010). LabView user interface is provided for setting the control parameters of the digitizer card, and the data acquisition which involves file creating and writing operations. The data acquisition can be either in the continuous mode or in the burst mode. In either case, the on-board memory is filled with the data to a specified depth during the acquisition. The data are then retrieved and stored in the hard disk of the host computer. But due to the shared on-board memory and the limitations in the data transfer rate of the PCI bus, we found that there is $'$data overwrite$'$ in the case of continuous mode of operation. Hence the card is presently operated in the burst mode in which a fixed number of data samples (defined by the user) are written to the on-board memory. No new acquisition will take place till all the data are retrieved. This results in a time gap of $\approx$ 10 msec between successive data acquisitions. Note that the life-time of the solar radio transients is $>$ 1 sec at low frequencies (McLean and Labrum, 1985). So the above time gap should not affect the observations.

4.2.2 Two-Element Antenna Array

We have fabricated and tested another LPDA using the design specifications (LPDA;

Figure 4.1) described in refer antenna design section in chapter 2 to be used for the two-element spectrograph array. The two LPDAs have been mounted vertically with a spacing (d) $\approx$ 12 meters between them along a North-South (NS) baseline. This baseline orientation between the two LPDAs facilitates observations for a duration of more than 6 hours in a day without the need for steering their $'$beam$'$ along the hour angle. But there will be a path length difference ($= dsin\theta$, where θ is the zenith angle) between the RF signal incident on the two LPDAs depending on the declination (δ) of the radio source. This can be compensated either in the analog or in the digital signal path. In the analog case, a coaxial cable of appropriate length is introduced in the RF signal path from either of the two LPDAs depending on the declination of the source with respect to the local zenith. In the digital case, an instrumental time delay (τ_i) equal to the geometrical time delay ($\tau_g = \frac{dsin\theta}{c}$) is introduced in the appropriate signal path after the digitization and sampling of the RF signal. Note that the change in the above path length difference ($= dsin\theta$) is negligible over a $\approx \pm$ 3 hours observing period in a day, for a particular declination. Also the change in the declination of the Sun within one day is very minimal ($\approx 0.1^{\circ}$). So, the inclusion of a co-axial cable of specific length in the RF signal path will provide the required path length compensation with minimal error for about one month. Similar to the baseline between the two LPDAs, their $'$arms$'$ are also oriented in the North-South direction (Figure 4.1). The above separation between the LPDAs has been chosen to minimize the mutual coupling between them to $<$ -40 dB (see for eg. SasikumarRaja *et al.* (2013b)). The RF signal from each LPDA is passed through a high-pass filter with cut-off frequency (f_h) $\approx$ 15 MHz (Figure 4.2). The filtered signal is amplified ($\approx$ 30 dB) and transmitted to the receiver room via coaxial cable buried $\approx$ 1 meter beneath the ground (Section 2.4). A low pass filter with cut-off frequency (f_l) $\approx$ 30 MHz restricts the RF signal bandwidth to $\approx$ 30 - 15 MHz for sampling and digitization by the digital receiver.

4.3 Implementation of a Correlation Spectrograph

Radio spectral observations of the solar corona at low frequencies are usually carried out with a single antenna (Benz *et al.*, 2009). In order to minimize the contribution from the galactic background and improve the sensitivity, we have configured our spectrograph in the cross-correlation mode with inputs from two identical antennas. Note that the correlation mode of observations provides better sensitivity (Kraus, 1950). The RF signal output from the low-pass filters are connected to two of the

Figure 4.1: A view of the two LPDAs used in the spectrograph.

analog input channels of the digitizer card (Figure 4.2). The specifications of the spectrograph are given in Table 4.2. The analog signals are sampled at the Nyquist rate and quantized to 16-bit data which are then stored in the on-board memory of the card. The sampled time domain data from the two antennas are then converted to the spectral domain using Fast Fourier Transformation (FFT). The amplitude of each of the corresponding frequency components from the two antennas are correlated and integrated. Designating $C1, C2$ and $S1, S2$ as the cosine and sine components corresponding to the two antennas (see Figure 4.2) in the spectral domain, the in-phase (cosine) and quadrature (sine) correlations are estimated using the relations $X = (C1 \times C2) + (S1 \times S2)$ and $Y = (C2 \times S1) - (C1 \times S2)$, respectively (see for eg. Ramesh, Sundara Rajan and Shastry (2006)). The visibility amplitude is given by $\sqrt{X^2 + Y^2}$. The correlated/integrated visibility amplitudes are written to the computer hard disk in binary format for further processing. The observations are carried out everyday during the interval $\approx 3 - 11$ UT.

4.4 Observations

The spectrograph was commissioned in October 2013 and a trial observational run was carried out initially for a period of four months during the period October 2013

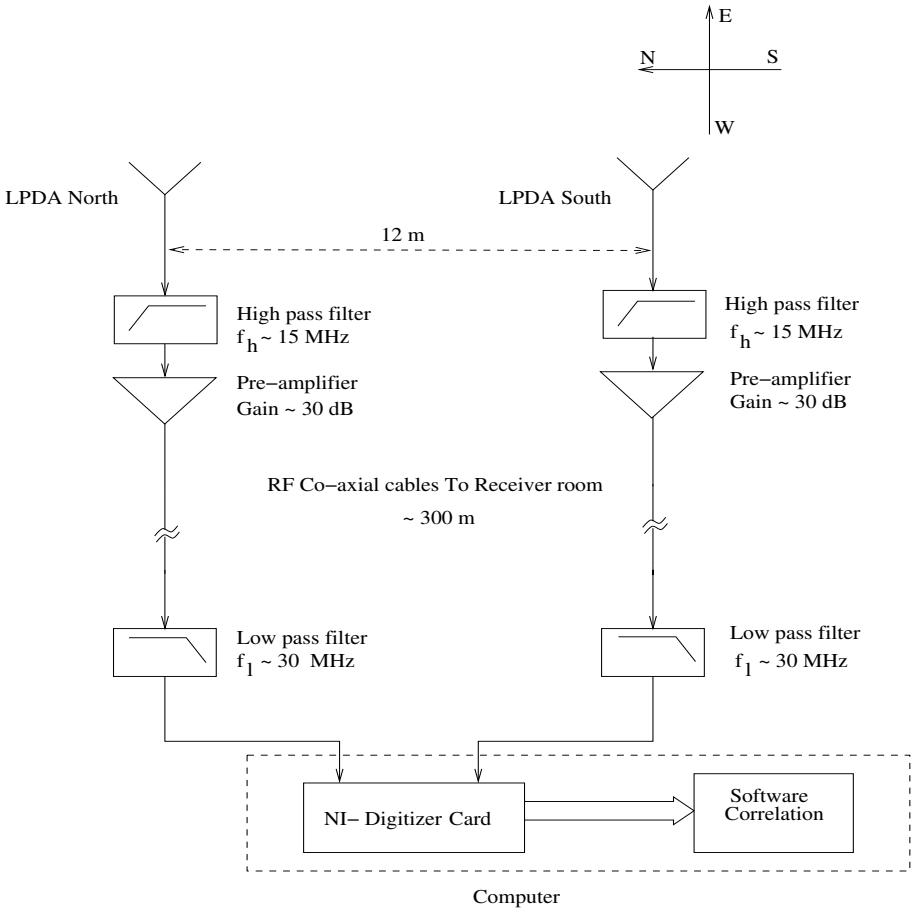

Figure 4.2: Block diagram of the spectrograph.

Table 4.2: Specifications of the spectrograph

Number of analog input channels	2
Frequency range	30 - 15 MHz
Number of frequency channels	4096
Sampling rate	60 MHz
Spectral resolution	7.32 kHz
Temporal resolution	69.6 μsec

- January 2014. A total of 71 solar radio bursts of type III were recorded from our daily observations during the above-mentioned period (see Table 4.4). An inspection of the dynamic spectra of the radio bursts observed with the RAD2 spectrograph on-board Wind-Waves during the corresponding period indicates that all the events listed in Table4.4 continued to frequencies < 15 MHz[1].

[1]http://lep694.gsfc.nasa.gov/waves/data_products.html

Prologue to Solar Type III Radio Bursts Solar radio bursts of Type III were first discovered using ground-based radio observations in the frequency range 10 to 500 MHz (Wild, Smerd and Weiss, 1963). They occur as fast-drift radio emission in the aforementioned frequency range with a drift rate of $\approx$ 10 MHz/s and can have a duration of few seconds. These are one of the most extensively observed and studied astrophysical phenomena. Type III radio emission is believed to be excited at the fundamental and second harmonic of the electron plasma frequency in a two-step process (Ginzburg and Zhelenzniakov, 1958; Wild and Smerd, 1972) wherein: i) the electrons accelerated in solar flares are energized to high energies of the order of few keV and stream away along open magnetic field lines inducing high-frequency plasma oscillations locally, all the way from the corona into the distant heliosphere; ii) These plasma oscillations (referred as "Langmuir waves") are converted to escaping electromagnetic radiation by non-linear wave-wave interactions. The beam-plasma system is unstable to the generation of Langmuir waves and these are scattered off of ions or low-frequency turbulence resulting in radiation at the fundamental of the local electron plasma frequency. Similarly the coalescence of two Langmuir waves can produce electromagnetic waves at twice the local electron plasma frequency, commonly known as "second harmonic emission". The above is referred as the $'$plasma emission mechanism$'$ which is the most accepted model for Type-III radio burst generation and has been verified through analytical calculations over many years in order to validate the observational properties such as the drift, brightness and harmonic structure of bursts, etc. There are many different variants of Type-III radio bursts based on their appearance in the waterfall diagram of the dynamic spectrum, as mentioned below:

Type-IIIg: Type-III bursts can occur either in isolation or in groups quasi-continuously which can last for a few minutes. The type-III groups (type-IIIg) are referred as $'$type-III storms$'$ when they continue to occur over a period of days. They are often observed to occur as harmonic emission with a low degree of polarization (Reid and Ratcliffe, 2014; SasikumarRaja and Ramesh, 2013) and each individual burst is thought to be a signature of individual electron streams associated with a common acceleration site.

Type-IIIb: These are bursts whose time duration is $\leq$1 second and display frequency splitting. They appear as a chain of elementary bursts as single, double or triple narrow-banded striations $\approx$ 100kHz in the dynamic spectra with a frequency drift similar to that of the type III radio burst. It has been found that atleast $\approx$ 30 % of these bursts are precursors to the type III bursts and they seem to have a common

exciter and hence the classification.

J and U bursts: The frequency drift of type-III bursts has been observed to change sign and appear to take the shape of an inverted U or J in the dynamic spectrum plots. These bursts are believed to be electron streams travelling along magnetic fields confined to the corona. For the $J-$bursts, the radio emission stops when the electron beam reverses direction but with $U-$bursts it continues to higher frequencies. due to their low occurrence rate their source properties are not yet fully understood.

Type-V: These are closely related to the type III burst and are classified by their relatively longer duration and wide spectra (Wild, Smerd and Weiss, 1963). They appear as a continuation to type-III burst in the dynamic spectra. Type V bursts appear at low frequencies below 120 MHz and generally have $1-3$ minute durations (Dulk and Suzuki, 1980). Type-V radio emission is thought to be due to the plasma emission from electron beams travelling along curved magnetic field lines which explains the relatively longer duration and continuum-like emission features.

Figure 4.3 (upper panel) shows the dynamic spectrum of a type III solar radio burst recorded with the instrument on 2014 December 14 during the time interval $\approx$ 06:24 - 06:27 UT. Observations of the same event obtained using the Wind-Waves RAD2 spectrograph is shown in the lower panel of Figure 4.3 for comparison. This clearly illustrates the excellent temporal correspondence and the near continuous spectral coverage offered by the two observations. This is important to understand the characteristics of the solar radio bursts which continue to frequencies < 15 MHz in the spectrum and those which do not (see for eg. the review article by Reid and Ratcliffe (2014)).

Through careful inspection we found that 12/71 bursts observed with our spectrograph were of comparatively longer duration, > 100 sec (see Table 4.4). Amongst the twelve long duration bursts, four bursts exhibited quasi-periodicity in their time profile at discrete frequencies. Table 4.3 lists the dominant periodicities for the four quasi-periodic bursts at a typical frequency (f) like 19.5 MHz (see Section 4.5 for details). Three of the quasi-periodic bursts occurred in the immediate aftermath of either a partial 'halo' or a 'halo' coronal mass ejection (CME)[2]. The fourth quasi-periodic burst (2014 January 31) was preceded by a 'halo' CME by $\approx$ 15 hours. The eight long duration bursts that did not show any quasi-periodicity were not associated with any 'halo' CMEs.

[2]cdaw.gsfc.nasa.gov

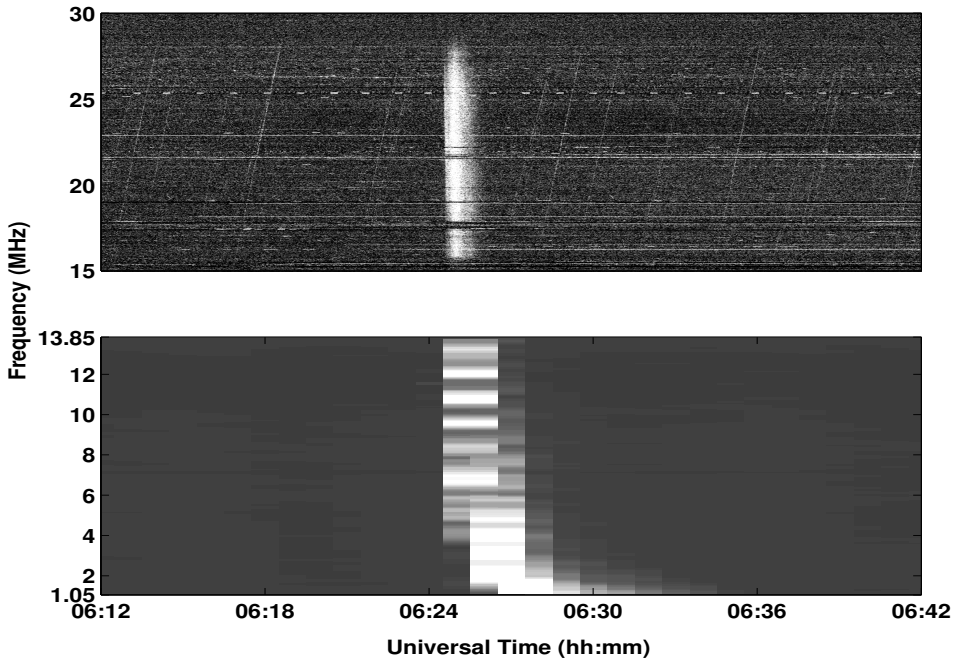

Figure 4.3: **Upper Panel:** Dynamic spectrum of a type III solar radio burst observed on 2013 December 14 during the interval ≈ 06:24 - 06:27 UT with the Gauribidanur low-frequency spectrograph in the cross-correlation mode. One can notice that the observations are minimally affected by RFI. **Lower Panel:** Wind-Waves RAD2 spectrograph observations of the same burst with spectral and temporal resolutions of ≈ 20 KHz and ≈ 60 sec, respectively. The advantages with higher temporal and spectral resolutions are clearly evident in the Gauribidanur observations.

Figure 4.4 shows the dynamic spectrum of the quasi-periodic bursts observed on 2013 October 28 during the time interval ≈ 04:36 − 04:42 UT. The fast drifting features are the characteristic signatures of group of type III solar radio bursts explained earlier.

Figure 4.5 shows the time profile (indicated by the solid line) of the group of type III radio bursts in Figure 4.4 at a typical observing frequency (f) like 19.5 MHz. Also shown is the time profile of the same event obtained in the total power mode with only one of the LPDAs in the spectrograph. The dynamic range is about a factor of five higher in the former. This is due to a combination of observations in the correlation mode and an increase in the collecting area (see for eg. Kraus (1950)). The estimation of the visibility amplitude using both the in-phase and quadrature correlations as in imaging observations with radio interferometric arrays, and the use of all the cosine and sine components (i.e. C1, C2, S1 and S2) to obtain the

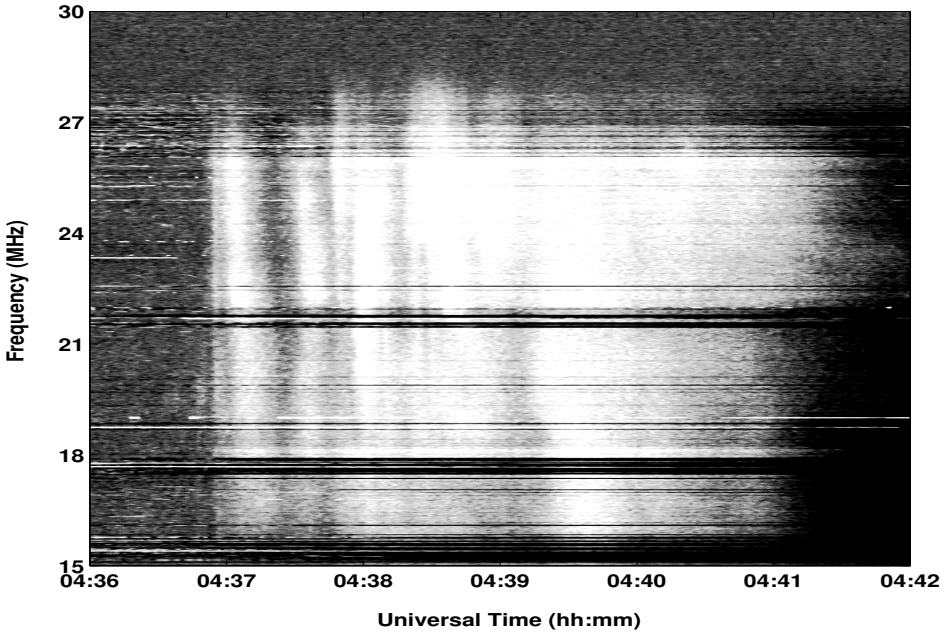

Figure 4.4: Dynamic spectrum of group of type III solar radio bursts observed on 28 October 2013 during the interval ≈ 04:36 - 04:42 UT. The dark patch towards the end of the observations is due to sudden ionospheric disturbance' (commonly referred to as 'short-wave fadeout') in the Earth's ionosphere.

in-phase and quadrature correlations (see Section 4.3) further enhances the dynamic range. The latter is particularly useful since the ′noise′ in above components are independent. These indicate that the dynamic spectrum of the radio signatures of the transient energy releases in the solar atmosphere can be obtained with better sensitivity through observations in the cross-correlation mode. Note that the presence of quasi-periodicity in the radio emission can be clearly noticed in the correlation mode.

4.5 Analysis

4.5.1 Multi-Resolution approach to periodicity analysis using wavelets

Any signal can be visualized in either time domain or frequency domain. The Fourier Transform (FT) is a generalization of the Fourier Series, which is a mathematical tool to decompose any periodic signal into as a trigonometric series of sines and cosines. Fourier Transform is a transformation tool that is useful in visualizing a continuous signal in the frequency domain by estimating the contribution of a given frequency to

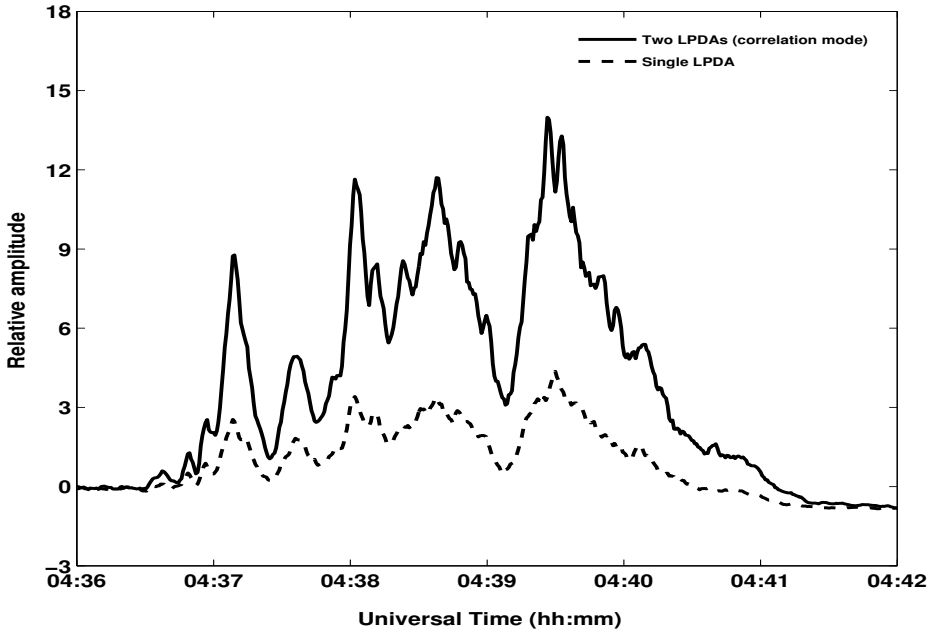

Figure 4.5: A comparison of the time profiles of the group of type III bursts (in Figure 4.4) as obtained with the two LPDAs (correlation mode) and a single LPDA (total power mode), at 19.5 MHz.

the particular signal. In reality we deal with discrete signals and equation (refer) is formulated in a different form and it is called the Discrete Fourier Transform (DFT). The Fast Fourier Transform (FFT) is an algorithm which follows the *divide and conquer* approach to accelerate the DFT process.

When analyzing signals of a non-stationary nature, it is often beneficial to be able to acquire a correlation between the time and frequency domains of a signal. The Fourier transform, provides information about the frequency domain, however time localized information is essentially lost in the process. The problem with this is the inability to associate features in the frequency domain with their location in time, as an alteration in the frequency spectrum will result in changes throughout the time domain. Therefore for temporal localization of individual spectral components in a signal, a multi-resolution analysis is considered to be a better approach which will give a time-frequency representation of the time domain signal. Two of the most commonly used multi-resolution analysis techniques are listed below,

Short-Time Fourier Transform (STFT) In STFT, the time domain signal is divided into multiple series defined by a common window function and the FFT algorithm is applied for the time series in each window. This is done to to try and

localize the frequency contribution in the given time domain signal. However, it can be noticed that the frequency resolution is decided by the length of the time window which is constant for all frequencies. This results in a reduction in bandwidth of each frequency bin and offers poor resolution in both temporal and spectral domain.

Wavelet Transform In view of the shortcomings of the STFT for a more accurate localization of spectral components in a time domain signal the Wavelet Transform (WT) is considered. In wavelet transform, the window function is chosen to be of variable lengths which allows the use of long time intervals where we want more precise low-frequency information, and shorter regions where we want high-frequency information. A wavelet is a wave-like oscillation with an amplitude that begins at zero, increases, and then decreases back to zero. The base mathematical function representing a wavelet in the wavelet transform is called a′mother wavelet′. The wavelet analysis uses a time-scale region and allows exceptional localization in both the time domain via translations of the mother wavelet, and in the scale (" response interval ") domain via dilation of the mother wavelet. The wavelet transform is the convolution of the time series with the scaled and translated version of the wavelet function giving us the wavelet power spectrum.

$$\psi_\eta = \pi^{-1/4} e^{i\omega_0 \eta} e^{-\eta^2/2} \tag{4.1}$$

In the present work the wavelet transform technique has been considered for the analysis quasi-periodicities in the TypeIIIg time profiles (Kaiser, 1994; Torrence and Compo, 1998; Zaqarashvili *et al.*, 2013). It was decided to use the morlet wavelet function (equation 4.1) as the base wavelet the present case which is primarily due to its mathematical simplicity. Though the choice is arbitrary it has been suggested (Kaiser, 1994; Torrence and Compo, 1998; Zaqarashvili *et al.*, 2013) that it can be used to model such periodic signals. Figure 4.6 shows the wavelet power spectrum obtained for the radio burst in Figure 4.5 (correlation mode) using equation 4.1. A wide range of periodicities can be seen in the spectrum. The duration of each one of them is shown in Figure 4.7. Considering only those periodicities within the 1/e width of the ′fit′ to the data points in Figure 4.7, we find that $p \approx 5 - 75$ sec. Note that the above 1/e region includes nearly all the periodicities outside the cone of influence (COI) boundary of the wavelet transform in Figure 4.6.

Table 4.3: Details of the quasi-periodic type III solar radio bursts

Date	Burst time (UT)	Burst duration (sec)	Burst periodicity p (sec)	Magnetic field B (G)	CME onset (UT)	CME width	CME speed (km/sec)
2013-10-28	04:36	288	5-75	0.96-0.06	04:07	156°	1200
2013-12-07	07:22	144	9-61	0.53-0.08	07:01	360°	1085
2014-01-26	10:09	144	4-28	1.00-0.18	07:53	255°	1088
2014-01-31	07:26	118	5-29	0.90-0.17	15:36[a]	360°	1087

[a]Previous day

4.5.2 Quasi-periodic pulsations and coronal magnetic field

The quasi-periodicity in the observed solar radio flux at low frequencies which are primarily from the upper part of the corona is due to the modulation of the electron acceleration / injection process responsible for the radio emission (Aschwanden, 1987). The modulation is likely to be communicated on magneto-hydrodynamic (MHD) timescales in the acceleration region Asai *et al.* (2001); Aschwanden *et al.* (1994); Kliem *et al.* (2000); Tajima *et al.* (1987). In such cases the corresponding Alfvén speed (v_A) can be estimated as,

$$v_A \approx \frac{l}{p} \tag{4.2}$$

where $l \approx 10000$ km is the typical dimension of the region over which the type III radio burst producing electrons are injected (Aschwanden, 2002; Lantos *et al.*, 1984), and p is the observed periodicity. Once v_A is known, the associated magnetic field strength (B) can be calculated using the expression,

$$v_A = 2.05 \times 10^6 B N_e^{-1/2} \tag{4.3}$$

where N_e is the electron density (corresponding to either f or $f/2$, depending on whether the observed emission corresponds to the fundamental or the harmonic component, respectively) in units of cm^{-3}.

The magnetic field strengths (corresponding to the above values of p) estimated using equations (4.2) and (4.3) are in the range $B \approx 0.96 - 0.06$ G. Interestingly, the estimates for the other three events are also nearly the same (see Table 4.3). This adds confidence to our results. We have assumed that the quasi-periodic radio bursts in Table 4.3 are due to second harmonic plasma emission since the viewing angle of the sunspot active regions associated with all the bursts is $\gtrsim 30°$. Further the fundamental plasma emission is more directive at low frequencies (Suzuki and Sheridan, 1982).

4.6 Discussions

The multiple periodicities in each event listed in Table 4.3 indicate that the observed quasi-periodic pulsations are possibly due to interaction of different magnetic structures (see for eg. Tomczak and Sfaforz (2014)). Each pulsation correspond to a burst of electron acceleration in a reconnection region. The episodes of acceleration/reconnection occur at different locations, but are triggered by a common phenomenon (Benz, 1994). Note that the probability of interaction and reconnection between an expanding CME and the neighboring open magnetic field structures, leading to generation of groups of type III radio bursts is also very high (see for eg. Goff *et al.* (2007)). The applicability of the above arguments to the present case is further strengthened by the reports that there is large scale reconfiguration of the coronal magnetic field (which facilitates reconnection) in the aftermath of a 'halo' CME. The time period over which this occurs is $\lesssim$ 19 h (Hansen *et al.*, 1974; Hiei *et al.*, 1993; Kathiravan *et al.*, 2007). The upper limit of the above period is nearly the same as the period ($\approx$ 20 h) reported by Tsuneta *et al.* (1992) in the context of global restructuring of the corona due to magnetic reconnections after the disappearance of a polar crown filament. Interestingly the latter is usually associated with the CMEs. Therefore multiple magnetic reconnections in the aftermath of either the partial 'halo' or 'halo' CMEs could be the cause of the quasi-periodicity for the four long duration bursts listed in Table 4.3 because: 1) neither partial 'halo' nor 'halo' CMEs were associated with the other eight long duration bursts that did not show any quasi-periodicity (see Section 4.4); 2) statistical results show that group of type III bursts observed at low frequencies are always preceded by CMEs of width $> 140°$ (Cane *et al.*, 2002). The rapid and irregular variations in the peak amplitudes of the pulsations point to a bursty, time dependant reconnection process in the present case (see for eg. Aschwanden (2004); Kliem *et al.* (2000)). An estimate of the v_A values (using equation 4.2) corresponding to the range of periodicities for each event listed in Table 4.3 indicates that the spread in the former agrees well with the coalescence speeds ($\approx 200-2000 km/s$) of the magnetic islands which lead to the burst of electron acceleration in the above reconnection process (Aschwanden, 2002). These imply that radio observations of quasi-periodic pulsations could be an useful tool to estimate the coronal plasma parameters in the reconnection/electron acceleration regions.

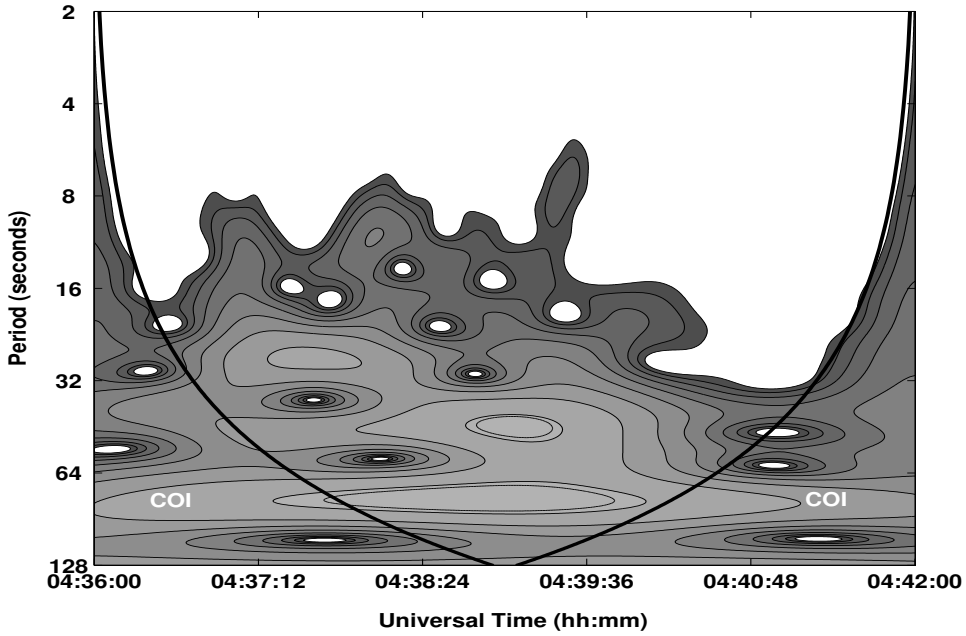

Figure 4.6: Wavelet spectrum for the 19.5 MHz correlation mode time profile in Figure 4.5. The region marked COI is the 'cone of influence' in which the edge effects become important due to the limited time series data and have a higher contribution of artefacts. Portions of the spectrum present within the COI as well as close to either side of its boundary should be treated with caution because of the aforementioned reason (see for eg. Torrence and Compo (1998)).

4.7 Summary

A low frequency (30 - 15 MHz) spectro-correlator for solar observations was recently commissioned at the GRO using high speed digitizer and FPGA hardware for the back end instrumentation. Observations indicate that the dynamic range is higher than that obtained using the conventional techniques. Located at $\approx 77°$E 13$\circ$N, the above instrument provides the possibility to have continuous observations of the Sun for $\approx$ 15 h in a day (at present) along with other similar low frequency spectrographs located at other terrestrial longitudes. We are exploring the possibilities to carry out continuous observations for more than 15 h in a day. Moreover it minimizes the spectral gap with the Wind-Waves observations. Wavelet analysis of the group of long duration (> 100 s) type III solar radio bursts observed with our spectrograph indicate that those which are preceded by either partial 'halo' or 'halo' CMEs are quasi-periodic with periodicities in the range $p \approx 4$ - 75 sec at a typical frequency like 19.5 MHz. The coronal magnetic field strengths calculated using the above periodicities are in the range $B \approx 1.00 - 0.06$ G. Note that radio emission at low frequencies originate

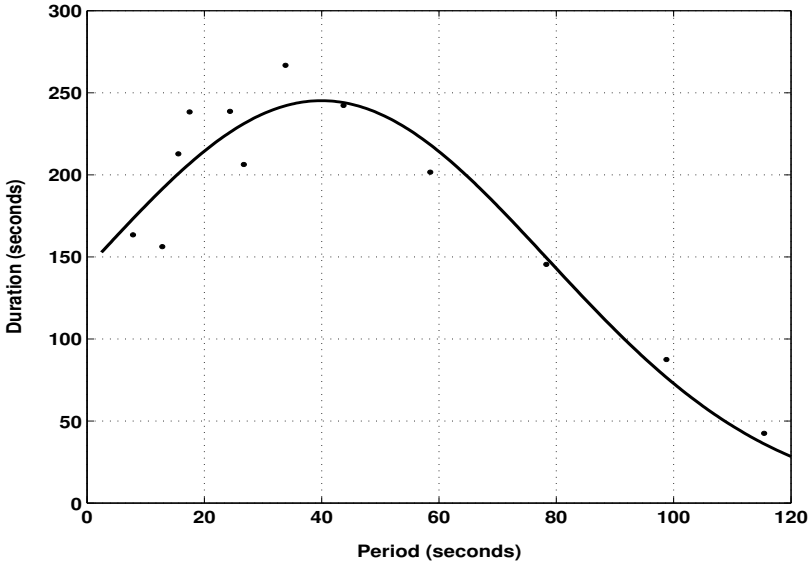

Figure 4.7: Distribution of the duration of the different periodicities outside the COI in Figure 4.6, obtained by taking horizontal slices through the latter. The dashed line is the 'fit' to the estimated periodicities.

typically in the 'middle' corona ($1.2\ R_\odot \lesssim r \lesssim 3\ R_\odot$) where r is the heliocentric distance. Observations over the above range of r at other frequency bands in the electromagnetic spectrum are presently limited. Hence radio observations similar to that reported in the present work could be an effective tool for routine monitoring and seismology in the aforementioned region of the solar atmosphere to understand the plasma parameters there. A number of scientific problems, for eg. the CME-solar energetic protons (SEP)-low frequency type III burst (type III-l) association in the context of the Space Weather studies, can also be investigated (Cliver and Ling, 2009; MacDowall *et al.*, 2003). Additionally, the corona overlying the visible solar disk as well off its limb can be simultaneously observed; weak energy releases in the solar atmosphere can be observed with good contrast via the associated non-thermal radio emission (Benz, 1995; Li *et al.*, 2009). Finally, the cross-correlation scheme described in this work can be successfully extended to observations of non-solar transients also. Since the antenna and the receiver system described in the present work can be easily reconfigured to observe at frequencies < 15 MHz, we should be able to achieve spectral overlap with Wind-Waves observations. As a follow-up to the present work we wanted to extend the observations on the high frequency side to have continuous spectral coverage till ≈ 100 MHz. The data rate should not be a problem since stand alone FPGA systems with fast ADCs and facilities for on-board processing are

available[3], commercially. Such a wide-band spectrometer back-end was developed and tested which is described in the next chapter.

[3]http://www.xilinx.com/univ/xupv5-lx110t.htm

Table 4.4: List of radio bursts observed with the spectrograph

No.	Date	Time (UT)	Duration (s)
1	2013/10/18	07:08	12
2	2013/10/20	04:33	18
3		05:20	14
4		05:34	18
5		05:45	25
6		06:52	21
7		06:57	18
8		07:23	115
9	2013/10/21	05:11	19
10		06:21	7
11		06:44	17
12		07:29	18
13		08:08	12
14		08:35	100
15		09:22	57
16	2013/10/23	09:56	20
17		05:12	30
18		07:49	28
19	2013/10/28	04:36	288
20	2013/11/02	04:44	36
21		06:03	23
22		06:19	18
23		06:48	33
24	2013/11/05	06:00	36
25	2013/11/07	03:38	12
26	2013/11/20	05:49	108
27	2013/11/21	07:31	11
28	2013/11/23	08:45	14
29	2013/11/24	06:06	25
30	2013/11/28	08:14	7
31	2013/12/04	05:12	14
32	2013/12/05	05:36	16
33		06:36	25
34	2013/12/07	07:22	144

35	2013/12/14	03:06	18
36		06:24	72
37		07:07	43
38		08:21	21
39	2013/12/15	04:21	19
40		06:30	14
41		07:13	25
42		08:15	18
43		10:30	58
44	2013/12/16	06:58	7
45		07:24	2
46	2013/12/23	06:27	18
47	2013/12/26	05:08	18
48		05:58	64
49	2013/12/28	07:02	216
50	2013/12/30	04:01	12
51		05:54	46
52		07:49	104
53		08:06	23
54	2014/01/18	04:35	108
55	2014/01/24	08:07	21
56	2014/01/26	10:09	144
57	2014/01/27	05:24	14
58		06:02	32
59		07:49	7
60	2014/01/28	05:31	63
61		06:06	7
62		07:28	237
63		09:34	9
64		09:36	6
65	2014/01/29	04:18	64
66		07:28	27
67	2014/01/30	06:06	14
68	2014/01/31	05:42	108
69		07:25	118
70	2014/02/02	09:29	20
71	2014/02/03	04:45	21

Chapter 5

Wide-band FFT Spectrometer

5.1 Introduction

A large part of astronomical data processing and analysis is now performed by receivers based on digital hardware and they prove to be more reliable in terms of system stability and affordability. Particularly in the case of moodern radio telescopes, digital processing of the RF signal can start practically at the output of each dipole. The broad frequency coverage, scalability and reconfigurability of the system design of the digital equipment in addition to the processing algorithms have taken radio astronomy research to a new technological level (Zakharenko *et al.*, 2016). Low-frequency solar radio observations (below 100 MHz) are of particular astrophysical interest due to the non-thermal nature of emission and related physical processes that operate at these frequencies (Section 1.2). In this range, despite the relatively narrow absolute frequency band, the upper-to-lower frequency ratio often exceeds several octaves. This helps to measure frequency-dependent emission parameters with high accuracy, possibly leading to important astrophysical conclusions. The simultaneous broad-band coverage with high spectral and temporal resolution offered by modern digital receivers makes it convenient to record the entire low-frequency range almost instantaneously (in the baseband or in upper Nyquist zones: f = [n, n + 1]$f_{sampling}$/2 with n = 0, 1, 2,. . .). The amplitude resolution and the dynamic range of measurements has governed by the number of bits of the analog-to-digital converters (ADC) which has significantly increased over the years. This is especially important for the frequencies below 30 MHz where radio frequency interference (RFI) from broadcasting stations are many orders of magnitude stronger than the weak cosmic signals.

In chapter 3, the usefulness of the high dynamic range and the high spectro-temporal resolution offered by such digital back-end recorder was presented. In view

of the recent upgradation of the back-end receivers for the instruments at the Gauribidanur Observatory, a new digital back-end based on high-speed ADC-FPGA hardware was configured for radio spectral observations of the Sun in the frequency range 40−80 MHz. The details of the hardware and the observational results obtained are described in the subsequent sections.

5.2 Wide-band Digital Data Recorder

The wide-band digital recorder consists of two sub-modules which involve data digitaization and packetization. The packetized data is then transferred to the computer where the data acquisition and pre-processing is performed on software.

5.2.1 High-Speed ADC Module

A commercially available ADC evaluation card was procured for this purpose from Analog Devices. The card is based on AD9286 chip which is an 8-bit dual core pipelined-ADC with a maximum sampling rate of 500 MSPS. The output of the ADC is available as Low-Voltage Differential Signal (LVDS) for better isolation from spurious noise pick-up. The analog input on the evaluation board in its default configuration uses a single transformer input with a 50 Ω impedance. The default analog input configuration supports analog input frequencies of up to ≈ 200 MHz and is optimized to support a broad frequency range. The ADC can be operated with various parameter settings which are controlled through registers available on the ADC chip. The registers are accessed via Serial Peripheral Interface (SPI) in order to set the various parameters of the ADC for a particular mode of operation. The various parameter settings are as follows :

i) **Clocking mode** : The ADC can be operated in two clocking modes: simultaneous and interleaved. In the simultaneous mode, both the ADC cores simultaneously sample the same data stream at the same sampling clock edge. The maximum sampling rate possible in this mode is 250 MSPS. In the interleaved mode, the data stream is sampled by both the cores, but the sampling clock to either core will be 180° out of phase with respect to the other and in this mode a maximum sampling rate of 500 MSPS is achievable.

ii) **DC offset** : Due to the multi-core architecture of the ADC there are possible bias voltage mismatch with respect to the ground of the board and this shows as a DC

offset in the digitized waveform data. This can be corrected by setting specific count values for a register where each increment or decrement of the count corresponds to a certain percentage of the full-scale reference voltage of the ADC board.

iii) **Data Format** : The data format of the ADC can be either offset binary or two's complement which is left to the convenience of the user and the choice is made by setting the appropriate registers.

5.2.1.1 Characteristics of ADC

The dynamic performance of an ADC is quantified by various specifications and these have been listed below. All of the specifications relate to the distortion and noise performance of the ADC and can be determined based on FFT analysis. We recorded the digitized waveform dataset from the ADC and spectral analysis was carried out to characterize its performance.

i) **Signal to Noise Distortion Ratio (SINAD)** : Signal to noise ratio (SNR) of the ADC determines the quality of the signal that is reproduced by the ADC. It is the difference between the signal power to the noise floor of the ADC. SINAD is similar to the SNR of the ADC and it is the ratio of signal power to the power at all other noise components including the harmonics in the spectrum. It is an indicator of the ac performance of the ADC in the presence of high frequency distortion effects. It can be noted that the SINAD increases with the increase of full-scale reference voltage (Figure 5.2)

ii) **Effective Number of Bits (ENOB)** : Although the bit resolution of an ADC is mentioned by a quantitative number. Due to various reasons the effective number of bits that goes into the quantization of the signal is much lesser than that specified in the data sheets. Figures 5.1 and 5.2 show the variation of ENOB as a function of frequency and the full-scale reference voltage V_{FS}. The full-scale reference voltage is to be chosen such that the band-limited input signal is accomodated well-within the range and maximum number of bits are utilized to accommodate the signal. It is clearly seen that the ENOB is higher with a better and closer choise of the V_{FS} with respect to the input signal amplitude. It should be noted that the ENOB can be estimated from SINAD using equation 5.1.

$$ENOB = \frac{(20\log_{10} SINAD - 1.76dB)}{6.02} \tag{5.1}$$

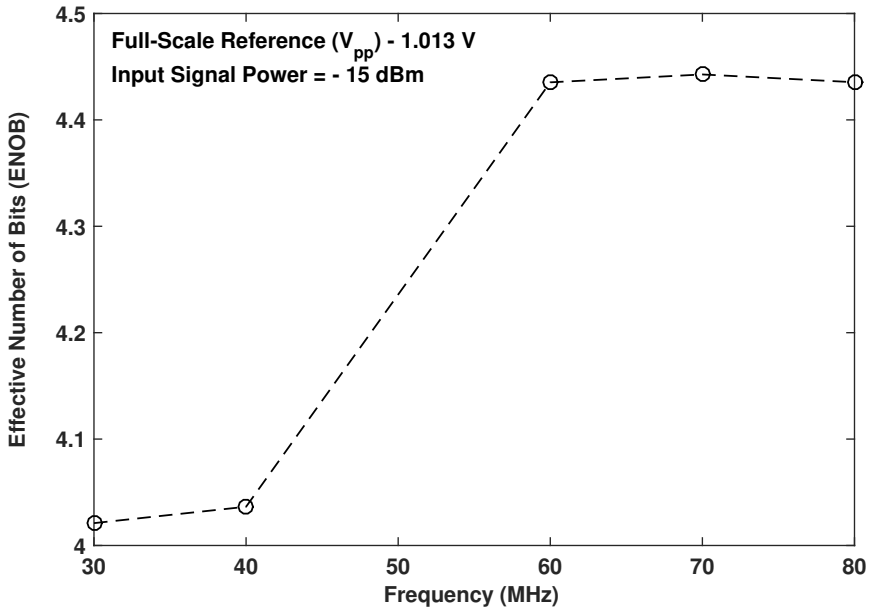

Figure 5.1: Variation of ENOB as a function of frequency for an input CW signal at different frequencies at a power level of -15 dBm

From the SINAD and ENOB performance it was determined that ideal power of a band-limited signal for the ADC can be in the range ≈ -10 − -20 dBm particularly for solar radio observations. This ensures that only 4 to 5 bits are used in quantization of the background noise and there is provision of further 3 bits to detect a radio burst without saturation of the ADC.

iii) **Spur-Free Dynamic Range (SFDR)** : It is the ratio of the input signal to the power level of the largest distortion component. SFDR is useful to determine the minimum signal level that can be distinguished from distortion components. It is seen from the Figure 5.3 that the SFDR inreases as we increase the input signal voltage close to the decreases as the input signal voltage is increased close to the ADC. It is most often the second or third harmonic of the carrier frequency that dominates to be the spurious signal and hence the SFDR is mostly dominated by the dynamic range between the carrier and the second harmonic component.

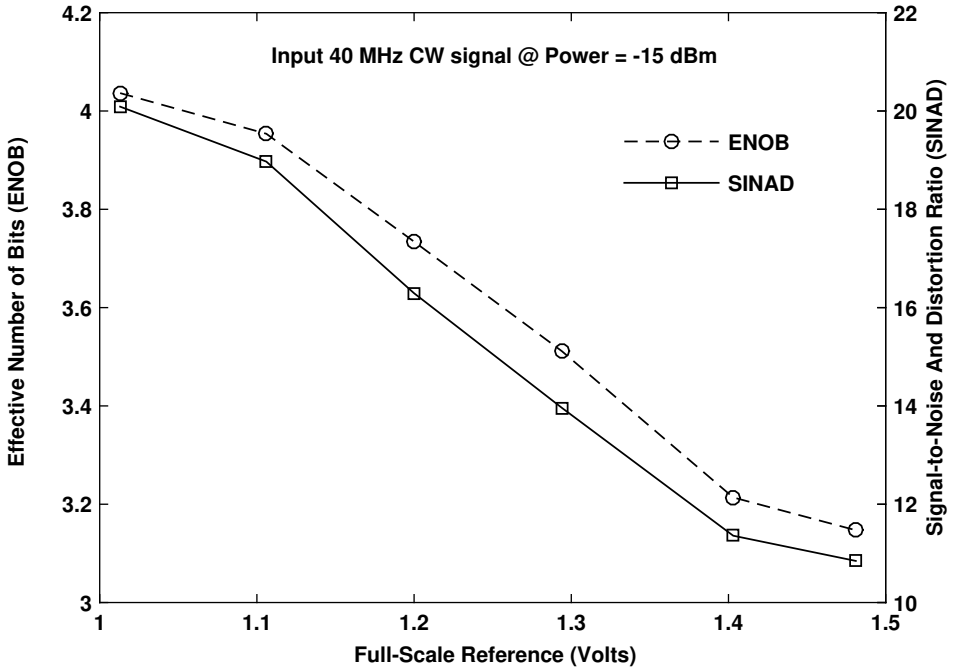

(a)

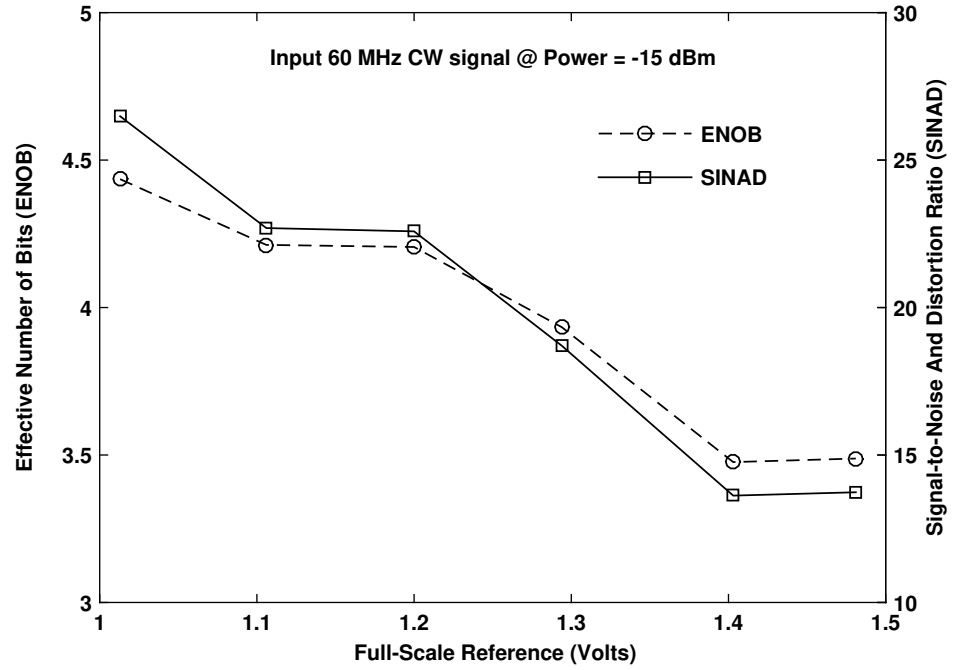

(b)

Figure 5.2: Variation of SINAD and ENOB at different full-scale reference voltage V_{FS} setting for the ADC : a) Input CW signal of 40 MHz at a power level of -15 dBm; b) Input CW signal of 60 MHz at a power level of -15 dBm

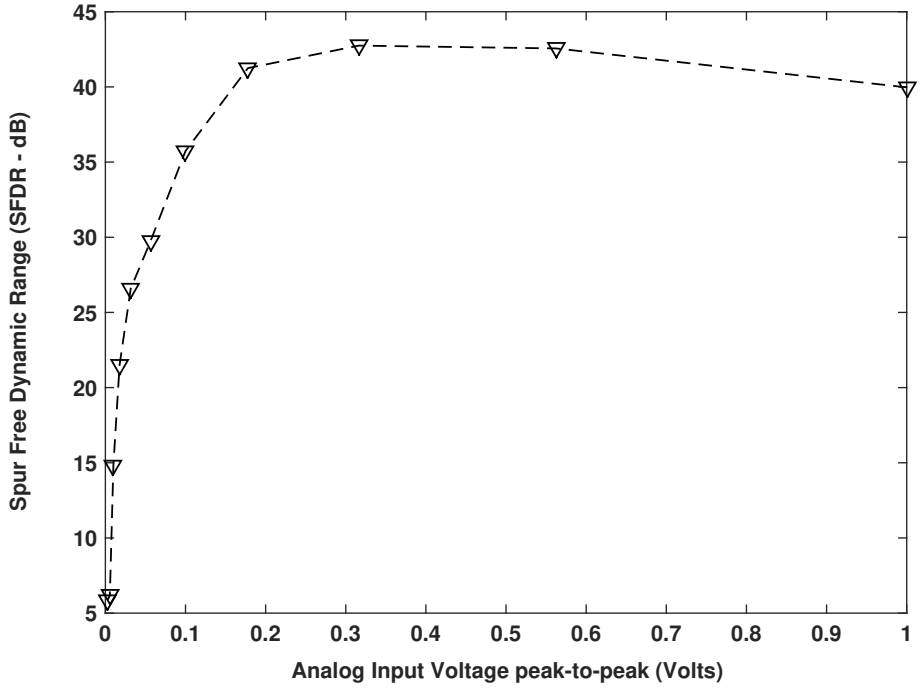

Figure 5.3: Variation of SFDR for different amplitudes (V_{pp}) of analog input CW signal at 40 MHz with ADC full-scale refernce V_{FS} = 1.013 V

iv) **Total Harmonic Distortion (THD)** : It is the ratio of the rms value of the fundamental signal to the mean value of the root-sum-square of its harmonics and a measure of the harmonics at the output of the ADC. Harmonics are generated by distortion at the ADC output due to missing code or by any nonlinearity present in the ADC characteristics. Figure 5.5 shows that THD decreases as the input signal voltage is increased close to the full-scale voltage range of the ADC.

From the characterization tests and analysis we found the performance of the ADC to be optimum for an input signal level is ≈ -10 dBm with a full-scale reference voltage of 1.013 V. The ADC is provided with Parameters like the DC offset, format of the output bits (2's complement, offset binary etc.), and the clocking modes of the ADC can be set through a Serial Peripheral Interface (SPI). The parameters of the ADC card are mentioned in table.

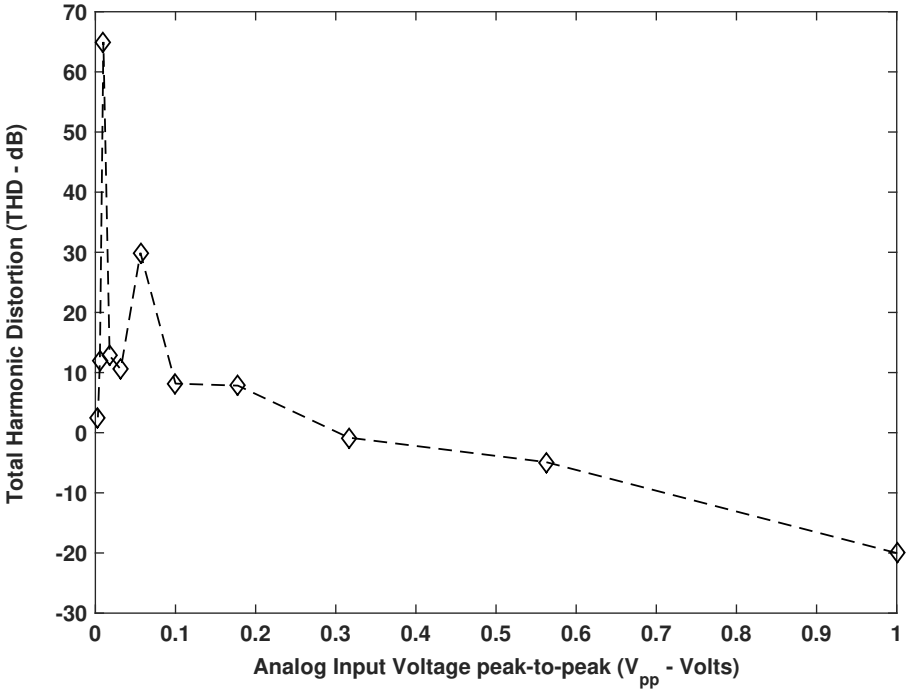

Figure 5.4: Variation of THD for different amplitudes (V_{pp}) of analog input CW signal at 40 MHz with ADC full-scale refernce $V_{FS} = 1.013$ V

5.2.2 FPGA Data Capture Module

A Xilinx Virtex-4 FPGA chip based evaluation board is interfaced with the ADC card for capturing the digitized data. An on-chip data buffer is implemented as a FIFO (First-In-First-Out) on the FPGA chip. The FIFO can have a maximum memory capacity of $\approx$ 65535 samples of 8-bit width. The evaluation board is interfaced to a computer through a standard Universal Serial Bus (USB) interface which supports a maximum data transfer rate of $\approx$ 480 MB/sec. Analog Devices based 'Visual Analog' is used as the software interface for programming the FPGA with a FIFO and for retrieving the data from it. In the FPGA chip a FIFO of appropriate length, which is basically the number of samples to be acquired. The poll signal is sent by the software via USB interface to monitor the status of the FIFO and retrive the data from the FIFO once it is filled. The retrieved data is then processed in realtime on software as described in section 5.3.2

5.3 Impelmentation of Spectrometer

5.3.1 Observational Set-up

A new array, named Gauribidanur LOw frequency Solar Spectrograph (GLOSS: Kishore *et al.*, 2015), was recently built and commissioned for regular spectral observations of the Sun. It is a phased array of eight log-periodic antenna elements along the NS direction with the antenna 'arms' oriented along the EW direction. The half-power width of the response pattern of GLOSS at a typical frequency like 80 MHz is approximately 90°× 6° (R.A. Decl.). It is a total power instrument and useful for recording the dynamic spectrum of the sun over a period of eight hours everyday. It is used in the identification of the type of radio burst and useful for calculating plasma parameters using the various features in the bursts. For a more technical description about the GLOSS array the reader is encouraged to read GLOSS: Kishore *et al.*, 2015.

The analog RF signal from the GLOSS array is filtered, amplified and brought to the receiver room via low-loss RF coaxial cable buried at ≈ 1m beneath the ground. The RF signal at the receiver room is given to a band-pass filter with a pass-band of $40 - 80$ MHz. This band-limited signal is then amplified and fed to the ADC analog input as shown in Figure 5.5. The ADC is clocked at 200 MHz sampling a base-band of 100 MHz signal which is digitized to 8-bit LVDS. The ADC card is interfaced with the H-pack HM-Zd connector, which supports high speed data transmission, with the FPGA evaluation card and the digitized data is written into the FIFO configured on the FPGA.

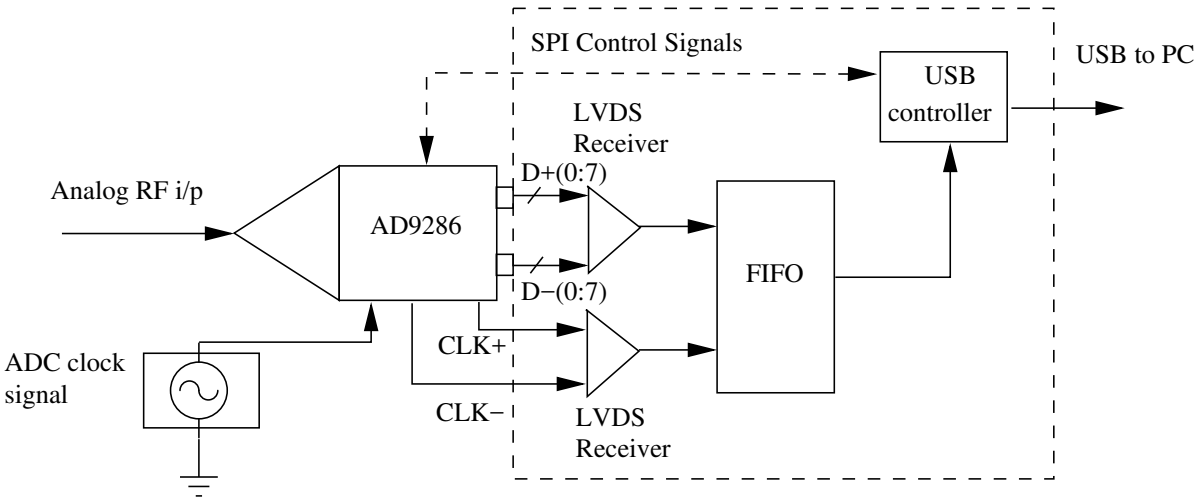

Figure 5.5: Block Diagram of the Digital Data Recorder

5.3.2 Data Acquisition and pre-processing

The data is retrieved from the FPGA in 8-bit offset binary format into the 'Visual Analog' software environment and is windowed by hanning function which is useful in reducing the FFT scalloping loss due to the discontinuos nature of the sample waveform. The windowed waveform is then processed by an FFT block and the spectral data-set is thus obtained which is then written to a binary file in the PC for post-processing. So a real-time software spectrograph is configured this way to operate in the frequency range 40−80 MHz. Note that the data acquisition is performed in burst mode in view of data rate and data handling issues and this results in a time gap of ≈ 10 msec between successive data acquisitions. Note that the life-time of the solar radio transients is > 1 sec at low frequencies (McLean and Labrum, 1985). So the above time gap should not affect the observations.

5.3.3 Comparison with Analog Back-End Receiver

Table 5.1: Comparison of Analog and Digital Spectrograph Specifications

Frequency Range	45−85 MHz	0−100 MHz
Number of frequency channels	401	4096
Frequency Resolution	≈ 175 kHz	≈ 24 kHz
Dwell time	≈ 30.9 ms	≈ 20 μ s
Time Resolution (Data ransfer + pre-processing time)	≈ 250 ms	≈ 20 ms

In-order to validate the new digital back-end receiver, a set of trial-run observations were carried out over the period from February-March, 2014 with both the existing analog spectrum analyzer and the new back-end. The comparitive features of both the analog and digital spectrograph configurations are listed in Table 5.1. It can be clearly seen that the digital spectrograph fares better in terms of spectral and temporal resolution. With such a high spectal resolution it is possible to identify and remove the RFI channels during offline analysis which would otherwise corrupt the data sat. This helps us to improve the dynamic range of waterfall plots of the spectral data. Though the dwell-time for the digital back-end is relatively very less, it may not affect the observations of solar radio bursts which tend to be quite strong in intensity in the operating frequency range. This can be clearly visualized in the dynamic spectrum of a type III radio burst in Figure 5.6 observed on 23, February, 2014 by both the analog and digital receivers. It can be seen that some of the

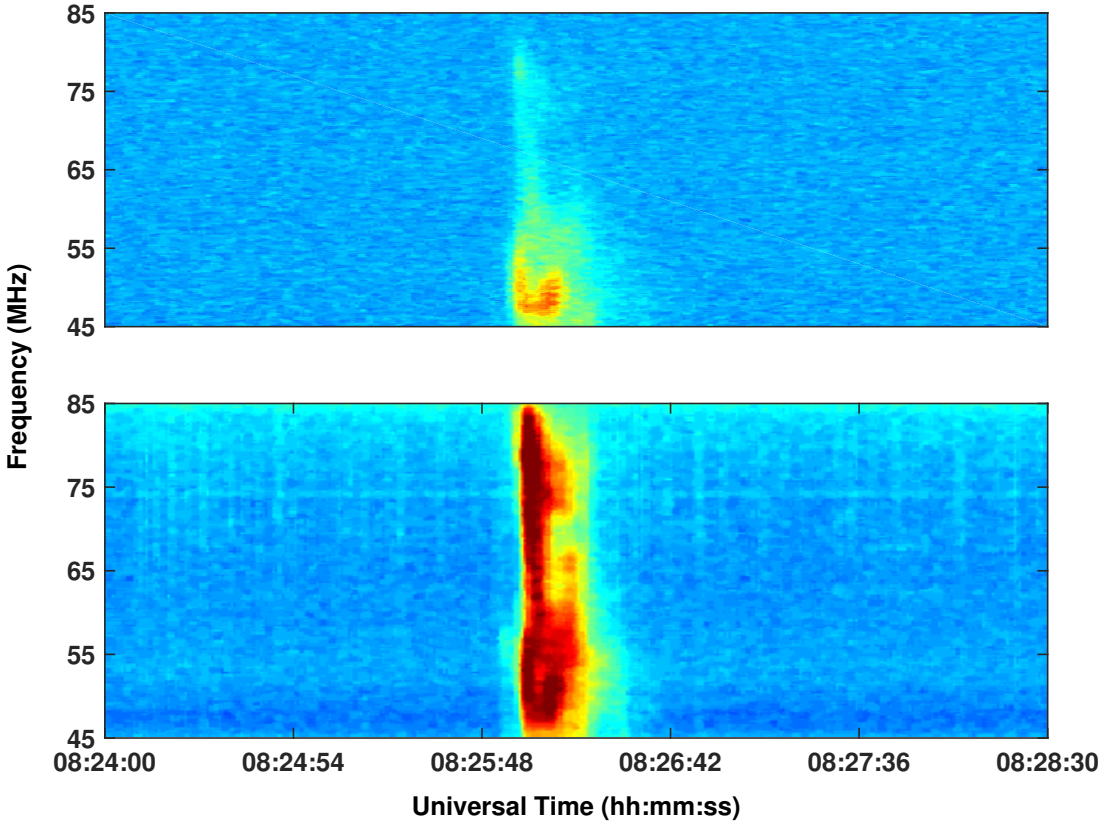

Figure 5.6: Dynamic Spectrum of Type-III radio burst recorded on 2014/02/23 around 8:25 UT at the GRO with GLOSS using the analog back-end (Top panel) and the digital back-end Bottom panel)

features of the type-III burst seem to be more pronounced in the digital spectrograph and a comparison of the Signal-to-Noise Ratio (SNR) calculated from the temporal profile of the radio burst at particular spot-frequencies (Figure 5.7 is indicative of the advantages of the new digital back-end receiver.

5.4 Observations

In the subsequent sections we describe the near-Sun ($r \lesssim 2\ R_{\odot}$) radio spectral observation of a type IVm burst that was co-spatial with the leading edge (LE) of a white light CME. we also present the radio heliograph and radio polarimetric measurements of the burst in conjunction with the space-borne observations and finally discuss the inherent fine structure phenomena.

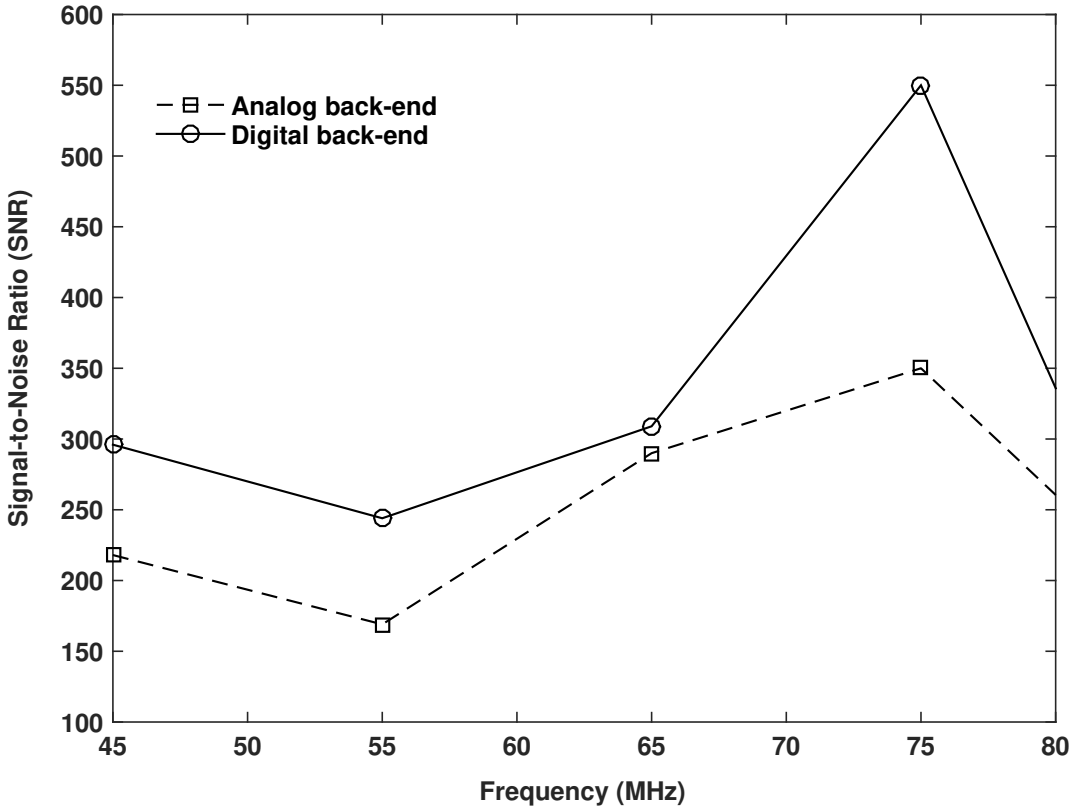

Figure 5.7: Distribution of the Signal-to-Noise ratio for the radio burst shown in Figure 5.6 against frequency for both the analog and digital back-end

Prologue to Solar Type IV Radio Bursts Quasi-continuum radio emissions of duration 10-60 min that occur along with flares and coronal mass ejections (CMEs) in the solar atmosphere are termed as type IV bursts. The bursts are non-thermal in nature and can be classified into two categories, *i.e.* moving type IV (type IVm) bursts and stationary type IV (type IVs) bursts, depending on their time-frequency characteristics in the dynamic spectrum. Amongst the two, the former has a comparatively closer association with the CMEs; they accompany nearly 5% of the CMEs Gergely (1986); Stewart (1985). This provides an opportunity to independently infer the characteristic parameters of CMEs (the electron density, the strength of the associated coronal magnetic field, *etc.*) from simultaneous observations of the two phenomena. Ever since the launch of space missions like the *Solar and Heliospheric Observatory* (SoHO; Domingo, Fleck, and Poland, 1995) and the *Solar-Terrestrial Relations Observatory*, it has become possible to observe the CMEs with comparatively good contrast, better time cadence, and more closer to the Sun. Further the

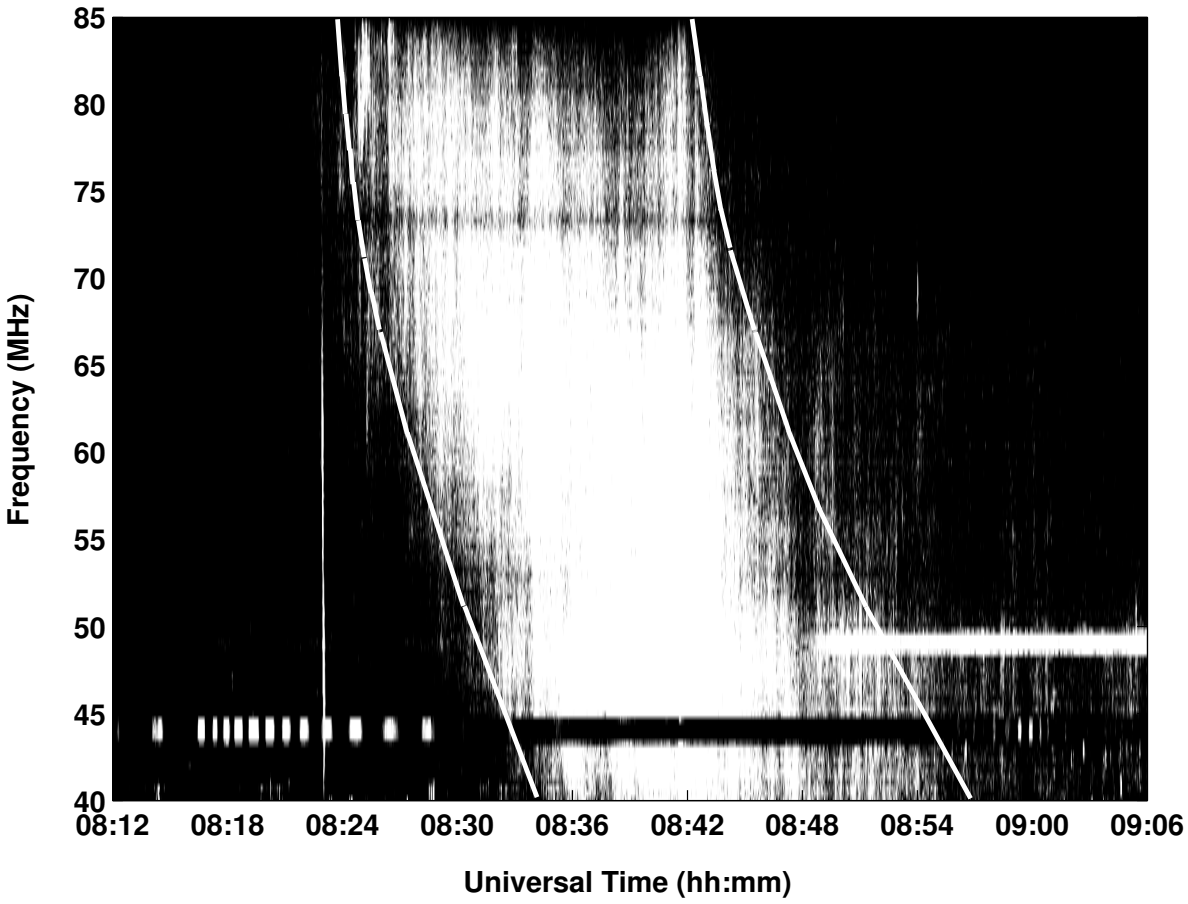

Figure 5.8: Dynamic spectrum of the type IVm radio burst observed with the GLOSS on 31 March 2014 during 08:24-08:56 UT in the frequency range 40-85 MHz. Observations with frequencies lower than 40 MHz are not shown here as they were affected by local radio frequency interference (RFI). The horizontal patches near 45, 50 and 75 MHz are also due to RFI. The 'vertical' emission feature close to 08:22 UT is a type III burst. The two slanted 'white' lines indicate the approximate onset and the end of the burst at different frequencies.

observations are nearly continuous over the 24 h period in a day. The corresponding coronal electron density estimates are also possible (see *eg.* Wang and Davila, 2014; Zucca *et al.*, 2014). These advantages facilitate comparison with complimentary and simultaneous ground based observations of the associated radio transients.

Figure 5.8 shows the GLOSS observations of a type IVm radio burst on 31 March 2014 during the interval of 08:24−08:56 UT. The duration of the burst at individual spot frequencies was nearly the same ($\approx$ 20 min) in the frequency range 40−85 MHz. The presence of a type III burst close to 08:22 UT, prior to the type IVm burst, can

also be noticed in the dynamic spectrum. Observations with the e-CALLISTO solar radio spectrometer at the Gauribidanur Radio Observatory over the frequency range of 45−440 MHz Benz *et al.* (2009); Monstein *et al.* (2007) indicates that the type IVm burst was limited to frequencies below 100 MHz.

Figures 5.9 and 5.10 show the transit mode observations with the GRIP at 65 and 80 MHz, respectively. The observations correspond to different intervals during the lifetime of the type IVm burst in Figure 5.8. Since the width of the beam pattern of the GRIP in the east-west direction is narrower compared to that of the GLOSS, the duration of the observations was limited. The estimated Stokes I peak flux densities of the burst at 65 and 80 MHz are approximately 112000 Jy and 57700 Jy, respectively. The corresponding estimates for Stokes V are approximately 900 Jy (65 MHz) and 4100 Jy (80 MHz). The degree of circular polarization (DCP = $|V|/I$) calculated using the above values is approximately 1% and 7% at 65 and 80 MHz, respectively.

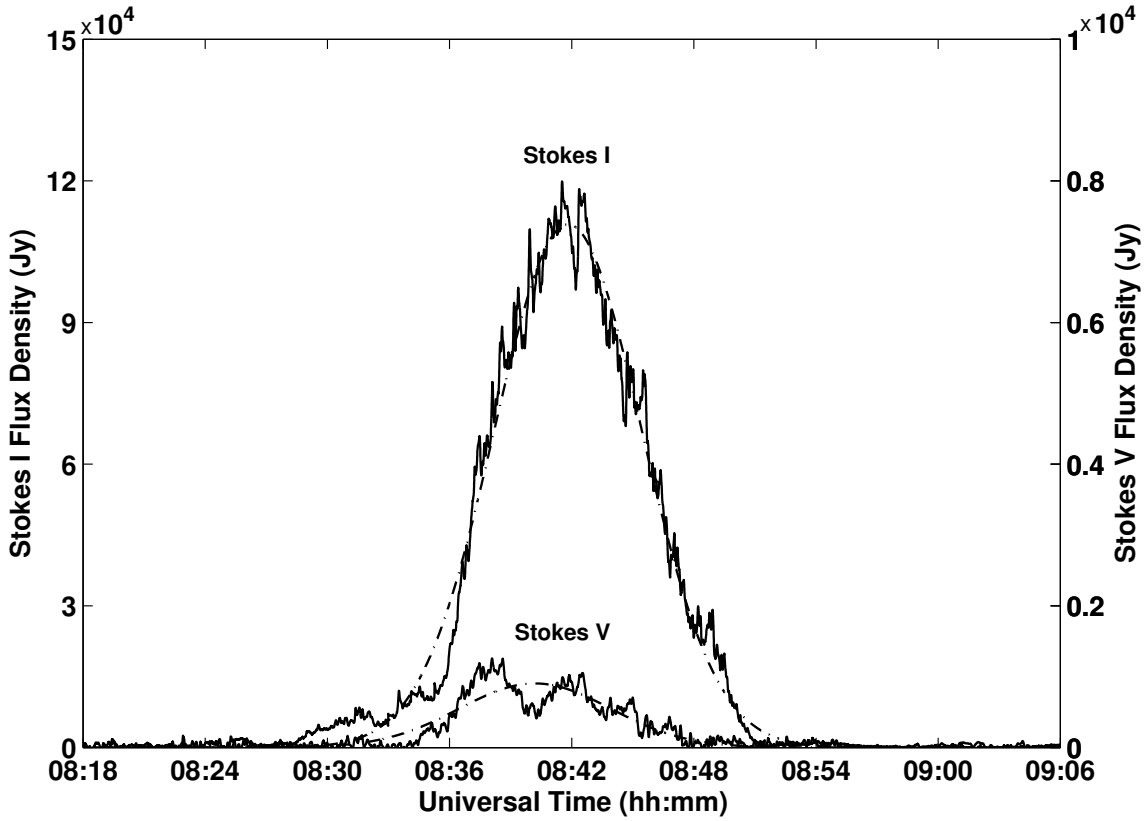

Figure 5.9: Stokes I and V time profiles of the type IVm burst observed with the GRIP on 31 March 2014 at 65 MHz. The dot-dashed lines superposed on the time profiles are the 'fit' to the observations.

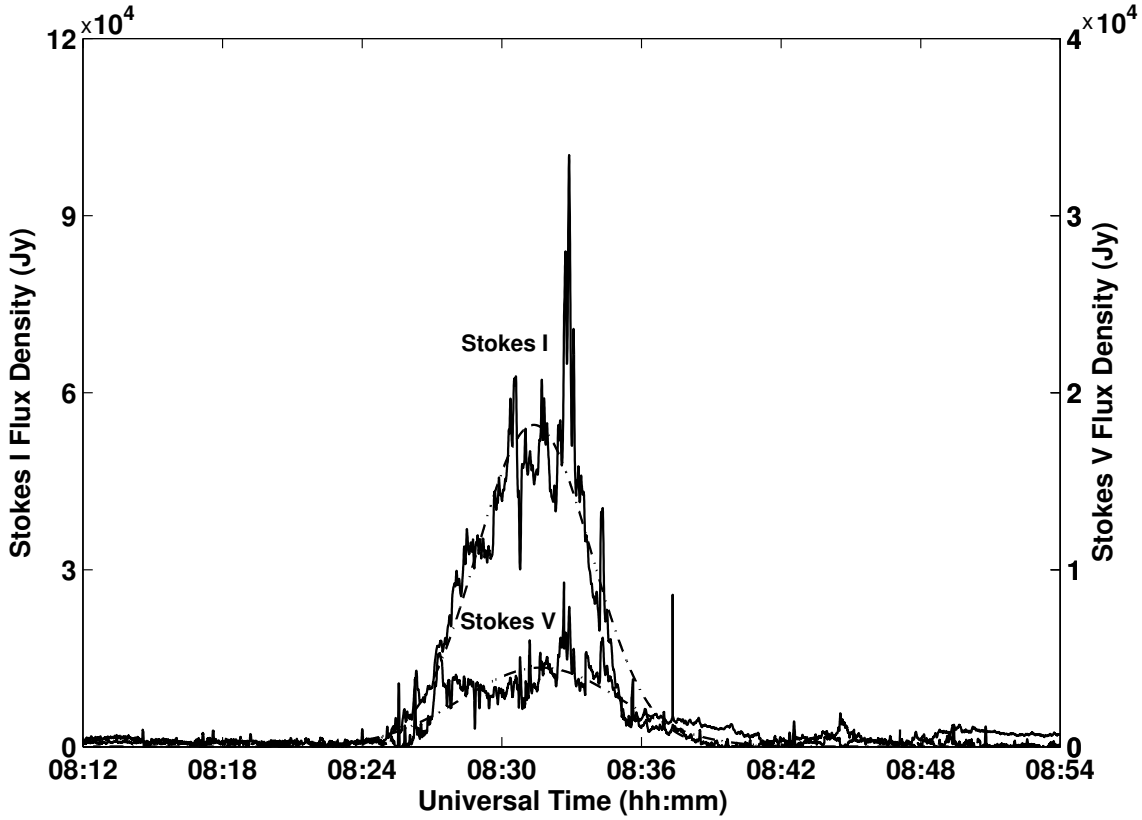

Figure 5.10: Same as Figure 5.9, but at 80 MHz.

Figure 5.11 shows the composite of the SOHO/-LASCO–C2 and SDO/-AIA 193 Å images obtained on 31 March 2014 at 08:36 UT, and GRAPH observations of the type IVm burst that day at 08:26 UT. The projected heliocentric distance ($r_{\rm radio}$) of the centroid of the radio burst is 2.2 $R_{\odot}$. The peak radio brightness temperature ($T_{\rm b}$) is 7×10^7 K. Any error in the above values due to irregular refraction in the solar corona is expected to be minimal since it is pronounced primarily at lower frequencies Aubier, Leblanc and Boischot (1971); Bastain (2004); Ramesh, Sundara Rajan and Shastry (2006); Riddle (1974); Thejappa and MacDowall (2008). But the effect of minimal angular resolution of the GRAPH on the derived $T_{\rm b}$ values could not be ruled out since high angular resolution observations at low frequencies with other instruments indicate the presence of solar radio sources of smaller sizes (Kerdraon, 1979; Lang and Wilson, 1987; Willson *et al.*, 1998; Ramesh *et al.*, 1999; 2012; Ramesh and Sastry, 2000; Ramesh and Ebenezer, 2001; Mercier *et al.*, 2006; 2015; Kathiravan *et al.*, 2011). The intense emission in the south-west quadrant of the SOHO/-LASCO–C2

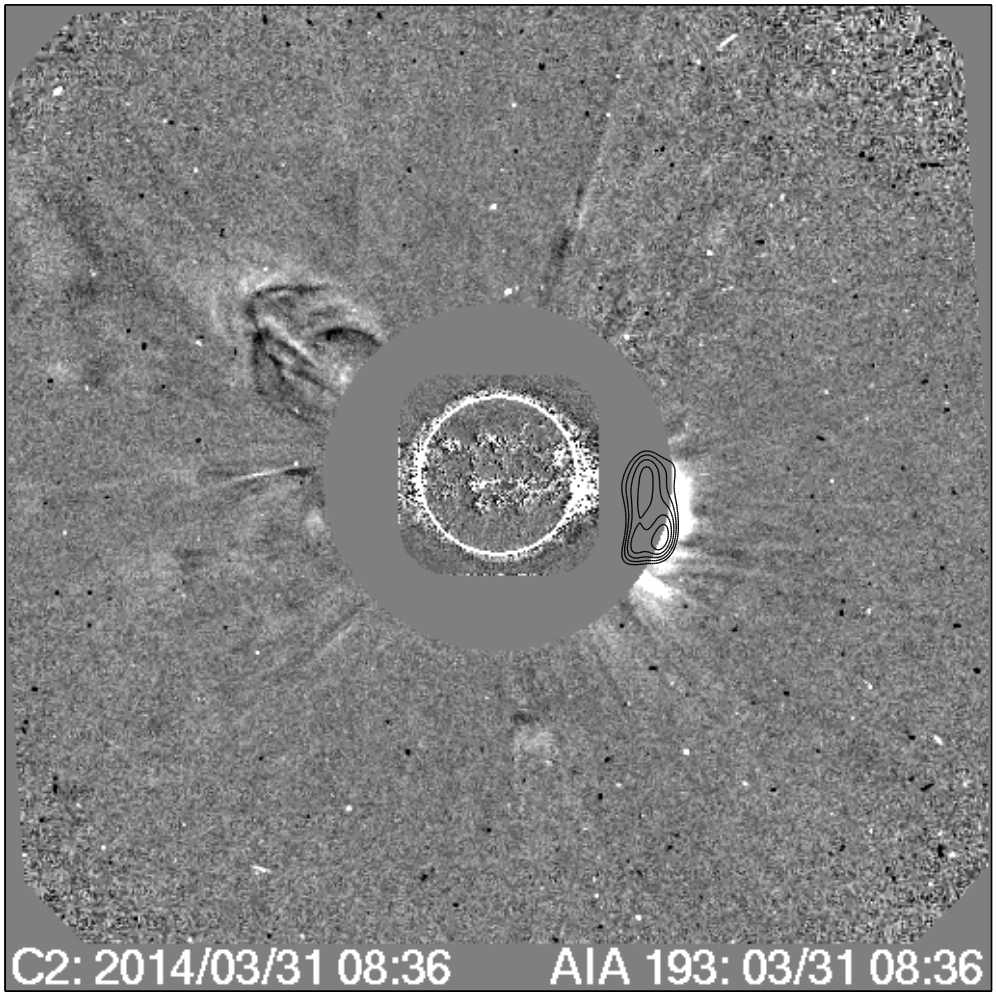

Figure 5.11: A composite of the SOHO/-LASCO–C2, SDO/-AIA 193 Å images obtained on 31 March 2014 at 08:36 UT, and radio contours (up-to 50% level) of the type IVm burst observed that day with the GRAPH at 80 MHz (over a bandwidth of $\approx$ 2 MHz; see Section 5.4) close to 08:26 UT. The enhanced white-light emission to the right of the radio burst source corresponds to the CME described in Section 5.4. The 'white' circle (radius = 1 $R_{\odot}$) at the center indicates the solar limb. The bigger, concentric 'gray' circle (radius = 2.2 $R_{\odot}$) represents the occulting disk of the SOHO/-LASCO–C2 coronagraph. Solar north is straight up and solar east is to the left in the image.

field of view (FOV) corresponds to a CME[1]. There was an associated SF class Hα flare and M1.4 class GOES soft X-ray flare (with peak emission at 08:07 UT) from the active region AR12014 located at the heliographic coordinates S15W77[2]. The latter suggests that the angle between the CME and the plane of the sky (POS) is

[1]cdaw.nasa.gsfc.gov

[2]ftp://ftp.swpc.noaa.gov/pub/warehouse/2014

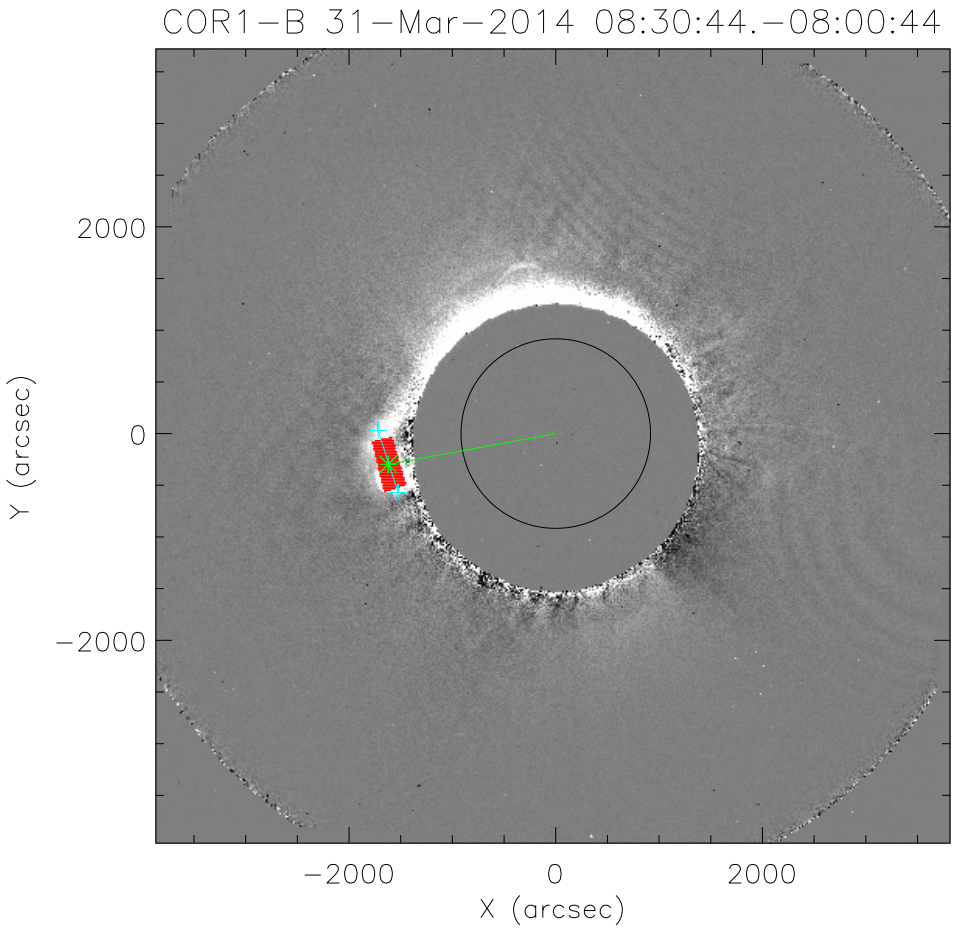

Figure 5.12: STEREO–B/-COR1 pB difference image obtained on 31 March 2014 at 08:30 UT. The subtracted reference image was observed at 08:00 UT prior to the CME onset. The 'gray' circle (radius 1.4 $R_{\odot}$) represents the occulting disk of the coronagraph. The enhanced emission to the left of the occulter corresponds to the same CME seen in Figure 5.11. The region marked with the red rectangular box is used for measuring the electron density of the CME LE. Its centroid (marked by the asterisk) has a projected heliocentric distance of $r_{\rm cor1b} = 1.8\ R_{\odot}$. The line joining the two '+' symbols represents the width ($\approx 0.69\ R_{\odot}$) of the CME LE which was assumed to be equal to its line-of-sight column depth for the pB inversion.

13° for the SOHO/-LASCO–C2 and GRAPH observations given that the CME came from AR12014 and propagated in the radial direction. The above active region must have been responsible for the non-thermal electrons necessary for the generation of

the radio emission in Figure 5.8. This supposition is supported by the presence of a bright surge like emission above the limb in the 174 Å images of the Sun[3], and the occurrence of the type III burst before the type IVm burst (see Figure 5.8). Note that both the surge and the type III burst occurred at possible locations of magnetic reconnection, a source of non-thermal electrons (see *eg.* Klein and Mouradian, 2002; White, 2007). The SOHO/-LASCO–C2 observations show that the CME LE at 08:36 UT was at a projected heliocentric distance ($r_{\rm lasco}$) of 2.5 $R_\odot$ (see Figure 5.11). The above CME was also observed in the FOV of the STEREO–B/-COR1 coronagraph (see Figure 5.12). Its LE is at a projected heliocentric distance ($r_{\rm cor1b}$) of 2.1 $R_\odot$. STEREO–B was behind the Earth at $E165°$ during the time of observation[4]. So the location of the flare corresponded to 28° behind the east limb of the Sun for the STEREO–B view. Assuming that the projection effects vary as $1/\cos(\phi)$, where ϕ is the angle from the POS, we calculated the de-projected heliocentric distance of the centroid of the type IVm burst from the GRAPH observations ($\phi = 13°$), and the de-projected heliocentric distances of the CME LE from the SOHO/-LASCO–C2 ($\phi = 13°$) and STEREO–B/-COR1 images ($\phi = 28°$). The resultant height-time (h-t) plot is shown in Figure 5.13. There is reasonably good agreement between the different measurements. This indicates that the same feature (*i.e.* the CME LE) was observed in the SOHO/-LASCO–C2 and STEREO–B/-COR1 images, and the type IVm burst in the GRAPH observations spatially corresponded with the CME LE. The estimated speed based on the linear-fit to the combined h-t measurements is 420 kms^{-1}. This agrees well with the average speed (423 kms^{-1}) of the CME LE in the LASCO–C2 FOV.

5.5 Analysis and Results

5.5.1 Emission mechanism

We interpret the type IVm burst in the present case by the second harmonic plasma emission based on the following analysis of the observations:

1) To check whether the type IVm burst can be attributed to non-thermal plasma emission similar to other types of low frequency radio bursts from the Sun Melrose (1985), a straight forward test is to ascertain whether the electron density ($n_{\rm e}$) near the burst region is reasonably sufficient for either the fundamental ($f_{\rm p}$) or second harmonic plasma emission ($2f_{\rm p}$) to occur at the observing frequency (f). We verified

[3]proba2.oma.be/swap/data/bsd/2014/03/31/

[4]stereo-ssc.nascom.nasa.gov/cgi-bin/make_where.gif

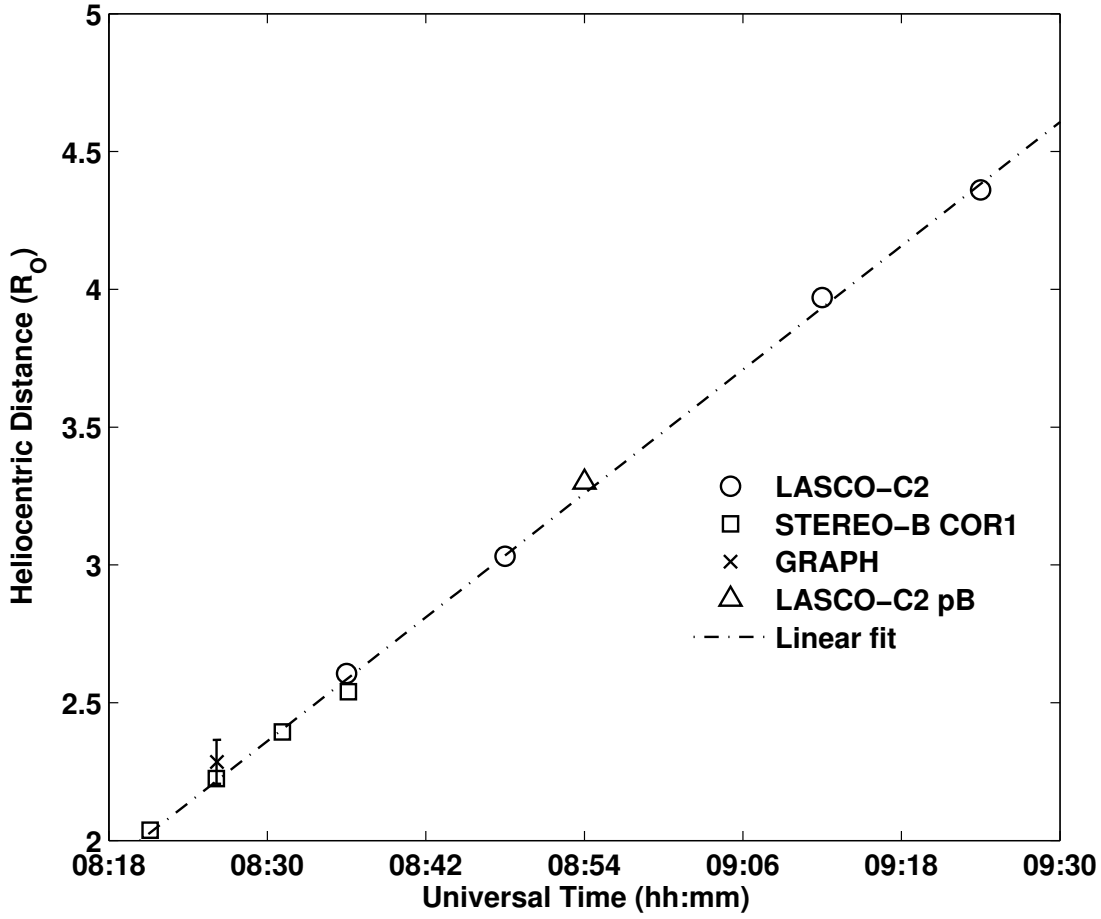

Figure 5.13: Height-time plot showing the de-projected heliocentric distances of the centroid of the type IVm burst observed with the GRAPH, and the position of the CME LE observed with the SOHO/-LASCO–C2 and STEREO–B/-COR1 coronagraphs on 31 March 2014 at different epochs.

this from the estimates of the coronal electron density obtained using the measurements of polarized brightness (pB) with the STEREO–B/-COR1 coronagraph (see Figure 5.12). The average electron density in the CME LE at 08:30 UT is $(6.7 \pm 3.2) \times 10^6$ cm^{-3}. This was derived from the background-subtracted pB radiation averaged over a selected region assuming that the line-of-sight (LOS) column depth of the CME LE is equal to its width and the CME propagates at an angle of 28° relative to the POS (see 5.4) for the pB inversion. The electron density of the background corona at the location near the CME LE ($r_{\rm cor1b} \approx 1.8\ R_\odot$, see Figure 5.12), estimated from observations at 08:00 UT, is $(5.9 \pm 1.4) \times 10^6$ cm^3 using the

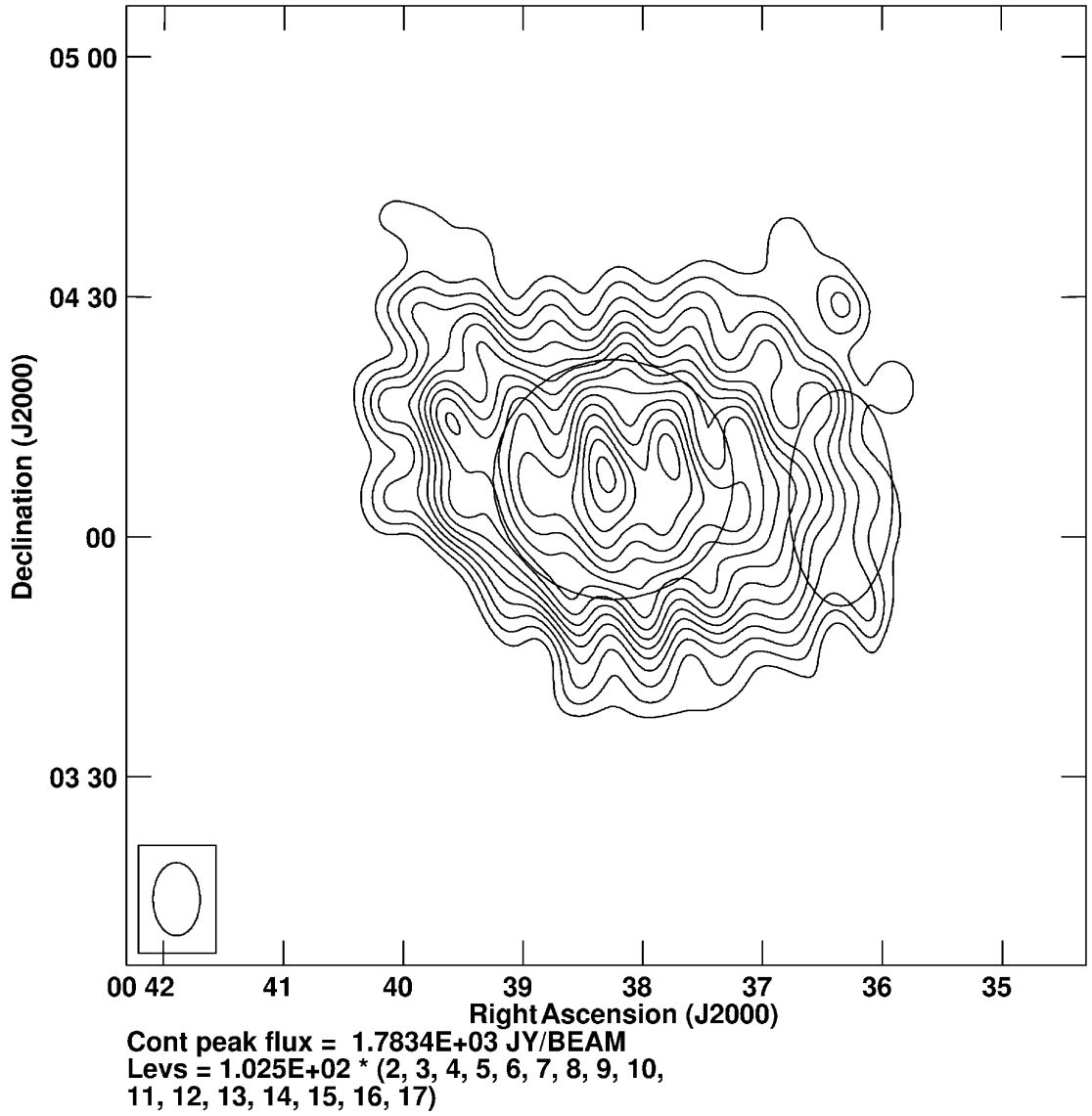

Figure 5.14: Radioheliogram of the 'undisturbed solar corona at 80 MHz obtained with the GRAPH close to 06:54 UT on 31 March 2014 prior to the type IVm burst observed that day (see Figure 5.11). The circle in the center of the image represents the solar limb. The angular resolution ('beam') of the GRAPH is shown inside the box in the lower left corner. The ellipse above the solar limb in the south-west quadrant indicates the approximate location and the size of the aforementioned type IVm burst source. Temperature T_b and the electron density estimates mentioned in Section 5.5.1 correspond to the coronal region within the above ellipse.

method of spherically symmetric inversion Wang and Davila (2014). We independently verified this using GRAPH observations of thermal free-free emission from the 'undisturbed' solar corona at 80 MHz close to 06:54 UT prior to the onset of the type

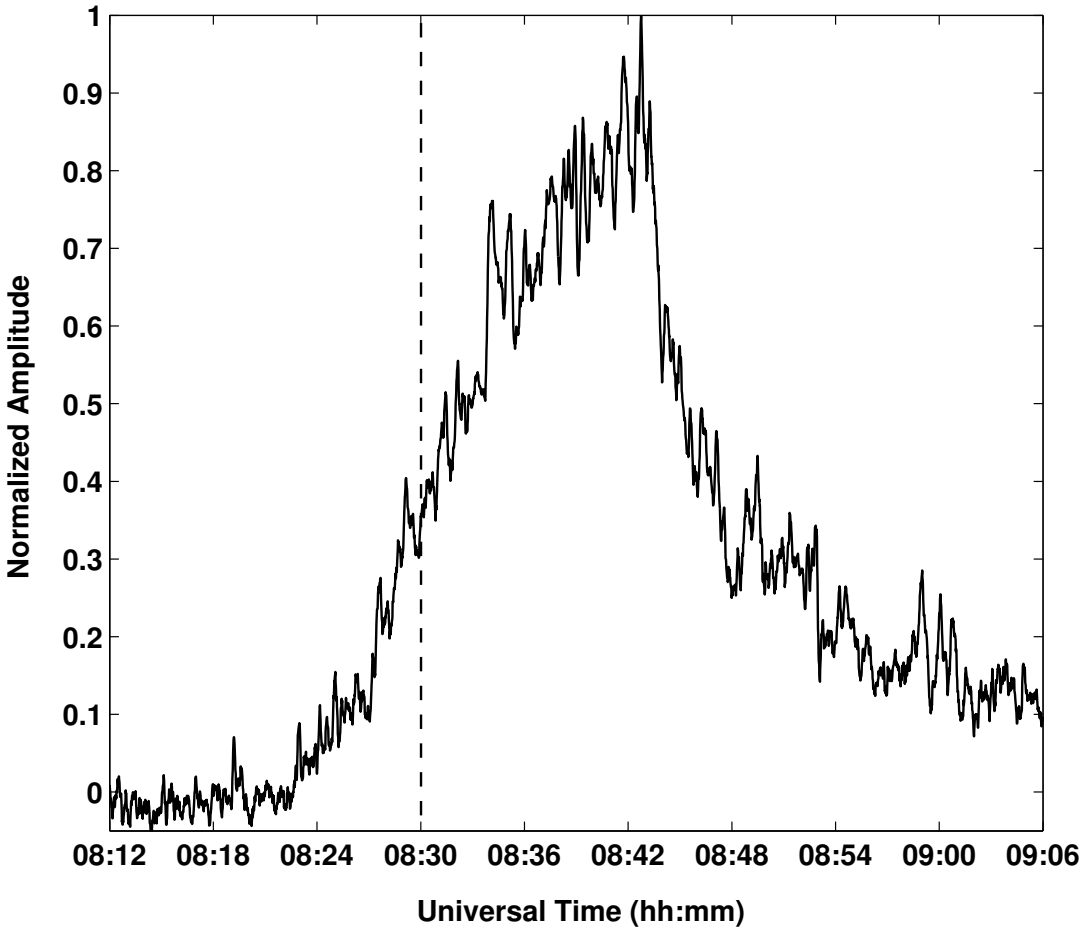

Figure 5.15: Time profile of the type IVm burst in Figure 5.8 at 55 MHz. The 'dashed' vertical line indicates the observations at 08:30 UT (see Section 5.5.1 for details).

IVm burst in Figure 5.11. The peak T_b at the location where the burst would be is $\times 10^5$ K (see Figure 5.14).

The corresponding electron density, calculated based on the assumption that the corona is optically thin close to the limb, is 4.6×10^6 cm^{-3} (see for eg. Ramesh, 2000). This agrees closely with the above STEREO–B/-COR1 estimate. Therefore the total electron density (CME LE + background corona at that location) around 08:30 UT is $(12.6 \pm 3.5) \times 10^6$ cm^3. Considering the 1σ error in the measurements, the upper limit to the estimated total electron density (i.e. CME + background) for the 31 March 2014 event at 08:30 UT is 16.1×10^6 cm^{-3}. Note that we have assumed that the LOS distance of the CME LE (i.e. the depth of the CME LE) is equal to its width of 0.69 $R_\odot$ (see Figure 5.12) for the above calculations. But it is possible

the 'true' depth could be lesser by a factor of up-to 5 (see for eg. Gary *et al.*, 1984), and hence the 'true' total density of the CME LE in the present case could be larger than 16.1×10^6 cm^{-3}. These imply that second harmonic plasma emission is the most likely cause of the type IVm burst observations in Figures 5.8, 5.10, and 5.11 at 80 MHz since it requires only a marginally higher electron density (19.8×10^6 cm^{-3}) at the location of the CME LE, which is estimated by assuming $f = 2f_p = 80$ MHz, where $f_p = 8979\sqrt{n_e}$ (in cgs units). Such electron densities in the CMEs are also common (Sheridan *et al.*, 1978; Stewart and McLean, 1982; Gopalswamy and Kundu, 1992; Akmal et al., 2001; Kathiravan *et al.*, 2002; Ramesh, Kathiravan and Sastry, 2003; Kathiravan and Ramesh, 2005; Bemporad *et al.*, 2007);

In addition, we find that the electron density in the CME LE estimated using independent pB difference image obtained with SOHO/-LASCO–C2 at 08:54 UT and 02:54 UT (the closest epoch at which pB observations were available with the above instrument) is also in support of the above claim. We obtained the average electron density of the CME LE to be $(3.1 \pm 0.8) \times 10^6$ cm^{-3}, and the corresponding background coronal density to be $(0.7 \pm 0.2) \times 10^6$ cm^{-3} (see Figure 5.16). So the total electron density around 08:54 UT is $(3.8 \pm 0.8) \times 10^6$ cm^{-3}. On the other hand, the GLOSS observations in Figure 5.8 show that the burst at 40 MHz was almost over at 08:54 UT. This indicates that the main emission of the burst has drifted to a frequency below 40 MHz at 08:54 UT, suggesting that the required electron density (4.9×10^6 cm^{-3}) for the second harmonic plasma emission at 40 MHz should be an upper limit of the CME LE at 08:54 UT. Our estimated density value from the LASCO–C2 pB data is consistent with this.

2) The low values of DCP at 65 and 80 MHz agree well with that reported previously for the second harmonic plasma emission (Suzuki and Sheridan, 1978; Melrose, Dulk and Smerd, 1978; Dulk and Suzuki, 1980; Ramesh *et al.*, 2010; SasikumarRaja and Ramesh, 2013; GLOSS: Kishore *et al.*, 2015);

3) An estimate of the spectral index (α_o) of the type IVm burst using the observations in Figures 5.9 and 5.10 indicate that $\alpha_o \approx$ -3.2. This is close to the expected spectral index $\alpha_t \approx$ -4.0 for second harmonic plasma emission based on theoretical calculations Dulk (1985); Kaplan and Tystovitch (1968); Melrose (1975);

4) fine structures that are noticeable in the type IVm burst in Figures 5.8, 5.9, and 5.10 point to the plasma emission mechanism Aurass *et al.* (2005); Benz (1993).

The possibility of non-thermal gyro-synchrotron emission as the cause of the type IVm burst (see for *eg.* Bastain *et al.*, 2001; Tun and Vourlidas, 2013; SasikumarRaja *et al.*, 2014) that is currently discussed is less likely because: 1) when the type IVm

bursts occur in a medium, the gyro-synchrotron emission should be strongly suppressed at frequencies $< 2f_{\rm p}$, (Wild and Smerd, 1972; Dulk, 1973; Melrose, 1985). The value of f_p corresponding to the total electron density (16.1×10^6 cm^{-3}) at the location of the CME LE is $\approx$ 36 MHz. This implies that if gyro-synchrotron emissions were responsible for the type IVm burst of 31 March 2014, the latter must have been suppressed at frequencies $<$ 72 MHz. The factor of suppression at $2f_{\rm p}$ (*i.e.* 72 MHz) should be $\approx$ 20 Dulk (1973). But we do not see any such suppression at 08:30 UT even at 55 MHz (see Figures 5.8 and 5.15). The observations of radio emission at still lower frequencies beyond the above epoch indicates that the condition for gyro-synchrotron emission in a medium, *i.e.* suppression below $2f_{\rm p}$, might not be satisfied during the corresponding periods also; 2) in the case of gyro-synchrotron emission, the peak $T_{\rm b}$ of the type IVm burst at 80 MHz is expected to be $\lesssim 10^7$ K Gopalswamy and Kundu (1990). This is less than the observed $T_{\rm b}$ in spite of the restricted angular resolution of the GRAPH (see Figure 5.14). These arguments reinforce our above interpretation that the type IVm burst in the present case is due to the second harmonic plasma emission.

Note that in our earlier work Ramesh *et al.* (2013) we had reported three different type IVm bursts generated by the second harmonic plasma emission from the 'legs' of the associated CMEs. But in the present case, the radio burst took place during the initial phase of the CME event (see Figures 5.11 and 5.12). The legs' of the CME were not distinguishable from its LE. Further the total electron density at the location of the CME LE was high enough to allow generation of the second harmonic plasma emission from there. These results suggest that both the 'legs' and the LE of the CMEs might possess sufficient electron density for the second harmonic plasma emission to be produced at low radio frequencies. Observations of CMEs near the Sun in white-light and estimates of their electron density are therefore crucial.

5.5.2 Estimate of the Magnetic Field

We adopted equation 3.1 to estimate B based on the discussions in section 3.2.2.2 that the type IVm burst observed at f=80 MHz is due to the second harmonic plasma emission. The peak DCP of the burst at 80 MHz is 0.07 (section 5.4). We assumed $a(\theta) \approx 1$ since, (i) the heliographic coordinates (S15W77) of the sunspot region associated with the type IVm burst corresponds to a viewing angle $\theta = 77°$, and (ii) the half-power widths and heliocentric distances of type IVm bursts at 80 MHz correspond to an average cone angle of 30° Robinson (1978); Suzuki and Dulk (1985). The occurrence of the CME close to the POS, the close spatial association between

the type IVm burst and the CME LE where the magnetic field is likely to be nearly perpendicular to the LOS (see Figure 5.11), and the low values of DCP (see 5.4) are consistent with the above assumption. Substituting the values in Equation (1), we get $B \approx 1.0$ gauss (G). The lower limit to B obtained using the criteria $B^2/8\pi = 2n_e k_B T_e$ for the confinement of the CME plasma, where n_e is the total electron density (CME LE + background) and $T_e = 1.5 \times 10^6$ K is the coronal electron temperature Reginald *et al.* (2011), indicates that $B > 0.4$ G. In this regard we would like to point out that Kwon *et. al.* (2013) had earlier reported $B = 0.6 \pm 0.4$ G at $r \approx 2.0\ R_\odot$ based on white-light observations of fast magneto-sonic waves associated with a CME. More recent observations of herringbone type II radio bursts in close association with the LE of a CME Hariharan *et al.* (2014) and doublet type II bursts due to interacting CMEs Hariharan *et al.* (2015), both close to the Sun ($r \lesssim 2\ R_\odot$), also give similar results. It is interesting to see that the magnetic field strength associated with a CME, estimated independently by applying Equation (1) for the first time to the second harmonic plasma emission from a type IVm burst, agrees well with the similar B values reported earlier based on other types of observations.

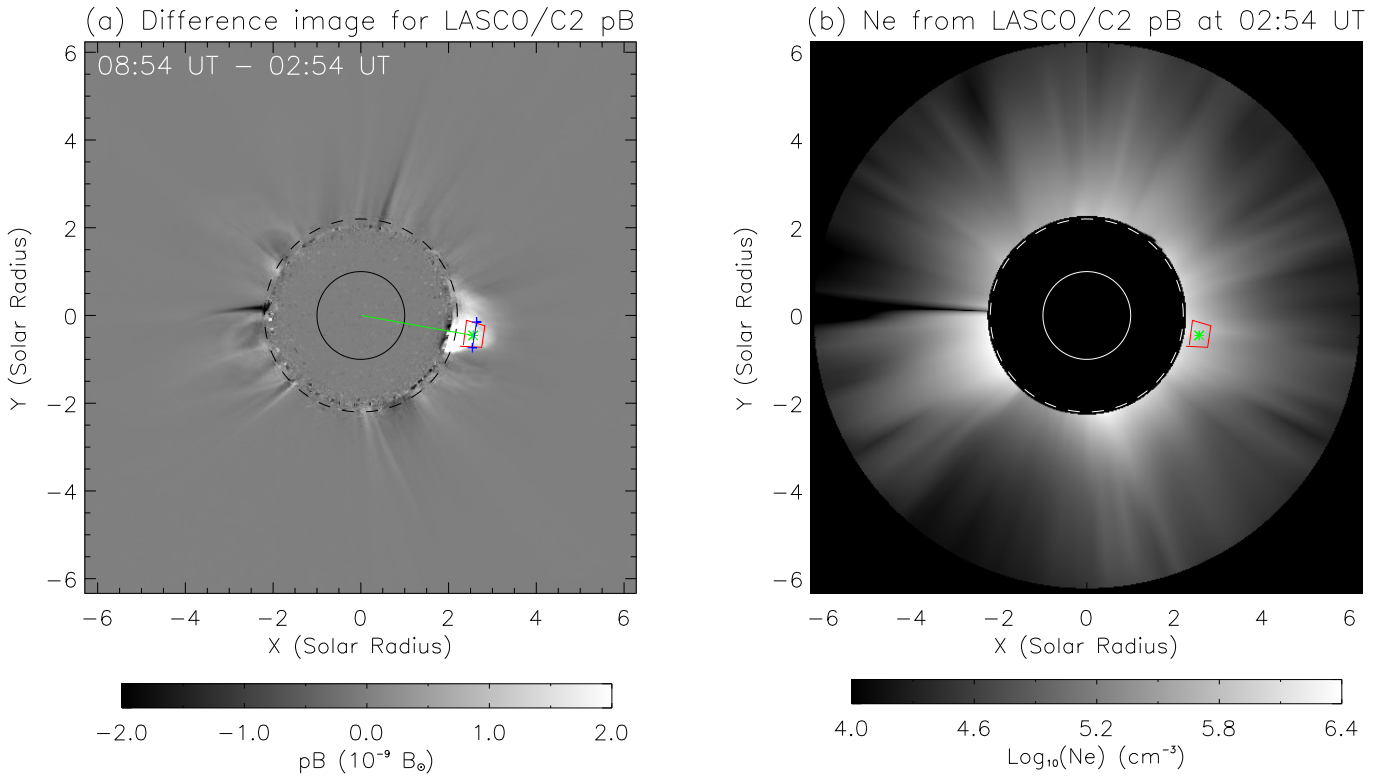

Figure 5.16: (a) SOHO/-LASCO–C2 pB difference image obtained on 31 March 2014 at 08:54 UT. The subtracted reference image was observed at 02:54 UT. The region marked with a box is used for measuring the electron density of the CME LE. Its centroid (marked by the asterisk) has a projected heliocentric distance of $r_{\rm lasco} = 2.6\ R_\odot$. The line joining the two '+ symbols represents the width ($\approx 0.57\ R_\odot$) of the CME LE which was assumed to be equal to its LOS column depth for the pB inversion. The solid circle indicates the solar limb and the bigger dashed circle (radius = $2.2\ R_\odot$) the occulter position. (b) The two-dimensional electron density derived from the pB image at 02:54 UT using the routine pb_inverter provided by the SolarSoftWare (SSW) based on the Van de Hulst technique (Van de Hulst 1950). The lines and the symbol have same meanings as in (a).

Chapter 6

Conclusions and Future Scope

We now conclude this thesis with the chapter-wise summaries of our results.

In Chapter 2 we described the details of design and fabrication of a log-periodic dipole antenna operating in the frequency range 85 − 15 MHz, which was particularly chosen in order to observe the solar corona from 1−2 $R_\odot$ in the solar atmosphere. This is very important as most of the dynamic events are thought to have their origin at this heliocentric distance range. The subsequent analog front-end components like the high pass filters, amplifiers were characterized through simple experimental set-up. A single antenna low-frequency spectrograph system was configured for regular solar radio observations using a conventional analog spectrum analyzer back-end. Preliminary RFI monitoring for 24 hours in a day was performed to ascertain the local RFI conditions at the GRO.

In chapter 3, we have presented the observation and analysis of two different split-band type-II radio bursts both of which were found to be associated with CMEs.
i) We estimated the magnetic field strength in the solar corona ahead of and behind the MHD shock front associated with a CME (at r = 2 $R_\odot$) that occurred on 2013 May 2, from the noticeable circular polarization exhibited by the harmonic component of the associated split-band type II radio burst with herringbone structures. The corresponding peak values are B ≈ (0.71.4)±0.2 G and (1.42.8)±0.1 G, respectively. Our results were found to be consistent with the estimates of the field strength in the coronal region ahead of the CMEs using other techniques, reported elsewhere. Also, our results are from the polarization observations and hence are independent of any coronal electron density model. At r = 2 $R_\odot$ ahead of a CME, the results indicate that B ≈ 0.64 G. We also obtained the coronal magnetic field strength at $2R_\odot$ for AR 11731 using the potential-field source-surface extrapolation scheme in Solar Software (Schrijver and De Rosa, 2003) and the value is B ≈ 0.2 G.

We have also reported the low frequency (< 100 MHz) radio observations of a split-band Type-II doublet burst that occurred on 20 February 2014 during the interval 03:22−03:26 UT, the onset–peak phase of the associated SF-class Hα and the C3.3 X-ray flares from the active region AR 11982 located at the heliographic coordinates S14W38. Using the spectral data set, the shock speeds of the first and the second Type-II bursts were calculated to be $\approx$ 648 kms^{-1} and $\approx$ 610 kms^{-1}, respectively. They were accompanied by a CME observed in the STEREO/B-COR1 FOV around the same epoch. The coronal magnetic-field in the upstream region of the CME was estimated from the split-band characteristics of the bursts to be $B \approx 1.3 - 1.1$ G over the frequency range $\approx 52 - 44$ MHz ($r \approx 1.49 - 1.58$ R$_\odot$) for the first Type-II burst, and $B \approx 1.3 - 1.0$ G over the frequency range $\approx 52 - 40$ MHz ($r \approx 1.49 - 1.64$ R$_\odot$) for the second Type-II burst. From polarimeter observations of the harmonic components of the first and the second Type-II bursts (at 80 MHz), the dcp corresponding to the first and the second Type-II bursts was estimated to be $\approx 0.1 \pm 0.02$ and $\approx 0.06 \pm 0.01$, respectively. These values were used along with magnetic-field strengths of the first and second Type-II bursts at 40 MHz to estimate the corresponding viewing angles ($\approx 72^\circ$ and $\approx 82^\circ$) of the source region of the bursts. Our analysis indicates that the doublet Type-II bursts are due to the near-simultaneous interaction between two different regions on the same CME with a preceding CME and a pre-existing streamer. Imaging observations of several similar events using low frequency solar-dedicated radio telescopes such as Nancay radioheliograph Kerdraon and Delouis (1997), Gauribidanur radioheliograph (Ramesh *et al.*, 1998; 1999; Ramesh, Subramanian and Sastry, 1999; Ramesh, Sundara Rajan and Shastry, 2006) with high angular resolution (Willson *et al.*, 1998; Ramesh and Ebenezer, 2001; Ramesh *et al.*, 2012) along with simultaneous radio spectral and CME observations (the latter particularly at $r < 2$ R$_\odot$) might help to improve the statistics of the Type-II doublet bursts and their association with the CMEs better.

Magnetic field strength in the solar atmosphere is routinely measured only in the photospheric and chromospheric layers at present. The coronal magnetic field is estimated from such measurements using extrapolation techniques. Estimates of the coronal magnetic fields through observations at microwave and infrared wavelengths are available (Lee, 2007; Lin, Penn and Tomczyk, 2000), but these correspond to regions very close to the base of the corona. To our knowledge, there are no published reports, particularly on the magnetic field near the LE of a CME in the middle corona, i.e., 1.2 R$_\odot \lesssim$ r $\lesssim$ 3.0 R$_\odot$, other than those mentioned in the previous paragraph. Acceleration of energetic particles by CME driven shocks occur typically in the above

distance range (Gopalswamy *et al.*, 2012). Given the paucity of coronal magnetic field measurements at present, particularly in close temporal and spatial association with a CME, our results provide useful constraints on the magnetic field strength involved in shock acceleration theories.

In chapter 4 we have presented the implementation of a correlation based spectrograph system using a digital back-end receiver. The spectrograph was configured to operate over the frequency range $15 - 30$ MHz and has gien us the possibility to have continuous observations of the Sun for $\approx$ 15 h in a day complimenting the spectral observations of the Wind-WAVES spececraft. We have also presented the observation of 71 individual bursts during the trial-run of the spectrograph system. We performed wavelet analysis for a group of long duration (> 100 s) type III solar radio bursts which indicate that these are preceded by either partial 'halo' or 'halo' CMEs are quasi-periodic with periodicities in the range $p \approx 4$ - 75 sec at a typical frequency like 19.5 MHz. The coronal magnetic field strengths calculated using the above periodicities are in the range $B \approx 1.00 - 0.06$ G. The digital signal processing techniques, higher temporal resolution, and the cross-correlation mode of operation helps to detect the quasi-periodicities in the time profiles with good contrast[1].

In Chapter 5 the details of a new digital spectrograph configured to operate in the frequency range $40 - 80$ MHz, was presented. The back-end receiver used for the spectrograph is based on a high-speed ADC and FPGA hardware that can sample and digitze a bandwidth of upto 250 MHz. The ADC card was successfully tested through lab experiments and it's characteristics were determined and verified. The performance of the digital back-end receiver was compared with that of the analog back-end through simultaneous observations of a solar type III radio burst. With the new digital back-end we achieved higher spectral and temporal resolution which is 10 $\times$ that offered by the analog spectrum analyzer back-end. This is useful in studying the fine structure phenomena associated with solar radio transients and to mitigate RFI in the low-frequency environment.

We have also reported the observations and analysis of the type IVm burst associated with the white light CME of 31 March 2014. The results indicate that the radio burst is due to the second harmonic plasma emission from the CME LE. The estimated strength of the magnetic field in the latter is $B \approx 1$ G at $r \approx 2.2$ $R_{\odot}$. An identification of the emission mechanism of the radio burst and the subsequent estimate of the associated magnetic field would not have been possible without the simultaneous whitelight, and radio imaging, spectral andt polarimetric observations.

[1]http://www.astro.umd.edu/∼white/gb/Data/Images/2013/10/28/20131028_042500_BIRS.png

With the whitelight coronagraphs onboard SoHO and STEREO continuing to provide interesting CME observations, and large low frequency radio antenna arrays like the *Murchison Widefield Array* (MWA; Londsale *et al.*, 2009 Tingay *et al.*, 2013), the *Long Wavelength Array Station 1* (Taylor *et al.*, 2012, Ellingson *et al.*, 2013) and the *Low Frequency Array* (LOFAR: Van Harleem *et al.*, 2013) being operational now, synchronous observations are expected to be useful for a better understanding of the near-Sun characteristics of the CMEs (see *eg.* Bastian and Gary, 1997; White, Kassim, and Erickson, 2003; Bastain, 2004; Salah *et al.*, 2005).

In summary, we have presented the implentation of a low-frequency spectrograph instrument with high dynamic range wide-band digtial receivers for solar radio observations. We have reported the observations of radio signatures of coronal shocks and analyzed their associated properties viz. speed, polarization etc. Using the high dynamic range and spectro-temporal resolution offered by the digital back-end we have presented the observations of fine-structure phenomena in type-IIIg and type-IVm solar radio bursts and their association with CMEs in conjuction with observations at other wave-bands from space-borne instruments. Our observations, analysis procedures, and results were presented which have been published in referreed scientific journals.

6.1 Future Work

This thesis work clearly demonstrated the usefulness of a wide-band back-end with high spectro-temporal resolution particularly for solar radio observations at low-frequencies down to the local ionospheric cut-off ($\approx$ 15 MHz) at the Gauribidanur Radio Observatory. This work could be further extended by implementing a full-digital wide-band receiver based on high-speed ADC and FPGA hardware[2] (Jack Hickish *et al.*, 2016) for the GRAPH providing spectroscopic imaging capability to the array. This augmentation will be useful for tomographic mapping of the solar corona at multiple frequencies over a wide range of heliocentric distance corresponding to the frequency range $30 - 120$ MHz which can be a useful tool for space weather forecasting studies. The high resolution offered by the back-end receiver in terms of time and frequency can be useful to probe the emission characteristics of very narrow-band short duration features that seem to occur at low radio frequencies which are presently not understood mainly due to the non-availability of solar-dedicated facilities. Considering the unsual extended minimum period of the present solar cycle, there

[2]https://casper.berkeley.edu/

is a possibility that the ionospheric cut-off frequency for radio wave propagation might decrease in the coming years even down to $\approx$ 5 MHz because of the steady decline in the solar and the interplanetary magnetic fields (Janardhan *et al.* (2015) and the references therein). So this gives us a unique oppurtunity to try out the possibility of astronomical observations at still lower frequencies ($<$ 15 MHz) by extending the low-frequency coverage of the existing instruments at the GRO making use of the latest digital hardware. This will be very useful for complimentarity observations with the proposed instruments at other wave-bands on-board the ADITYA-L5 mission.

Bibliography

Akmal, A., Raymond, J. C., Vourlidas, A., Thompson, B., Ciaravella, A., Ko, Y.-K., Uzzo, M., Wu, R.: 2001, *Astrophys. J.*, **553**, 922

Alissandrakis, C. E., Kundu, M. R., & Shevgaonkar, K. R.: 1991, *Astron. Astrophys.*, **251**, 276.

Allen, C. W.: 1947, *Mon. Not. Roy. Astron. Soc.*, **107**, 426.

Asai, A., Shimojo, M., Isobe, H., Morimoto, T., Yokoyama, T., *et al.*: 2001, *Astrophys. J. Lett.*, **562**, L103.

Aschwanden, M. J.: 1987, *Solar Phys.*, **111**, 113.

Aschwanden, M. J., Benz, A. O., & Montello, M. L.: 1994, *Astrophys. J.*, **431**, 432.

Aschwanden, M. J.: 2002, *Space Sci. Rev.*, **101**, 1.

Aschwanden, M. J.: 2004, Physics of the Solar Corona, (Berlin: Springer-Verlag), 407

Aubier, M., Leblanc, Y., & Boischot, A.: 1971, *Astron. Astrophys.*, **12**, 435.

Aurass, H. J.: 1997, In: Trottet, G. (eds.), *Coronal Physics from Radio and Space Observations*, Lecture Notes in Physics, Springer, Berlin 135.

Aurass, H. J., Rausche, G., Mann, G. & Hofmann, A.: 2005, *Astron. Astrophys.*, **435**, 1137

Avignon, Y., Bonmartin J., Boutille A., Clavelier B. & Hulot E.: 1989, *Solar Phys.*, **120**, 193

Baan, W. A., Fridman, P. A., & Millenaar, R. P.: 2004, *Astrophys. J.*, **128**, 933.

Bahcall, J. N., Huebner, W. F., Lubow, S. H., Parker, P. D., & Ulrich, R. K.: 1982, *Rev. Mod. Phys.*, **54**, 767.

Bale, S. D., Reiner, M. J., Bougeret, J. -L., *et al.*: 2009, *Geophys. Res. Lett.*, **26**, 1573.

Balanis, C., A.: 2005, Antenna Theory: Analysis and Design (New Delhi: John Wiley & Sons).

Bastian, T. S., Gary, D. E.: 1997, *J. Geophys. Res.*, **102**, 14031

Bastian, T. S., Pick, M., Kerdraon, A., Maia, D., & Vourlidas, A.: 2001, *Astrophys. J. Lett.*, **558**, L65.

Bastian, T. S.: 2002, *Astronomische Nachrichten*, **323**, 271.

Bastian, T. S.: 2004, *Planetary & Space Sci.*,
textbf52, 1381.

Baumbach, S.: 1937, *Astron. Nachr.*, **263**, 120.

Bemporad, A., Raymond, J. C., Poletto, G., Romoli, M.: 2007, *Astrophys. J.*, **655**, 576

Benz, A. O.: 1993, *Plasma Astrophysics. Kinetic Processes in Solar and Stellar Coronae*, **77**,184

Benz, A. O.: 1994, *Space Sci. Rev.*, **68**, 135.

Benz, A. O.: 1995, in Coronal Magnetic Energy Releases, eds. A.O.Benz & A.Krüger, *Lecture Notes in Physics* (Berlin: Springer), **444**, 1.

Benz, A. O., Monstein, C., Meyer, H., Manoharan, P. K., Ramesh, R., Altyntsev, A., *et al.*: 2009, *Earth, Moon & Planets*, **104**, 277.

Biermann, L.: 1957, The Observatory, **77**, 109.

Boischot, A.: 1957, C. R. Acad. Sci., **44**, 1326

Boischot, A., & Pick, M.: 1962, J. Phys. Soc. Japan, **17**, 203

Boischot, A., Rosolen, C., Aubier, M. G., Daigne, G., Genova, F., et al.: 1980, Icarus, **43**, 399.

Bougeret, J., -L., Kaiser, M. L., Kellogg, P. J., Manning, R., Goetz, K., *et al.*: 1995, *Space Sci. Rev.*, **71**, 5.

Bogod, V. M., Grebinskij, A. S., Opeikina, L. V., & Gelfreikh, G. B.: 1998, In : Costas E. Alissandrakis & Brigitte Schmieder (eds.), ASP Conf. Series, **155**, 279.

Brueckner, G. E., Howard, R. A., Koomen, M. J., Korendyke, C. M., Michels, D. J., Moses, D. J., *et al.*: 1995, *Solar Phys.*, **162**, 357.

Burkepile, J. T., Hundhausen, A. J., Stanger, A. L., St. Cyr, O. C. & Seiden, J. A.: 2004, *J. Geophys. Res.*, **109**, 3103.

Carrel, R. L.: 1961, International Convention Record, **9**, 61.

Cairns, I. H., & Robinson, R. D.: 1987, *Solar Phys.*, **111**, 365

Cairns, I. H., Knock, S. A., Robinson, P. A., & Kuncic, Z.: 2003, *Space Sci. Rev.*, **107**, 27

Cane, H. V., Erickson, W. C., & Prestage, N. P.: 2002, *J. Geophys. Res.*, **107**, SSH 14-1.

Cane, H. V., & Erickson, W. C.: 2005, *Astrophys. J.*, **623**, 1180.

Carley, E. P., Reid, H. A. S., Vilmer, N., & Gallagher, P. T.: 2015, *Astron. Astrophys.*, **581**, A100.

Chapman, S., & Zirin, H.: 1957, Smithsonian Contributions to Astrophysics, **2**, 1.

Cho, K. -S., Lee, -J., Gary, D. E., Moon, Y. J., Park, Y. D.: 2007, *Astrophys. J.*, **665**, 799.

Cho, K. -S., Bong, S. -C., Kim, Y. -H., Moon, Y. -J., Dryer, M., Shanmugaraju, A., *et al.*: 2008, *Astron. Astrophys.*, **491**, 873.

Cho, K.,-S., Bong, S.-C., Moon, Y.-J., Shanmugaraju, A., Kwon r.-Y., Park, Y.D.: 2011, *Astron. Astrophys.*, **530**, A16.

Cho, K., -S., Gopalswamy, N., Kwon, R., -Y., Him, R., -S., Yashiro, S.: 2013, *Astrophys. J.*, **765**, 148.

Claβen, H.T., Aurass, H: 2002, *Astron. Astrophys.*, **322**, 696.

Cliver, E.W., Nitta, N.V., Thompson, B.J., Zhang, J.: 2004, *Solar Phys.*, **225**, 105.

Cliver, E. W., & Ling, A. G.: 2009, *Astrophys. J.*, **690**, 598.

Dere, K. P., Brueckner, G. E., Howard. R. A., Koomen, M. J., Korendyke, C. M., *et al.*: 1997, *Solar Phys.*, **175**, 601.

Domingo, V., Fleck, B., Poland, A. I.: 1995, *Solar Phys.*, **162**, 1.

Duhamel, R. H., & Isbell, D. E.: 1957, IRE Nat. Conv. Rec., **Part I**, 119.

Dulk, G. A.: 1973, *Solar Phys.*, **32**, 491

Dulk, G. A., Smerd, S. F., MacQueen, R. M., *et al.*: 1976, *Astron. Astrophys.*, **88**, 203.

Dulk, G. A., McLean, D. J.: 1978, *Solar Phys.*, **57**, 279.

Dulk, G. A. & Suzuki, S.: 1980, *Astron. Astrophys.*, **88**, 203.

Dulk, G. A.: 1985, *Ann. Rev. Astron. Astrophs.*, **23**, 169

Duncan, R. A.: 1981, *Solar Phys.*, **73**, 191

Eastwood, J. P., Wheatland, M. S., Hudson, H. S., Krucker, S., Bale, S. D., *et al.*: 2010 *Astrophys. J.*, **708**, L95.

Ebenezer, E., Ramesh, R., Subramanian, K. R., Sundara Rajan, M. S. & Sastry, Ch. V.: 2001, *Astron. Astrophys.*, **367**, 1112.

Ebenezer, E., Subramanian, K. R., Ramesh, R., Sundara Rajan, M. S. & Kathiravan, C.: 2007, *Bull. Astron. Soc. India*, **35**, 111.

Ellingson, S., Craig, J., Dowell, J., Taylor, G. B & Helmboldt J., F.: 2013, *IEEE Trans. Ant. Prop.*, **2540**, 61

Erickson, W. C.: 1997, Publ. Astron. Soc. Aust., **14**, 278.

Felli, M., Lang, K. R., & Willson, R. F.: 1981, *Astrophys. J.*, **247**, 325.

Feng, S. W., Chen, Y., Kong, X. L., Li, G., Song, H. Q., Feng, X. S. & Guo, Fan: 2013 *Astrophys. J.*, **767**, 29F.

Foukal, P. V.: 2004, Solar Astrophysics, (Wiley-VCH).

Fomichev, V. V. & Chertok, I. M.: 1968, *Soviet Astron.*, **12**, 21.

Gary, D. E., et al.: 1985, *Astron. Astrophys.*, **152**, 42

Gary, D. E., Dulk, G. A., House, L. L., Illing, R., Sawyer, C., Wagner, W. J., McLean, D. J. & Hildner, E.: 1984, *Astron. Astrophys.*, **134**, 222

Gary, D. E., Hurford, G. J., Nita, G. M., White, S. M., McTiernan, J. & Fleishman, G. D.: 2014, *Meeting of the American Astronomical Society.*

Gergely, T. E.: 1986, *Solar Phys.*, **104**, 175

Ginzburg, V. L. & Zhelenzniakov, V. V.: 1958, *Soviet Astron.*, **2**, 653

Goff, C. P., van Driel-Gesztelyi, L., Démoulin, P., Culhane, J. L., Matthews, S. A., *et al.*: 2007, *Solar Phys.*, **240**, 283.

Golub, L., Deluca, E., Austin, G., et al.: 2007, *Solar Phys.*, **243**, 63.

Gopalswamy, N. & Kundu, M. R.: 1990, *Solar Phys.*,**128**, 377.

Gopalswamy, N. & Kundu, M. R.: 1989a, *Solar Phys.*, **122**, 91

Gopalswamy, N. & Kundu, M. R.: 1989b, *Solar Phys.*, **122**, 145

Gopalswamy, N., Kaiser, M. L., Lepping, R. P., Kahler, S. W., Ogilive, K., *et al.*: 1998, *J. Geophys. Res.*, **103**, 307.

Gopalswamy, N., & Mäkelä, P.: 2010, *Astrophys. J.*, **721**, L62.

Gopalswamy, N., Thejappa, G., Sastry, Ch. V. & Tlaimcha, N.: 1986, *Bull. Astron. Inst. Czech.*, **37**, 115.

Gopalswamy, N. & Kundu, M. R.: 1992, In: Zank, G.P. & Gaisser, T.K. (eds.), *Particle Acceleration in Cosmic Plasmas*, AIP Conf. Proc., **264**, 257.

Gopalswamy, N., Aguilar-Rodriguez, E., Yashiro, S., Nunes, S., Kaiser, M., L.: 2005, *J. Geophys. Res.*, **110**, A12S07.

Gopalswamy, N. :2006, In: Gopalswamy, N., Mewaldt, R. & Torsti, J. (eds.), *Solar Eruptions and Energetic Particles*, Geophys. Monogr. Ser. 165, AGU, Washington DC, 207.

Gopalswamy, N., Thompson, B. J., Davila, J. M., Kaiser, M. L., Yashiro, S., Mäkelä, P., *et al.*: 2009, *Solar Phys.*, **259**, 227.

Gopalswamy, N., Nitta, N., Akiyama, S., Mäkelä, P. & Yashiro, S.: 2012, *Astrophys. J.*, **744**, 72.

Gopalswamy, N., Xie, H., Mäkelä, P., Yashiro, S., Akiyama, S., Uddin, W., *et al.*: 2013, *Adv. Space Res.*, 51

Grognard, R. J. M. & McLean, D. J.: 1973, *Solar Phys.*, **29**, 149.

Hariharan, K., Ramesh, R., Kishore, P., Kathiravan, C. & Gopalswamy, N.: 2014, *Astrophys. J.*, **795**, 14.

Hariharan, K., Ramesh, R. & Kathiravan, C.: 2015, *Solar Phys.*, **290**, 2479

Hansen, R. T., Garcia, C. J., Hansen, S. F., & Yasukawa, E.: 1974 *Pub. Astron. Soc. Pac.*, **86**, 500.

Hiei, E., Hundhausen, A. J., & Sime, D. G.: 1993, *Geophys. Res. Lett.*, **20**, 2785.

Hoang, S., Lacombe, C., MacDowall, R. J., & Thejappa, G.: 2007, *J. Geophys. Res.*, **112**, A09102.

Holman, G. D., & Pesses, M. E.: 1983, *Astrophys. J.*, **267**, 837.

Howard, R. A., Moses, J. D., Vourlidas, A., Newmark, J. S., Socker, D. G., Plunkett, S. P., *et al.*: 2008, *Space Sci. Rev.*, **136**, 67.

Illing, R. M. E. & Hundhausen, A. J.: 1985, *J. Geophys. Res.*, *90*, 275.

Isbell, D., E.: 1960, IRE Trans. Antennas Propag., **AP-8**, 260.

Iwai, K., Tsuchiya, F., Morioka, A., & Misawa, H.: 2012, *Solar Phys.*, **277**, 447.

Jack Hickish *et al.*,: 2016, *J. Astron. Instrum.*, **05**, 1641001.

Janardhan, P., Bisoi, S. K., Ananthakrishnan, S., Tokumaru, M., Fujiki, K., Jose, L., & Sridharan, R.: 2015, *J. Geophys. Res.* (Space Physics), **120**, doi:10.1002/2015JA021123.

Kai, K. 1969, Publ. Astron. Soc. Aust., **1(5)**, 189

Kaiser, G.: 1994, A Friendly Guide to Wavelets (Boston: Birkhäuser).

Kaiser, M. L.: 2005, *Adv. Space Res.*, **36**, 1483.

Kaiser, M. L., Kucera, T. A., Davila, J. M., St. Cyr, O. C., Guhathakurta, M., Christian, E.: 2008, *Space Sci. Rev.*, **136**, 5.

Kaplan, S. A., Tsytovitch, V. N.: 1968, *Soviet Astron.*, **11**, 956

Kathiravan, C., Ramesh, R., Subramanian, K. R.: 2002, *Astrophys. J. Lett.*, **567**, L93

Kathiravan, C., Ramesh, R.: 2005, *Astrophys. J. Lett.*, **627**, L77

Kathiravan, C., Ramesh, R., & Nataraj, H. S.: 2007, *Astrophys. J.*, **656**, L40.

Kathiravan, C., Ramesh, R., Barve, V. I., & Rajalingam, M.: 2011, *Astrophys. J.*, **730**, 91.

Kerdraon, A.: 1979, *Astron. Astrophys.*, **71**, 266.

Kerdraon, A., Pick, M., Trottet, G., Sawyer, C., Illing, R., Wagner, W., House, L.: 1983, *Astrophys. J. Lett.*, **265**, L19.

Kerdraon, A. & Delouis, J.M.: 1997, In: Trottet, G. (eds.), *Coronal Physics from Radio and Space Observations*, Lecture Notes in Physics, **483**, Springer, Berlin 192.

Kishore, P., Ramesh, R., Kathiravan, C. & Rajalingam, M.: 2015, *Solar Phys.*, **290**, 2409.

Kishore, P., Kathiravan, C., Ramesh, R., Barve, V. I. & Rajalingam, M., 2014, *Solar Phys.*, **289**, 3995.

Kliem, B., Karlický, M., & Benz, A. O., 2000, *Astron. Astrophys.*, **360**, 715.

Klein, K. -L., Mouradian, Z.: 2002, *Astron. Astrophys.*, **381**, 683.

Komesaroff, M.: 1958, *Austr. J. of Phys.*, **11**, 201.

Kopp, G., Lawrence, G. & Rottman, G.: 2005, *Solar Phys.*, **230**, 129.

Kraus, J. D.: 1950, Radio Astronomy (New York: McGraw-Hill).

Kraus J. D.: 1986, Radio Astronomy, Second Edition, (Ohio: Cygnus-Quasar), 8-13

Kraus, J. D., & Marhefka, R. J.: 2001, Antennas, Third Edition, (McGraw-Hill:New York).

Kundu, M. R., Schmahl, E. J., & Rao, A. P.: 1981, *Astron. Astrophys.*, **94**, 72.

Kundu, M. R., Schmahl, E. J., Gopalswamy, N. & White, S. M.: 1989, Adv. Space Res., **9(4)**, 41

Kwon, R. -Y., Kramar, M., Wang, T. J., Ofman, L., Davila, J. M., Chae, J., Zhang, J.: 2013, *Astrophys. J.*, **766**, 55

Lang, K. R. & Willson, R. F.: 1987, *Astrophys. J.*, **319**, 514

Lantos, P., Pick, M. & Kundu, M. R.: 1984, *Astrophys. J.*, **283**, L71.

Leblanc, Y., Dulk, G. A., Vourlidas, A., & Bougeret, J. -L.: 2001, *J. Geophys. Res.*, **106**, 25301.

Lecacheux, A., Konovalenko, A. A., & Rucker, H. O.: 2014, Planet. Sp. Sci., **52**, 1357.

Lee, J.: 2007, *Space Sci. Rev.*, **133**, 73

Lemen, J.R., Title, A.M., Akin, D.J., Boerner, P.F., Chou, C., Drake, J.F., *et al.*: 2012, *Solar Phys.*, **275**, 17.

Lengyel-Frey, D., Thejappa, G., MacDowall, R. J., Stone, R. G., & Phillips, J. L.: 1997, *J. Geophys. Res.*, **102**, 2611

Li, B., Cairns, I. H., & Robinson, P. A.: 2009, *J. Geophys. Res.*, **114**, A02104.

Lin, R. P., Dennis, B., Hurford, G., Smith, D. M., & Zehnder, A.: 2004, In: Fineschi, S. & Gummin, M. A. (eds.), *Telescopes and Instrumentation for Solar Astrophysics*, *Proc. SPIE.*, **5171**, 38.

Lin, H., Penn, M. J., & Tomczyk, S.: 2000, *Astrophys. J. Lett.*, **541**, L83

Lin, J., Mancuso, S., Vourlidas, A.: 2006, *Astrophys. J.*, **649**, 1110.

Liu, Y., Luhmann, J. G., Bale, S. D., Lin, R. P.: 2009, *Astrophys. J. Lett.*, **691**, L151.

Londsale, C. J., Cappallo, R. J., Morales, M. F., Briggs, F. H., Benkevitch, L., Bowman, J. D, *et al.*: 2009, *Proc. of IEEE*, **1497**, 97

Ma, S., Raymond, J. C., Golub, L., *et al.*: 2011, *Astrophys. J.*, **738**, 160

MacDowall, R. J., Lara, A., Manoharan, P. K., Nitta, N. V., Rosas, A. M. & Bougeret, J. -L.: 2003, *Geophys. Res. Lett.*, **30**, 8010

Maia, D. J. F., Gama, R., Mercier, C., Pick, M., Kerdraon, A., Karlický, M.: 2007, *Astrophys. J.*, **660**, 874

Mancuso, S., Raymond, J. C.: 2004, *Astron. Astrophys.*, **413**, 363.

Mancuso, S., Raymond, J. C., Kohl, J., Ko, Y. -K., Uzzo, M., Wu, R.: 2003, *Astron. Astrophys.*, **400**, 347.

Mann, G. J., Classen, T., Aurass, H.: 1995, *Astron. Astrophys.*, **295**, 775.

Marsh, K. A. & Hurford, G. J.: 1980, *Astrophys. J.*, **240**, L111.

McLean, D. J., & Labrum, N. R.: 1985, Solar Radiophysics (Cambridge: Cambridge Univ. Press).

Melnik, V. N., Brazhenko, A. I., Konovalenko, A. A., Rucker, H. O., Frantsuzenk, A. V., *et al.*: 2014, *Solar Phys.*, **289**, 263.

Melrose, D. B., & Sy, W. N.: 1972, *Austr. J. of Phys.*, **25**, 387

Melrose, D. B.: 1975, *Solar Phys.***43**, 211

Melrose, D. B., Dulk, G. A., Smerd, S. F.: 1978, *Astron. Astrophys.*, **66**, 315.

Melrose, D. B.: 1980, *Solar Phys.*, **111**, 89.

Melrose, D. B., Dulk, G. A., Gary, D. E.: 1980, *Pub. Astron. Soc. Aust.*, **4**, 50.

Melrose, D. B.: 1985, In: McLean, D.J., Labrum, N.R. (eds.), *Solar Radio Physics*, Cambridge University Press, Cambridge, 211.

Mercier, C.: 1990, *Solar Phys.*, **130**, 119.

Mercier, C., & Trottet, G.: 1997, *Astrophys. J.*, **474**, L65.

Mercier, C., Subramanian, P., Kerdraon, A., *et al.*: 2006, *Astron. Astrophys.*, **447**, 1189.

Mercier, C., Subramanian, P., Chambe, G. & Janardhan, P.: 2015, *Astron. Astrophys.*, **576**, A136

Monstein, C., Ramesh, R. & Kathiravan, C.: 2007, Bull. Astron. Soc. India, **35**, 473.

Morioka, A., Miyoshi, Y., Masuda, S, Tsuchiya, F., Misawa, H., *et al.*: 2007, *Astrophys. J.*, **657**, 567.

Morosan, D. E., Gallagher, P. T., Zucca, P., Fallows, R., Carley, E. P., *et al.*: 2014, *Astron. Astrophys.*, **568**, A67.

Nakajima, H., Nishio, M., Enome, S., Shibasaki K., Takano, T. *et al.*: 1994, *Proc. IEEE*, **82**, 705.

Nakajima, H., Nishio, M., Enome, S., Shibasaki, K., Takano T. *et. al.*: 1995, *Astron. Astrophys. Suppl.*, **16**, 437.

Nelson, G. J., Melrose, D. B.: 1985, In: McLean, D.J., Labrum, N.R. (eds.) *Solar Radiophysics*, Cambridge Univ. Press, Cambridge, 333.

Oberoi, D., Matthews, L. D., Cairns, I. H., Emrich, D., Lobzin, V., *et al.*: 2011, *Astrophys. J.*, **728**, L27.

Offringa, A. R. : 2012, University of Groningen, dissertation.

Parker, E. N.: 1958, *Astrophys. J.*, **128**, 664.

Parijskij, Y. N.: 1993, *IEEE Antennas Propag. Mag.*, **35**, 7.

Payne-Scott, Ruby; Yabsley, D. E.; Bolton, J. G.: 1947, *Nature*, **160**, 256.

Pesnell, W. D., Thompson, B. J., & Chamberlin, P. C.: 2012, *Solar Phys.*, **275**, 3.

Pick-Gutmann, M.: 1961, Ann. Astrophys., **24**, 183

Pick, M., Forbes, T. G., Mann, G., Cane, H. V., Chen, J., Ciaravella, A., Cremades, H., Howard, R. A., *et. al.*: 2006, *Space Sci. Rev.*, **123**, 341.

Pick, M.: 2008, Astron. Astrophys. Rev., **16**, 1.

Prasad, S., Ananthakrishnan, S., Janardhan, P., Kundu, M. R., White, S. M., & Garaimov, V. I.: 2003, *Solar Phys.*, **218**, 247.

Prestage, N. P.: 1995, J. Atmos. Terres. Phys., **57**, 1815.

Pulupa, M., & Bale, S. D.: 2008, *Astrophys. J.*, **676**, 1330

Ramesh, R., Subramanian, K. R., Sundara Rajan, M. S. & Sastry, Ch. V.: 1998, *Solar Phys.*, **181**, 439.

Ramesh, R., Subramanian, K. R., & Sastry, Ch. V.: 1999, *Astron. Astrophys. Suppl.*, **139** , 179.

Ramesh, R., Subramanian, K. R., & Sastry, Ch. V.: 1999, *Solar Phys.*, **185**, 77.

Ramesh, R., & Sastry, Ch. V.: 2000, *Astron. Astrophys.*, **358**, 749

Ramesh, R.: 2000a, *Solar Phys.*, **196**, 213

Ramesh, R., & Ebenezer, E.: 2001, *Astrophys. J. Lett.*, **558**, L141.

Ramesh, R., Kathiravan, C. & Sastry, Ch. V.: 2003, *Astrophys. J. Lett.*, **591**, L163

Ramesh, R., SatyaNarayanan, A., Kathiravan, C., Sastry, Ch. V. & UdayaShankar, N.: 2005, *Astron. Astrophys.*, **431**, 353.

Ramesh, R., Sundara Rajan, M.S. & Sastry, Ch. V.: 2006, *Exp. Astron.*, **21**, 31.

Ramesh, R., Nataraj, H. S., Kathiravan, C. & Sastry, Ch. V.: 2006a, *Astrophys. J.*, 648, 707.

Ramesh, R., Kathiravan, C., Sundara Rajan, M. S., Barve V. I. & Sastry, Ch. V.: 2008, *Solar Phys.*, **253**, 319.

Ramesh, R., Kathiravan, C., Sreeja S. Kartha, & Gopalswamy, N.: 2010, *Astrophys. J.*, **712**, 188.

Ramesh, R., Kathiravan, C., Barve, I. V., Beeharry, G. K., Rajasekara, G. N.: 2010, *Astrophys. J. Lett.*, **719**, L41

Ramesh, R.: 2011, In: Choudhuri, A.R., Banerjee, D. (eds.), *Proc. of the 1st Asia-Pacific Solar Physics Meeting* (Astron. Soc. India Conf. Ser.), **2**, 55

Ramesh, R., Kathiravan, C. & Satya Narayanan, A.: 2011, *Astrophys. J.*, **734**, 39.

Ramesh, R., Annalakshmi, M., Kathiravan, C., Gopalswamy, N., & Umapathy, S.: 2012, *Astrophys. J.*, **752**, 107.

Ramesh, R., Kathiravan, C., Barve, V. I., Rajalingam, M.: 2012, *Astrophys. J.*, **744**, 165.

Ramesh, R., Sasikumar Raja, K., Kathiravan, C. & SatyaNarayanan, A.: 2013, *Astrophys. J.*, **762**, 89.

Ramesh, R., Kishore, P., Sargam M. Mulay, Indrajit V. Barve, Kathiravan, C. & Wang, T. J.: 2013, *Astrophys. J.*, **778**, 30.

Ratcliffe, H., Kontar, E. P., & Reid, H. A. S.: 2014, *Astron. Astrophys.*, **572A**, 111.

Reginald, N. L., Davila, J. M., St. Cyr, O. C., Rabin, D. M., Guhathakurta, M., Hassler, D. M., Gashut, H.: 2011, *Solar Phys.*, **270**, 235

Reid, H. A. S., & Ratcliffe, H.: 2014, Res. Astron. Astrophys., **14**, 773.

Reid, H. A. S., & Kontar, E. P.: 2015, *Astron. Astrophys.*, **577A**, 124.

Reiner, M. J., Kaiser, M. L., Fainberg, J., & Stone, R. G.: 1998, *J. Geophys. Res.*, **103(A12)**, 29651

Reiner, M. J., Fainberg, J., Kaiser, M. L., & Bougeret, J. -L.: 2007, *Solar Phys.*, **241**, 351.

Riddle, A. C.: 1974, *Solar Phys.*, **35**, 153

Roberts, J. A.: 1959, *Austr. J. of Phys.*, **12**, 327

Roberts, B., Edwin, P. M., & Benz, A. O.: 1984, *Astrophys. J.*, **279**, 857.

Robinson, R. D.: 1974, Publ. Astron. Soc. Aust., **2(5)**, 258

Robinson, R. D.: 1978, *Solar Phys.*, **60**, 383

Robinson, R. D. & Sheridan, K. V.: 1982, *Pub. Astron. Soc. Aust.*, **4**, 392.

Robinson, R. D.: 1983, *Pub. Astron. Soc. Aust.*, **5**, 208

Robinson, R. D., Stewart, R. T., Cane, H. V.: 1984, *Solar Phys.*, **91**, 159.

Rumsey, V. H.,: 1957, IRE National Convention Record, **5**, 114.

Ryabov, V. B., Vavriv, D. M., Zarka, P., Ryabov, B. P., Kozhin, R., *et al.*: 2010, *Astron. Astrophys.*, **510**, A16.

Salah, J. E., Lonsdale, C. J., Oberoi, D., Cappallo, R. J., Kasper, J. C.: 2005, In: Fineschi, S. & Viereck, R.A. (eds.), *Solar Physics and Space Weather Instrumentation*, *Proc. SPIE.*, **5901**, 124

SasikumarRaja, K., Kathiravan, C., Ramesh, R., Rajalingam, M., & Indrajit V. Barve: 2013b, *Astrophys. J. Suppl.*, **207**, 2.

Sasikumar Raja, K. & Ramesh, R.: 2013, *Astrophys. J.*, **775**, 38.

Sasikumar Raja, K., Ramesh, R., Hariharan, K., Kathiravan, C. & Wang, T. J.: 2014, *Astrophys. J.*, **796**, 56.

Schrijver, C. J. & De Rosa, M. L.: 2003, *Solar Phys.*, **212**, 165

Shanmugaraju, A., Moon, Y., -J., Dryer, M. & Umapathy, S.: 2003, *Solar Phys.*, **215**, 161.

Shanmugaraju, A., Moon, Y., -J., Cho, K.-S, Kim, Y., -H, Dryer, M. & Umapathy, S.: 2006, *Solar Phys.*, **233**, 117.

ShanmughaSundaram, G. A. & Subramanian, K. R.: 2004, *Solar Phys.*, **222**, 311.

Sheridan, K. V., Jackson, B. V., McLean & Dulk, G. A.: 1978, *Proc. Astron. Soc. Aust.*, **3**, 249

Sheeley, N. R., Hakala, W. N. & Wang, Y. M.: 2000, *J. Geophys. Res.*, **105(A3)**, 5081.

Shevgaonkar, R. K. & Kundu, M. R.: 1985, *Astrophys. J.*, **292**, 733.

Smerd, S. F., & Dulk, G. A.: 1971, In: Howard R. (ed.), *Solar Magnetic Fields*(Dordrecht: Reidel), IAU Symposium, **43**, 616

Smerd, S. F., Sheridan, K. V. & Stewart, R. T.: 1975, *Astrophys. Lett.*, **16**, 23.

Stewart, R. T.: 1966, *Austr. J. of Phys.*, **19**, 209

Stewart, R. T., McCabe, M. K., Koomen, M. J., Hansen, R. T. & Dulk, G. A.: 1974a, *Solar Phys.*, **36**, 203.

Stewart, R. T., Howard, R. A., Hansen, F., Gergely, T. E. & Kundu, M. R.: 1974b, *Solar Phys.*, **36**, 219.

Stewart, R. T. & Magun, A.: 1980, *Pub. Astron. Soc. Aust.*, **4**, 53

Stewart, R. T. & McLean, D. J.: 1982, *Pub. Astron. Soc. Aust.*, **4**, 386

Stewart, R. T. textitet al.: 1982b, *Astron. Astrophys.*, **116**, 217.

Stewart, R. T.: 1985, In: McLean, D. J., Labrum, N. R. (eds.), *Solar Radio Physics*, Cambridge University Press, Cambridge, 361

Subramanian, K. R. & Sastry, Ch. V.: 1988, *Astron. Astrophys.*, **9**, 225

Subramanian, K.R. & Ebenezer, E.: 2006, *Astron. Astrophys.*, **451**, 683.

Suzuki, S. & Sheridan, K. V.: 1978, *Radio Phys. & Quant. Elec.*, **20**, 989

Suzuki, S., Stewart, R. T., Magun, A.: 1980, In: Kundu, M. R., Gergely, T. E. (eds.), *IAU Symp. 86*, Radio Physics of the Sun, Dordrecht: Reidel, 241

Suzuki, S. & Sheridan, K. V.: 1982, *Pub. Astron. Soc. Aust.*, **4**, 382.

Suzuki, S., Dulk, G. A.: 1985, In: McLean, D. J., Labrum, N. R. (eds.) *Solar Radiophysics*, Cambridge Univ. Press, Cambridge, 320.

Schwenn, R.: 2006, *Living Reviews*, *Solar Phys.*, **3(2)**, 1 72.

Tajima, T., Sakai, J., Nakajima, H., Kosugi, T., Brunel, F., & Kundu, M. R.: 1987, *Astrophys. J.*, **321**, 1031.

Taylor, G. B., Ellingson, S. W., Kassim, N. E., Craig, J., Dowell, J., *et al.*: 2012, *J. Astron. Instrum.*, **1**, 1250004.

Thejappa, G., & MacDowall, R. J.: 2003, *Astrophys. J. Lett.*, **544**, L163.

Thejappa, G., Zlobec, P. & MacDowall, R. J.: 2003, *Astrophys. J.*, **529**, 1234.

Thejappa, G., & MacDowall, R. J.: 2008, *Astrophys. J.*, **676**, 1338.

Tingay, S. J., Goeke, R., Bowman, J. D., Emrich, D., Ord, S. M., Mitchell, D. A., *et al.*: 2013, *Pub. Astron. Soc. Aust.*, **e007**, 30

Tomczak, M. & Sfaforz, Ś: 2014, Cent. Eur. Astrophys. Bull., **38(2)**, 111.

Torrence, C., & Compo G. P.: 1998, Bull. Amer. Meteor. Soc., **79**, 61.

Tsuneta, S., Takahashi, T., Acton, L. W., Bruner, M. E., Harvey, K. L., & Ogawara, Y.:1992, *Pub. Astron. Soc. Japan*, **44L**, 211.

Tun, S. D., Vourlidas, A.: 2013, *Astrophys. J.*, **766**, 130

Tun, S. B., Cutchin, S. & White S. M.: 2015, *Solar Phys.*, **290**, 2423.

Van de Hulst, H. C. 1950, *Bull. Astron. Inst. Netherlands*, **11**, 135.

Van Harleem, M. P., Wise, W. M., Gunst, A. W., Heald, G., McKean, J. P., Hessels J. W. T. *et al.*: 2013, *Astron. Astrophys.*, **556**, A2

Vasanth, V., Umapathy, S., Vršnak, B., Annalakshmi, M.: 2011, *Solar Phys.*, **273**, 143.

Vasanth, V., Umapathy, S., Vršnak, B., Žic, T., Prakash, O: 2014, *Solar Phys.*, **289**, 251.

Vourlidas, A., Buzasi, D., Howard, R. A. & Esfandiari, E.: 2002, In A. Wilson (eds.) *Solar Variability: From Core to Outer Frontiers*, ESA Special Publication, 506

Vourlidas, A., Wu, S. T., Wang, A. H., Subramanian, P. & Howards, R. A.: 2003, *Astrophys. J.*, **598**, 1392.

Vršnak, B., Aurass, H., Magdalenić, J. & Gopalswamy, N.: 2001, *Astron. Astrophys.*, **377**, 321.

Vršnak, B.: 2001, *J. Geophys. Res.*, **291**, 106.

Vršnak, B., Magdalenić, J., Aurass, H. & Mann, G.: 2002, *Astron. Astrophys.*, **396**, 673.

Wang, T. J. & Davila, J. M.: 2014, *Solar Phys.*, **289**, 3723

Wedemeyer, S.: 2016, *The Messenger*, **163**, 15

Weiss, A. A.: 1963, Aust. J. Phys., **16**, 526

White, S. M., Kassim, N. E., Erickson, W. C.: 2003, In: Keil, S.L., Avakyan, S.V. (eds.), *Innovative Telescopes and Instrumentation for Solar Astrophysics*, *Proc. SPIE.*, **4853**, 111

White, S. M.: 2007, *Asian J. Phys.*, **16**, 189

Wild, J., P., Smerd, S., F. & Weiss, A., A.: 1963, *Ann. Rev. Astron. Astrophs.*, **1**, 291

Wild, J. P., Smerd, S. F.: 1972, *Ann. Rev. Astron. Astrophs.*, **10**, 159

Willes, A.J., Melrose, D.B.: 1996, *Solar Phys.*, **171**, 393.

Willson, R.F., Redfield, S.L., Lang, K.R., Thompson, B.J., St. Cyr., O.C.: 1998, *Astrophys. J. Lett.*, **504**, L117.

Yashiro, S., Gopalswamy, N., Michalek, G., St. Cyr, O.C., Plunkett, S. P., Rich, N. B. & Howard, R. A.: 2004, *J. Geophys. Res.*, **109**, 7105.

Zakharenko V., Konovalenko A., Zarka P., Ulyanov, O., Sidorchuk M. *et. al.*: 2016, *J. Astron. Instrum.*, **5**, 1641010,

Zaqarashvili, T. V., Melnik, V. N., Brazhenko, A. I., Panchenko, M., Konovalenko, A. A., *et al.*: 2013, *Astron. Astrophys.*, **555**, A55.

Zhang, J., Kundu, M. R., White, S. M., Dere, K. P, & Newmark, A. S.: 2001, *Astrophys. J.*, **561**, 396.

Zhao, R. -y., Mangeney, A., & Pick, M.: 1991, *Astron. Astrophys.*, **241**, 183.

Zimovets, I., Vilmer, N., Chian, A., C., -L., Sharykin, I., & Struminsky, A.: 2012, *Astron. Astrophys.*, **547**, A6

Zlobec, P., Messerotti, M., Karlický, M., & Urbarz, H.: 1993, *Solar Phys.*, **144**, 373

Zlotnik, E. Ia.: 1981, *Astron. Astrophys.*, **101**, 250.

Zucca, P., Carley, E. P., McCauley, J., Gallagher, P. T., Monstien, C., McAteer, R. T. J.: 2012, *Solar Phys.*, **280**, 591.

Zucca, P., Carley, E. P., Bloomfield, D. S., Gallagher, P. T.: 2014, *Astron. Astrophys.*, **564**, A47